UNIVERSITÀ DEGLI STUDI DI PARMA

Dottorato di Ricerca in Tecnologie dell'Informazione

XXVII Ciclo

PHOTONIC CRYSTAL FIBERS DESIGN FOR 2 μm WAVELENGTH OPERATION

Coordinatore:

Chiar.mo Prof. Marco Locatelli

Tutor:

Chiar.mo Prof. Stefano Selleri

Dottorando: *Carlo Molardi*

Gennaio 2016

To my family . . .

The only true wisdom is in
knowing you know nothing.

– Socrates

Contents

List of Figures

List of Tables

Introduction

In their history, started in the middle of 1950s of the last century and arrived in present days through a long sequence of achievements and improvements, optical fibers have progressively assumed a fundamental role in the field of science and technology with a dramatic impact in modern life. An optical fiber is basically a cylindrical dielectric waveguide, made with a transparent material, usually glasses or polymers, which guides light in the range from visible to near infrared. Nowadays, optical fibers can be successfully used in different applications which can be divided in four main groups. Optical fibers primary application can be ascribed to the field of telecommunication where fibers are the most important vehicle for long distance data transfer, mainly because of their huge transmission capacity and their low attenuation. A second remarkable application is the use of fibers to transport light as an illumination source for imaging purpose. For third, it is worth noting the possibilities which optical fibers can offer in the sensors field, where the large amount of optical properties that can be controlled in a fiber, can be efficiently used for an ample range of physical measurements. The last main application involves a particular class of fibers doped with optical-active rare earth ions, making the optical fiber to operate as an amplifier or as a laser. The key factor which justifies this large amount of applications is related to the possibility of varying most of the fiber parameters, its material composition and its cross-section geometry. Fibers design flexibility can range from a standard fiber design, composed by a core surrounded by a cladding with a lower refractive index, to a more elaborated design involving different materials or complex cross-section, such as the case of *Photonic Crystal Fibers (PCFs)* also called *Microstructured Fibers* or

Holey Fibers. PCFs are a special kind of fibers where the light guidance is obtained exploiting the presence of a periodical lattice of small holes inside a solid substrate of transparent medium. The introduction of PCFs in the middle of 1990s largely expanded the usability of fiber technology opening new horizons in optics. Probably the application which has benefited the most by the introduction microstructured fibers is the fiber laser technology, especially regarding high power operation.

A Laser, name which stands for *Light Amplification by Stimulated Emission of Radiation*, is an optical structure made by two fundamental components, an optical cavity and a gain medium within the cavity. The cavity acts as an optical resonator where circulating photons are multiplied by stimulated emission induced in the active medium. While stimulated emission is in phase with the incident light and while the cavity length permits only a discrete number of resonant frequencies, laser output consists of coherent emission. In a fiber laser, the active medium is represented by a rare earth doped optical fiber. Dopants normally used are: erbium, neodymium, ytterbium, thulium, praseodymium and holmium, each of these can emit in different wavelengths covering the region of near infrared. Fiber lasers offers several advantages with respect to the conventional semiconductor based and gas based lasers. Such advantages depend mainly by usage of an optical fiber as guiding medium and as gain medium. In fact, a doped fiber can produce a strong gain with a consequent high power output, avoiding excessive heating because of the large surface-to-volume ratio and maintaining a high quality near gaussian output beam. This characteristic of high quality beam combined with the possibility to obtain high power emission, both in *continuous wave (CW)* operation and *pulsed operation* is of interest in the field of industrial applications like machining, cutting, scribing, drilling and texturing where high precision work is often required. In the research for increasing the laser output power, three factors are playing a key role: at first it is mandatory to enlarge the core area to deliver more power remaining in a safe heating region of operation; for second the beam quality is strictly related to the modal content of output beam, so a diffraction limited beam requires to be single mode; finally every non-linear effect appearing in the light propagation inside the fiber medium shall be avoided or limited. In this contest, the benefit given by microstructured fibers is clear. The large amount of de-

gree of freedom offered by microstructured fibers design makes possible to tailor the light propagation inside the structure and consequently obtain larger beam effective area with single mode operation, dramatically scaling the output power achievable.

In the last decades of research, fiber lasers with 10 kW of output power in CW and several mJ of pulse energy in pulsed operation have been demonstrated. Such amazing results have been reached in particular in the emission region around 1064 nm using ytterbium doped fiber amplifiers. The use of ytterbium gives an important advantage due to his quantum efficiency in the mechanism of laser absorption-emission, limiting thermal induction inside the fiber, improving the stability and in general the quality of emitted beam. So most of the research in high power fiber lasers technologies has been focused in the emission region around 1064 nm and the fibers design has been consequently optimized for such operation.

In recent time, the laser around 2 µm operation is gaining interest in the scientific community, thanks to its intrinsic property to be eye-safe and thanks to the several applications that can be developed in this region. Water absorption which is particularly strong at 1.94 µm is of interest both in soft-tissue medical applications and laser imaging detection and ranging (LIDAR). The window of high atmospheric transparency between 2.02 and 2.25 µm instead can be efficiently used in remote sensing, communications and industrial processing. Fiber technologies can be considered as a good solution to supply amplification in the 2 μm region, in particular using thulium as dopant. Thulium offers a wide spectrum emission between 1.8 µm to 2.1 µm and absorbs at 790 nm, a wavelength which can be supplied by a cheap commercially available pump photo-diode. Unfortunately, thulium properties are not as brilliant as the ones exhibited by ytterbium in terms of lasing efficiency. Consequently, a number of problems deriving by the thermal effects induced by thulium large quantum defect and the different properties of light propagation at 2 µm make the thulium doped fiber laser design quite challenging. In principle, scaling of existing fiber designs, successfully used for ytterbium doped fiber laser, can not be an efficient solution. It is clear that a proper fiber design optimized for 2 µm, which takes in consideration the physical properties of thulium dopant, is a better solution which can open new frontiers in fiber laser technology.

Starting from this background the primary goal of this PhD thesis is focused on the study and design of new microstructured thulium doped fibers optimized to work in the region of 2 µm emission. Fiber design has been developed on the basis of the experience collected by a deep analysis of the state of art of thulium doped fiber lasers. Different fiber designs has been considered, exploring solutions which range from flexible fibers family to rod-type fibers design. In particular, a new class of asymmetric PCFs has been proposed to improve mode area scaling and single mode operation. Solutions to counteract thermal effects induced by the usage of thulium has also been proposed. Results, shown in this thesis, have been collected with the help of a full vectorial modal solver based on *Finite Element Method (FEM)*. This software has been developed, tested, optimized and upgraded with new functionalities, also within the timespan of my PhD period, by the *Group of Applied Electromagnetics (GAEM)* in the *Information Engineering Department (DII)* of the University of Parma. Additionally, in the field of fiber design for high power fiber lasers, a future improvement can be researched through the exploitation of disordered media properties. A part of this PhD work has been dedicated to the investigation of disordered materials properties in the context of random lasing in mid-IR region. This area of research is promising, in particular regarding fiber design for random fiber lasers, and is drawing huge attention in scientific community, opening new opportunities in the world of optics, both experimentally and theoretically. The thesis is organized with the following outline:

Chapter I: an overview on optical fiber technology from simple designs to most advanced microstructured fiber designs is presented. Principle of guidance and properties of light inside dielectric cylindrical waveguide are explained, introducing the concept of modes and the definitions of absorption, dispersion and non linearities.

Chapter II: fiber lasers are explained in detail introducing the advantages of fiber with respect to conventional systems. Then, high power operation is described focusing on the essential requirements that an optical fiber, suitable for laser systems, shall achieve to be effective. An overview on the most popular fiber

designs for high power operation is presented. In the end of the chapter 2 µm operation region is disclosed stressing on the issues which make fiber design, for such operation, quite challenging.

Chapter III: *large mode area (LMA) polarization maintaining (PM)* flexible PCF designs with a core diameter of 80 µm are investigated considering different bending radii. A new PCF design optimized for 2 µm is discussed, showing the capability to obtain a better single mode behavior with respect to a 1 µm fiber design scaled to work in 2 µm region.

Chapter IV and V: the properties of modes discrimination induced by symmetry free PCF design are discussed. Two new rod-type LMA PCF are presented and investigated through numerical simulations. Thermal behavior induced by high power operation is taken in consideration, showing the possibility to optimize the design to different thermal loads while pushing the core diameter to reach the value of 120 µm. A comparison with *Large Pitch Fibers (LPFs)*, which are considered as the state of art in the field of high power fiber lasers, shows the superior mode discrimination achievable with asymmetric design.

Chapter VI: a disordered optical planar structure is studied in order to depict modal properties and random lasing effect in the Mid-IR region, around 10 µm. At the beginning, the structure is supposed to be composed by a passive material and the analysis has been focused to show the nature of light transport, varying the amount of scattering, through the control of filling factor and through the manipulation of disorder impact. After that, the structure is investigated in presence of gain, showing the evolution of photons travel statistic at lasing threshold. Statistical analysis is performed with the help of a custom software, based on Monte Carlo Method, added with the possibility to consider properties of active media.

Eventually conclusions are drawn. A possible area of future research in the field of fiber optics is also proposed, combining the properties of disordered media with fiber technology.

Part of the content presented in this thesis, in particular chapters III and VI, has been completed through the support and the international collaboration with the renowned *Singapore Institute of Manufacturing Technology*, for this reason I would like to thank:

- Dr. Yu Xia and all the collaborators of *Precision Measurements Group (PMG)* at Singapore Institute of Manufacturing Technology (SIMTech), for having hosted me in the last two years of my PhD, guiding, supporting and helping me to complete this work, giving me the opportunity to open my mind to new fields of research in optics.
- Singapore and the Agency for Science Technology and Research (A*STAR), which supported my work with the scholarship offered by *A*STAR Research Attachment Programme (ARAP)*.

Chapter 1

Optical fiber

Nowadays, optical fibers are a fundamental device in the modern world, mainly for their large usage in telecommunication field where fibers have become the most common channel for long range, high density data transmission. In principle, optical fiber can be defined as a dielectric waveguide, with cylindrical symmetry, suitable to transport electromagnetic field in the range of visible and near infrared wavelength, which for simplicity is referred as light. The history of light transport in dielectric media began in the middle of 19th century with the demonstration, first by Collodon and Babinet [1, 2], then by Tyndall [3], of light confinement in a water flow. The first practical applications of this principle were demonstrated in the beginning of 20th century, when Baird (1920) and Lamm (1930) used glass fibers for illumination and imaging purpose. Some years later the principle of light transmission was improved toward the concept of modern optical fiber with the usage of a bundle of fibers coated with lower refractive index cladding for internal medical examination, by Hopkins and Kapany [4]. It was the introduction of the idea of laser in 1958 as a efficient source of light, by Townes and Schawlow, to push the research for a suitable medium to transport light at long distances [5]. Few years later (1966) Kao and Hockham published a paper where it was theoretically demonstrated that light loss in existing silica glass fibers could have been decreased by cleaning impurities in fibers [6], and in 1970 a group of scientists at Corning reached the goal of producing a single mode

fiber with attenuation of 17 dB/km. Starting from these pioneering works, with a continuous sequence of improvements of fiber technology and manufacturing process, today low impurity single mode silica fibers achieve a remarkable low attenuation of 0.2 dB/km in the telecommunication band around 1550 nm, making optical fiber a cheaper and more efficient data transmission medium with respect to copper cable. Further important achievements in fiber technology not only fostered the development of optical communication but also opened new paths in optics, making optical fibers an interesting platform for different applications such as lasers and sensing. In particular, a couple of fundamental research milestones contributed to the success of optical fibers. The first was the introduction of rare earth doped fiber amplifiers. These fibers, proposed in 1964 by Snitzer [7] to build the first prototype of fiber laser and then perfected in the 1985 by Poole et al. [8], not only offer the possibility to create long distance communication networks regenerating the signal without the use of inefficient optical-electrical-optical repeaters, but also represent a remarkable platform for modern fiber lasers. The second milestone is represented by the introduction of Photonic Crystal Fibers (PCFs) by the research group of Russell [9]. PCFs also referred as *Microstructured Fibers* or *Holey Fiber* cover an ample class of fibers where the cladding is built with a periodic lattice of holes along the propagation direction. The core can be solid or empty in the case of Hollow Core Fibers [10]. The large degree of freedom given by these structures and the possibility to finely tune the light propagation properties, make PCFs a fundamental tool in fields like fiber lasers, non-linear optics and sensing.

1.1 Step-index fiber

Step-index fiber (SIF) is the most simple kind of optical fiber which can be designed. Because of its simplicity, SIF is the most common fiber design successfully used in telecommunication and in other applications like fiber lasers, imaging and sensing. SIF basically consists in a cylindrical core surrounded by a cladding, a polymeric coating jacket can be included to protect the fiber, Fig. 1.1 (a). The most common material used to built optical fiber is silica (SiO_2), which is transparent in the near in-

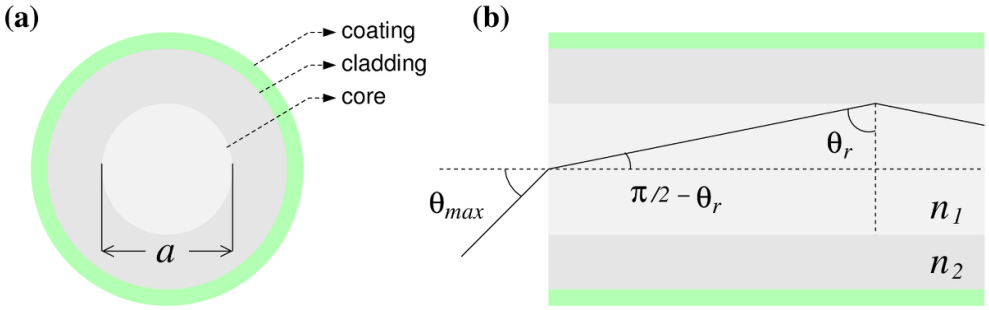

Figure 1.1: (a) cross-section of a step-index fiber, where the core, the cladding, and the coating jacket are clearly shown; (b) section of the same fiber with the explanation of TIR mechanism.

frared region, roughly between 0.6 µm and 2.1 µm. The basic principle of light guidance in such structure is the *total internal reflection (TIR)*, as shown in Fig. 1.1 (b). The refractive index profile is such that there is a step between core index n_1 and cladding index n_2, i.e. refractive index of the core is larger than cladding one. According to Sell's law of refraction, the incident electromagnetic field is totally reflected by the materials interface. For incident angles larger than a critical angle θ_r the light is trapped by the interface inside the core and can propagate through the fiber without significant losses. Index contrast between core and cladding is consequently important to define the quality of guidance inside the fiber and to define the angle of acceptance θ_{max} of the signal that can be focused inside the fiber. To tailor the index contrast between core and cladding, silica glass can be doped with different materials. Usually titanium dioxide (TiO_2), germanium dioxide (GeO_2), phosphorus pentoxide (P_2O_5), and aluminum trioxide (Al_2O_3) are used to increase refractive index, while boron trioxide (B_2O_3) and fluorine (F) can decrease the index [11]. Typical substrate for optical fiber is silica, because of its excellent physical and mechanical properties, but other materials can be used. Plastic optical fibers (POF), build with acrylic (PMMA) or polystyrene, show remarkable light guidance properties in visible range and can be efficiently used for the wiring of local networks [12]. Fluoride

fibers, based on fluoroaluminate or fluorozirconate glasses, instead offer very low attenuation in the range of mid infrared over 2 µm [13].

1.1.1 Principles of propagation, modes in fiber

The most correct way to describe propagation in fiber is to mathematically treat the structure as a waveguide, using the mode theory. Solving Maxwell's equations in frequency domain it is possible to suppose that electric and magnetic solutions can be decomposed in two components, where the former describes the field behavior along the transverse plane and the later describes the behavior along the propagation direction:

$$\overline{e}(x,y,z) = \overline{E}(x,y)e^{-\gamma z}, \tag{1.1}$$

$$\overline{h}(x,y,z) = \overline{H}(x,y)e^{-\gamma z}, \tag{1.2}$$

where $\gamma = \alpha + j\beta$, α is the attenuation constant and β is the propagation constant. $\overline{E}$ and $\overline{H}$ are mode functions, which describe the transverse configuration of electromagnetic propagating inside the fiber. Supposing no attenuation and considering that the optical fiber posses cylindrical symmetry, it is possible to write the wave equation in cylindrical coordinates ρ, ϕ and z:

$$\frac{\partial^2\overline{\psi}}{\partial\rho^2} + \frac{1}{\rho}\frac{\partial\overline{\psi}}{\partial\rho} + \frac{\partial^2\overline{\psi}}{\partial\phi^2} + \frac{\partial^2\overline{\psi}}{\partial z^2} + n^2{k_0}^2\overline{\psi} = 0, \tag{1.3}$$

where $\overline{\psi} = \overline{\psi}(\rho,\phi,z)$ stands for $\overline{E}$ or $\overline{H}$. The solution has this form:

$$\overline{\psi}(\rho,\phi,z) = \overline{F}(\rho)e^{-jl\phi}e^{-j\beta z}. \tag{1.4}$$

Substituting Eq. (1.4) inside Eq. (1.3), the problem becomes:

$$\frac{\partial^2\overline{F}}{\partial\rho^2} + \frac{1}{\rho}\frac{\partial\overline{F}}{\partial\rho} + \left(n^2{k_0}^2 - \beta^2 + \frac{l^2}{\rho^2}\right)\overline{F} = 0, \tag{1.5}$$

where the refractive index n is equal to n_1 for $\rho \leq a$, and to n_2 for $\rho > a$. a is the core radius. Eq. (1.5) is the Bessel differential equation. Its general solution assumes the

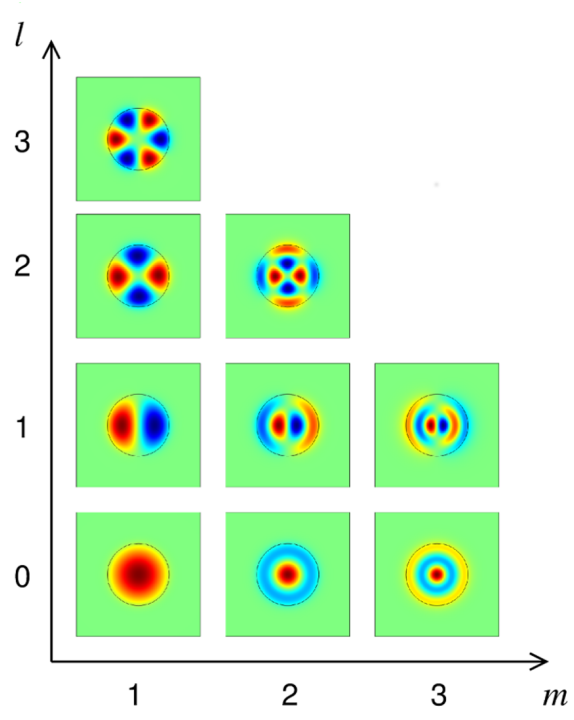

Figure 1.2: Examples of LP modes in a SIF.

following form:

$$F(\rho) = \begin{cases} J_l(p\rho), & \rho \leq a \\ K_l(q\rho), & \rho > a \end{cases} \tag{1.6}$$

where J_l is the the Bessel function of order l, while K_l is the modified Bessel function of order l, with $p = \sqrt{{n_1}^2 {k_0}^2 - \beta^2}$ and $q = \sqrt{\beta^2 - {n_2}^2 {k_0}^2}$. This solution is such that the field is guided inside the core and is exponentially decaying in the cladding. To determine all the field components and to calculate the value of β for each mode, it is necessary to impose the field continuity at the core-cladding interface and solve for an eigenvalue problem. The procedure is long and complex, the detailed explanation can be found in [14, 15].

The exact modes can be divided in four families, HE_{lm} and EH_{lm}, which have non-zero E_z and H_z components, and TE_{0m} and TM_{0m} without z components; the subscript indices l and m represent the order and the zeros of Bessel function. When the index contrast is low, which is typical in optical fibers, z component becomes negligible also for HE and EH and all the modes degenerate in *linearly polarized* (LP_{lm}) modes. Some examples of field distribution of LP modes in a SIF are shown in Fig. 1.2. The number of modes that can be excited in a fiber at a particular wavelength λ is strictly related to the core radius a and to the index contrast between core and cladding. It is possible to define the normalized frequency, also known as $V-$number as:

$$V = \frac{2\pi a}{\lambda}\sqrt{n_1^2 - n_2^2}, \tag{1.7}$$

where the square root term is the Numerical Aperture (NA). Similarly, the normalized propagation constant b is defined as:

$$b = \frac{n_{eff}^2 - n_2^2}{n_1^2 - n_2^2}, \tag{1.8}$$

where the effective index n_{eff}, equal to β/k_0, is the refractive index related to a mode with propagation constant β. From the plot of b vs $V-$number, plotted in Fig. 1.3, it is clear that for larger value of core radius and higher index contrast, the number of modes, which can be excited inside a fiber, increases. When V is less than 2.405, in the fiber can exist only the mode LP_{01} which is referred as Fundamental Mode (FM). So $V = 2.405$ is the discrimination value between single mode fiber (SMF) and multi mode fiber (MMF). In the field of telecommunication, a typical SMF has core diameter equal to 8.2 µm, cladding diameter equal to 125 µm, and NA equal to 0.14. After this short explanation on propagation in fiber, affected by several approximations, it is worth noting that in real case, propagation is influenced by three important factors: attenuation, dispersion and non-linearities.

1.1.2 Attenuation

Attenuation is caused by both absorption and scattering. Basically, absorption is an unavoidable property of the material, and it depends on several factors, in particular

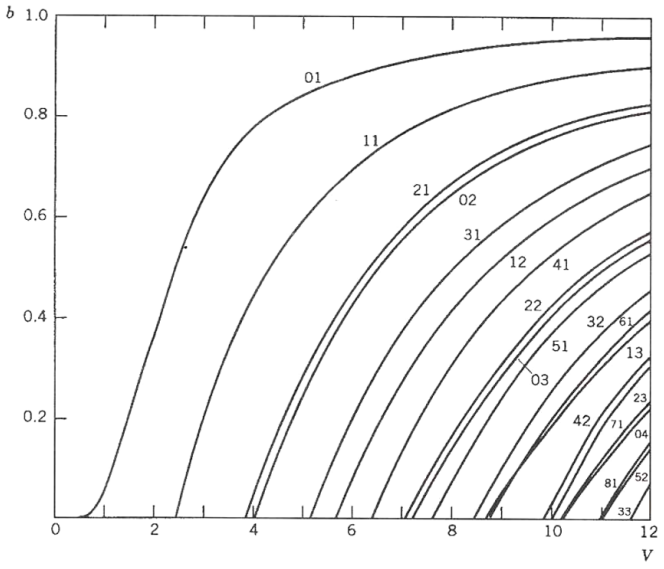

Figure 1.3: Normalized propagation constant b vs $V-$number. Every LP modes is characterized by a particular cut-off value.

presence of impurities, imperfections of the atomic structure, and the intrinsic absorption due to conductance of the material. On the other hand, scattering is caused by the interaction of the light with refractive index fluctuation inside the material, which is derived by density changes in the manufacturing process. Rayleigh scattering represents the main scattering factor. Figure 1.4 shows the attenuation profile of an silica based optical fiber. It is possible to notice that attenuation minimum is located at 1550 nm with a value of 0.2 dB/km, for this reason the windows around 1550 nm is widely used in the telecommunications systems. A second strong attenuation peak can be identified at 1400 nm, this is due to the absorption of the OH^- ions incorporated in the manufacturing process. Recently, fiber producers have improved their manufacturing process and OH^- absorption free fibers are commercially available [16]. Attenuation is then a factor that limits the signal propagation in an

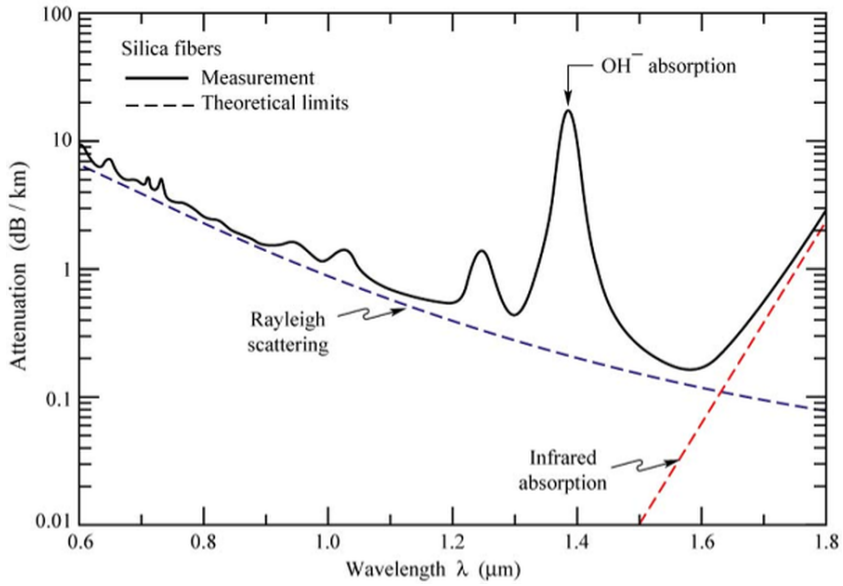

Figure 1.4: Attenuation profile of silica glass fiber. Theoretical profiles of Rayleigh scattering and infrared absorption are reported. This two phenomenons represent the attenuation theoretical limit.

optical fiber in long distance transmission, so in large area telecommunication networks optical amplifier are introduced to recover the signal. For different applications attenuation is not so critical as long as it remains less than 1 dB/m.

1.1.3 Dispersion

Dispersion is the second important factor involved in fiber propagation, in particular in pulse propagation. Dispersion does not cause power loss, but the broadening of optical pulses. There are two kind of dispersion. The first one is called modal dispersion and it appears in the presence of different modes propagating inside the structure. As different modes have different propagation constant β, they travel with different velocity inside the fiber. The resultant effects are the beating between modes and in general the spectral broadening of signal. Chromatic dispersion is the second kind of

dispersion inside the fiber. This phenomenon is independent of the number of modes and appears also in SMF. The reason of chromatic dispersion is the dependency of refractive index by the wavelength of incident light. In general, an input signal is not monochromatic, therefore its different wavelengths content experiences different propagation velocity. Mathematically dispersion can be defined as the Taylor expansion of propagation constant:

$$\beta(\omega) = n(\omega)\frac{\omega}{c} = \beta_0 + \beta_1(\omega - \omega_0) + \frac{1}{2}\beta_2(\omega - \omega_0)^2 + \cdots . \tag{1.9}$$

In the previous equation, the second and third terms are particularly important:

$$\beta_1 = \frac{1}{v_g} = \frac{1}{c}\left(n - \omega\frac{dn}{d\omega}\right), \tag{1.10}$$

$$\beta_2 = \frac{1}{c}\left(2\frac{dn}{d\omega} + \omega\frac{d^2n}{d\omega^2}\right), \tag{1.11}$$

because they are related to the group velocity v_g, i.e. the velocity of an envelope of frequencies, and to the group velocity dispersion (GVD), represented by β_2. Often, instead of using β_2, is common to describe chromatic dispersion with the parameter D defined as:

$$D = -\frac{\lambda}{c}\frac{d^2n}{d\lambda^2}. \tag{1.12}$$

When the value of D is positive, dispersion is referred as *anomalous dispersion*, otherwise as *normal dispersion*. Dispersion is considered detrimental in fiber optic communication because the pulse signal broadening is the main cause of inter-symbolic interference. However, dispersion combined with non-linearities can be effectively exploited in other applications, in particular supercontinuum generation. Optical fibers can be designed to compensate dispersion, using different index profiles and engineering the materials which compose the fiber. An important role in this field is played by microstructured fibers which offer an ample margin to tailor dispersion profile at different wavelength regions [17, 18].

1.1.4 Non-linearities

The response of a dielectric media, including optical fibers, becomes non-linear for intense electromagnetic fields. The understanding of non-linear effects is related to

the non-harmonic oscillation of bound electrons in the dielectric atoms, in response to incident light. Formally, the non linearities are identified as a non linear dependence of polarization vector P from electric field:

$$P = \varepsilon_0 \left(\chi^{(1)} E + \chi^{(2)} |E|^2 + \chi^{(3)} |E|^2 E + \cdots \right), \tag{1.13}$$

where $\chi^{(j)}$ is the susceptibility of order j. For silica glasses, the term $\chi^{(2)}$ vanishes, so non-linearities are due to the term $\chi^{(3)}$, whose main effect is to raise the refractive index:

$$\tilde{n}(\omega, E) = n(\omega) + n_{nl} |E|^2, \tag{1.14}$$

where n_{nl} is the non-linear index coefficient. Such behavior is known as Kerr effect. The intensity dependence of the refractive index leads to a large number of non-linear effects, the most common are the *self-phase modulation* (SPM) and the *cross-phase modulation* (XPM). SPM is described as the self-induced phase shift experienced by the electric field during its propagation inside the fibers. SPM is responsible for spectral broadening of ultrashort pulses. It is interesting to notice that in regime of anomalous dispersion, dispersion can compensate SPM leading the formation of optical solitons inside the fiber [19]. XPM refers to the nonlinear phase shift caused on an optical field by the action of another field having a different wavelength, direction, or state of polarization. XPM effect is two times more intense with respect to SPM considering the same incident field. Asymmetric spectral broadening of co-propagating optical pulses are caused by XPM. In principles, the effect of Kerr non-linearities in fibers can be summarized by highlighting the non-linear phase shift at a particular wavelength λ:

$$\phi_{nl} = \frac{2\pi}{\lambda} n_{nl} \frac{P}{A_{eff}} L, \tag{1.15}$$

where L is the length of the fiber, P is the power of the input beam, and A_{eff} is the mode effective area, which can be defined as:

$$A_{eff} = \frac{\left(\int_A |E|^2 \, dA \right)^2}{\int_A |E|^4 \, dA}. \tag{1.16}$$

As it is possible to notice from Eq. (1.15), non-linearities in fiber depend directly on the fiber length L, and inversely on the effective area.

While Kerr non-linearities are an elastic behavior of atomic oscillations, with the meaning that no energy given by the incident field is dissipated in the material structure, a second class of non-linearities presents an inelastic behavior. This non-linearities are due to the inelastic scattering between electromagnetic field and atomic structure of glass leading the excitation of vibrational modes of silica, also called phonons. The most important phenomena belonging to this class of non-linearities are the *Stimulated Brillouin Scattering* (SBS) and the *Stimulated Raman Scattering* (SRS). The main difference between SBS and SRS is that acoustical phonons participate in SBS while optical phonons participate in SRS. Both these effect can cause energy transfer between a wavelength to another one. In particular SRS can be exploited to amplify broadband input signals in those band region not covered by common rare earth amplifiers [20].

Usually, optical non-linearities in silica are quite weak compared to other media, however in the area of fiber optics it is possible to engineer fiber design to strongly enhance non linear effects. In this field, specialty photonic crystal fibers play a key role. Although in such application, like high quality beam fiber lasers, non-linear effects shall be avoided, they offer a great potential in a number of interesting applications. The main applications include solitons formation [21] , i.e. light pulses which preserve their shape for long distance, and supercontinuum generation for broadband laser sources [22]. Other applications of great interest are photonic switching, wavelength conversion, optical signal processing and dispersion compensation. Moreover, as previously mentioned, Raman scattering can be efficiently used to build optical amplifiers. Further information about the theory of non-linear fiber optics and their application can be retrieved in [23, 24, 25].

1.2 Photonic Crystal fibers

A PCF, also called microstructured fiber, is an optical waveguide that, instead of presenting well defined core and cladding like standard SIF, has a lattice of air holes, that goes through all the length of the fiber along propagation direction. PCFs, despite their unique properties, can not at present time substitute the role of standard fibers

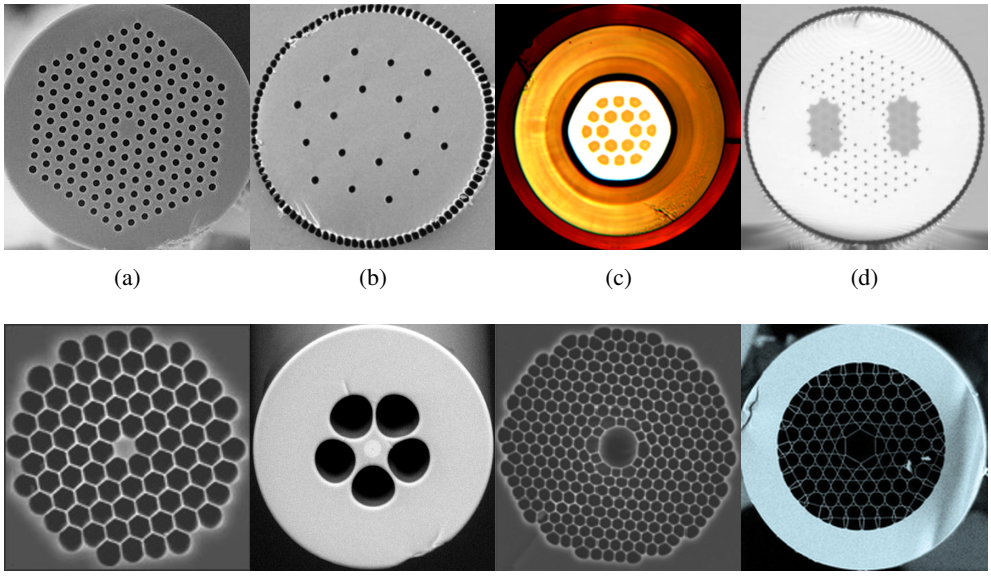

(a) (b) (c) (d)

(e) (f) (g) (h)

Figure 1.5: Cross-sections of different microstructured fibers: (a) standard LMA-PCF produced by NKT Photonics; (b) double cladding LPF; (c) leakage channel fiber LCF; (d) polarization maintaining DC-200-40-PZ-Yb produced by NKT Photonics; (e) high non-linear NL-1.5-670-02-SG produced By NKT Photonics for supercontinuum generation; (f) high non-linear Penta fiber; (g) Hollow core photonic bandgap fiber HC-1060-02 produced by NKT Photonics; (h) kagome lattice HC-PCF.

in telecommunications systems, because of their attenuation which is higher compared to standard fibers. PCFs can be divided in two family: solid core PCF where light propagates in a silica glass core, and hollow core PCF (HC-PCF), where light propagates inside an air core. In Fig. 1.5(a)-(h) some example of cross sections of PCFs are shown. The advent of this new kind of fibers has opened the way to a large number of different applications. The possibility to operate on the hole lattice varying parameters like disposition, distance and diameter of air holes made PCFs an efficient platform for applications impossible to treat with standard SIF. The main advantage

of PCF is the possibility to finely tune the index contrast between the core and the holey cladding, in particular in solid core PCF, operating on the hole diameter or on the distance between holes, according to the principle of mode sieve [26, 27]. The result is the ability to reach a lower index contrast than the one achievable operating only on glass doping. Such result makes easier to build PCFs with large mode area and robust single mode operation, suitable for high power fiber laser applications [28, 29]. Highly non-linear PCFs can be engineered with small core diameter, down to 1.5 μm. The small mode area increases significantly non linear effects making PCFs an optimum solution for the generation of supercontinuum light sources [22]. HC-PCF can be exploited to deliver signal in wavelength region over 2 μm where silica is no more transparent [30]. Another interesting applications are also possible with HC-PCFs, thanks to the possibility to infiltrate gases inside the core. In such configuration the interaction between light and gases gives the opportunity to exploit non-linearities stimulated in the molecule of the gas, with the results like amplification, high harmonic generation or frequency shift [31, 32]. Finally, PCFs offers a good platform for realization of fiber sensors.

1.2.1 Propagation principles in solid core PCF

In Fig. 1.6 a typical cross-section of solid core PCF is depicted. The holes are placed according to periodic triangular lattice, where d is the holes diameter, and the distance between the centers of two neighbor holes defines the pitch Λ. In solid core PCFs without active doping, the substrate is usually made of pure silica. The refractive index of the holey cladding is lower than core one because of the presence of holes. The electromagnetic waves can propagate in the core in a way that is similar to step index fibers. Such principle is usually called modified TIR. Due to the complex structure of PCF, an exact mathematical solution of Maxwell's equations is impractical, so a numerical approach shall be used to investigate modes distributions. The well-known Finite Element Method represents a good tool to calculate modal solutions. However, as for step-index fibers, it is possible to write the $V-$number for PCF

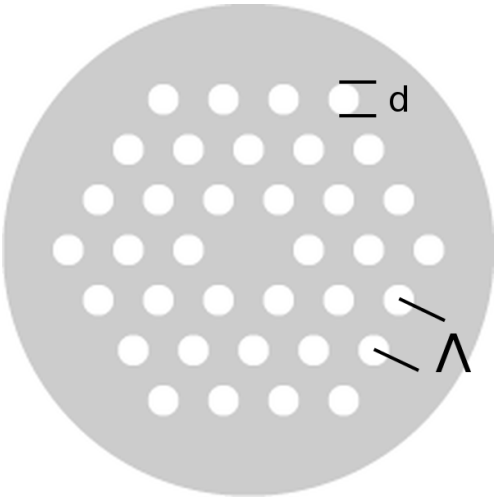

Figure 1.6: Cross-section of a solid core PCF with triangle lattice of holes. d is the hole diameter, while the pitch Λ is the distance between two neighbour holes.

[33], as follows:

$$V = \frac{2\pi\Lambda}{\lambda}\sqrt{n_{co}^2 - n_{cl}^2}, \tag{1.17}$$

where n_{co} and n_{cl} are the effective index of the core and the effective index of the cladding. The latter is defined considering an infinitely extended holes lattice in the cladding. As usual the single mode condition is obtained when $V = \pi$. Equation (1.17) has be solved with the help of a numerical strategy in order to obtain single mode operation. Nevertheless a simplified form, obtained as a result of data fitting [34], can be considered:

$$V\left(\frac{\lambda}{\Lambda}, \frac{d}{\Lambda}\right) = \frac{A\left(\frac{d}{\Lambda}\right)}{B\left(\frac{d}{\Lambda}\right)\exp\left[C\left(\frac{d}{\Lambda}\right)\frac{\lambda}{\Lambda}\right] + 1}, \tag{1.18}$$

where $A(d/\Lambda)$, $B(d/\Lambda)$, and $C(d/\Lambda)$ are reported in [34]. With the help of Eq. (1.18), it is possible to design the PCF parameters, where the ratio d/Λ is the most signifi-

cant, to achieve endless single mode regime. This value is obtainable from:

$$lim_{\lambda \to 0} V\left(\frac{\lambda}{\Lambda}, \frac{d}{\Lambda}\right) = \frac{A\left(\frac{d}{\Lambda}\right)}{B\left(\frac{d}{\Lambda}\right)+1} = \pi\,. \tag{1.19}$$

Clearly, the endless single mode conditions can be designed only by manipulating the geometry of fiber. From calculations, the optimum value of d/Λ is equal to 0.44 .

1.2.2 Propagation principles in Hollow core PCF

A HC-PCF is composed by a periodic lattice of capillaries, which create a two-dimension photonic crystal. This photonic crystal structure surrounds an hollow core. In a hollow core structure, the core refractive index is lower than the index of cladding region, as a consequence the field confinement can not be described by the mechanism of TIR. *Photonic Band Gap* (PBG) theory can be invoked to explain the light propagation in HC-PCFs. PBG is defined as the wavelength range where the structure can not absorb light or allow light propagation, this behavior can be achieved with a periodic dielectric structure. Photonic crystal periodicity defines the range of wavelengths which are not likely to propagate. In principle, tailoring the band gap can be possible by changing the periodicity of the structure. The difference of refractive index determines the size of the particular band gap for particular material. Light diffraction is well understood as the physical mechanism which originates the PBG. Because of the PBG imposed by the periodical structure, light is reflected back inside the core. Significant filling fractions of holes and small inter-hole silica bridges are necessary to permit propagation in the core which must be large enough.

1.2.3 Dispersion and attenuation

As the SIFs case, attenuation and dispersion affect light propagation in PCFs. The attenuation mechanisms for PCFs is driven by two main factors: the fraction of light propagating in glass and the roughness of glass-air interface. Solid core PCFs, where the light propagates in glass, show an attenuation profile which is similar to the one obtained in SIFs, an example is depicted in Fig. 1.7. The minimum loss value obtained so far is roughly 0.3 dB/km at the wavelength of 1550 nm [35], this value is

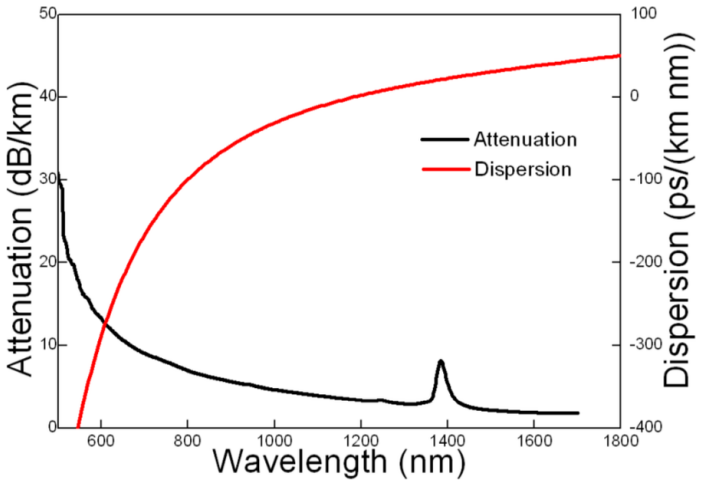

Figure 1.7: Attenuation and dispersion profile of the LMA10 PCF, produced by NKT Photonics.

higher than the minimum attenuation obtained for a SIF. This fact can be explained considering the roughness at the glass-air interfaces [36].

On the other hand, HC-PCFs show a good potential to overcome the 0.2 dB/km minimum attenuation of SIFs, mainly by the fact that light propagates in a air hole. Nowadays, the best attenuation achieved is 1.2 dB/km [37]. The limitation in HC-PCFs technologies derives from the surface roughness between core and periodic cladding. Such surface imperfections are introduced by the fabrication process. In some cases, the core mode can phase match a surface mode and the light can propagate onto the surface experiencing more scattering. To limit the loss imposed by the resonance between the core mode and surface modes, it is possible to act on the core dimensions. In general, for a particular wavelength the loss can be minimized by drawing a fiber with a proper core diameter. The optical overlap with surface modes scales inversely with the size of the fiber [37]. A second factor which causes loss in PCFs is given by confinement loss. In a real PCF, the photonic crystal lattice in the cladding is actually finite. For both solid core PCFs and HC-PCFs a certain period of air-holes is mandatory to decrease confinement losses [35].

PCFs suffer also from dispersion. In PCFs this factor can be tailored by changing the fiber design. In general, it is feasible to change the zero-dispersion point or the dispersion sign, with a remarkable degree of freedom. In solid core, PCFs larger air holes improve core isolation. Consequently, the zero-dispersion point can be shifted till the visible range. The large degree of freedom offered by PCFs makes it possible to draw a dispersion which is near insensitive to wavelengths, i.e. it is possible to tailor a flat dispersion over a certain wavelength range [18].

Chapter 2

High power fiber lasers

In the wide area of laser source, a particular important place is taken by fiber laser. These devices have gained a high reputation for representing a laser source with huge scalability potential in terms of power emission. This increase of performance, much higher respect to conventional bulk solid state or gas laser counterparts, has led fiber lasers to enter the context of applications formerly dominated by other lasers sources. While the possibility to generate high power emission is of course an attracting feature, fiber lasers offer others interesting advantages which are pushing them to substitute conventional sources. Such advantages can summarized in:

- High quality diffraction limited beam output, guaranteed by the possibility to obtain a robust mode operation.
- Efficient thermal dispersion, given by cylindrical symmetry of fibers which offer a high ratio between dissipative surface and volume.
- Broad gain line width, that can reach a value of 20 THz. This fact permits an ultra-short pulse operation and a wide range of tunability.
- High gains offered by the option of *master oscillator power amplifier (MOPA)* configuration. Typically most of the modern high power fiber laser systems are based on a low power seed, obtained with a master oscillator, followed by a high power fiber amplifier.

- Extremely high efficiency, considering both optical and electro-optical conversion.
- The possibility to build a complete fiber system offers a compact setup configuration, allowing fiber laser system to be integrated in a small case.

As explained in the previous chapter, the main application of optical fibers are related to communications. Nevertheless the first idea to use optical fibers in a laser system is quite old, and pioneering works are dated at the beginning of 1960s [38, 39]. With the introduction and the improvement of fiber amplifiers [8], the early choice for high power fiber lasers was to exploit the properties of neodymium as dopant with good results [40, 41]. With the advent of high brightness pump laser source between 900 nm and 980 nm neodymium has been substituted with ytterbium, whose potential has been recognized by Hanna [42]. Nowadays Yb-doped fiber lasers system has reached the impressive power of 10 kW in continuous wave (CW) and several mJ pulse energy in pulsed operation [29]. While ytterbium solution remains the most effective in terms of efficiency, recently a large interest is attracted by the 2 µm emission region, pushing research to improve fiber lasers doped with thulium, which has a wide emission region between 1800 nm and 2100 nm [43].

2.1 Fiber laser principles

2.1.1 Fiber amplifiers

Here a brief understanding, about physical mechanism of amplification in earth doped optical fibers, will be presented. However more complete information can be found in [44, 45]. To describe amplification in rare earth doped fiber, it is mandatory to begin from the basic properties of matter and the interaction between radiation and atoms. In a simplified explanation, matter can be described as an object that is characterized by a group of energy levels. Each level, which corresponds to an orbital in a single atom or a combination of many orbitals in a more complex structure, is populated by electrons. The amount of population of each energy level in the steady state depends on the temperature in a way to minimize the potential energy of the system. When

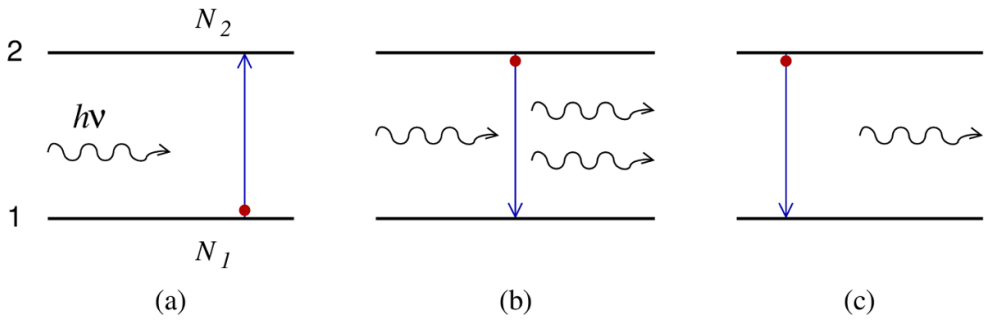

Figure 2.1: Physical mechanisms involved in laser emission: (a) absorption; (b) stimulated emission; (c) spontaneous emission.

matter is exposed to radiation, under the hypothesis that photons which compose the radiation are enough energetic, two events can happen: a photon can be absorbed promoting an electron to an higher level, this is called *absorption* Fig. 2.1(a); or an electron in a higher level can decay in phase with the incident radiation generating another photon, this phenomenon is called *stimulated emission* Fig. 2.1(b). A third event can happen, when a high level electron decays spontaneously generating a non coherent photon, this is referred as *spontaneous emission* Fig. 2.1(c). The dynamic of these physical mechanisms are described by *Einstein coefficients*:

$$\frac{dN_1}{dt} = -W_{12}N_1 = \sigma_{12}\frac{I}{h\nu}N_1\,, \tag{2.1}$$

$$\frac{dN_2}{dt} = -W_{21}N_2 = \sigma_{21}\frac{I}{h\nu}N_2\,, \tag{2.2}$$

$$\frac{dN_2}{dt} = -A_{21}N_2 = \frac{1}{\tau}N_2\,, \tag{2.3}$$

where N_1 and N_2 are the concentrations of electrons in two considered energy levels, while W_{12}, W_{21} and A_{21} are the Einstein coefficients whose meaning is the rate of transition between the energy levels. W_{12} and W_{21} are proportional to the intensity I of incident radiation, and consequently to the photons flow. The proportionality is given by σ_{12} and σ_{21} which are called *absorption cross-section* and *emission cross-section*. The coefficient A_{21} of spontaneous emission is the inverse of lifetime τ.

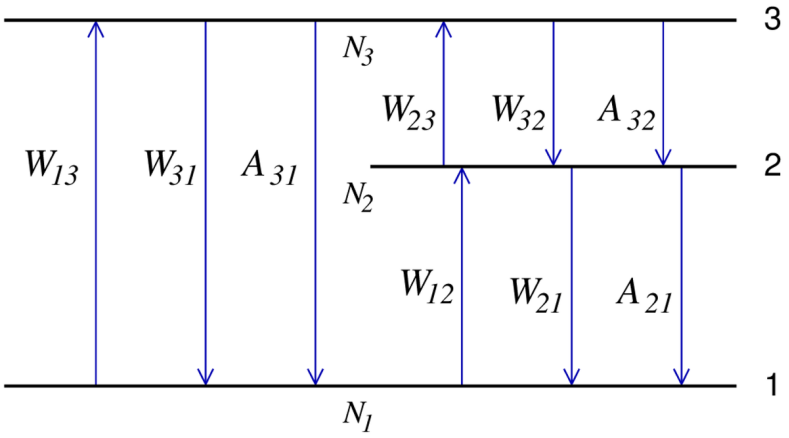

Figure 2.2: Schematic of a three level system. Many of the four level system can be reduced to this schematic. When level 3 and level 2 are very near with respect to each others, the system is referred as quasi-two level.

Eventually h is the Plack's constant and ν is the frequency of incident radiation. The previous equations give the rate of transition between states, for this reason are called *population equations*.

Now it is possible to consider a rare earth doped glass, where the energy levels are given by the active dopant. Depending on the dopant, the energy levels involved in the laser dynamic can be two, three or four. It is common to reduce all the cases to the case of three levels, shown in Fig. 2.2. The dynamic of fiber amplifier is easy to understand on a three level system: a *pump laser* excites the transition between level 1 and level 3, after that a non radiative decay occurs between level 3 and level 2, populating this level, finally a *seed input* with proper frequency is amplified by stimulated emission occurring between level 2 and level 1. According to this logic, the system can be further simplified assuming a fast transition between level 3 and level 2, consequently level 3 is not populated and $N_3 = 0$. In the steady state, it is

possible to write the *simplified population equation for a three levels system*:

$$N_1 = \frac{W_{21} + A_{21}}{W_{13} + W_{12} + W_{21} + A_{12}} N_t \,, \tag{2.4}$$

$$N_2 = \frac{W_{12} + W_{12}}{W_{13} + W_{12} + W_{21} + A_{12}} N_t \,, \tag{2.5}$$

$$N_t = N_1 + N_2 \,. \tag{2.6}$$

Considering the dynamic state with the signals, i.e. pump and seed, varying along the length of the amplifier, and assuming the core uniformed doped with rare earth, it is now possible to write *propagation equations* which show the evolution of the power inside the amplifier, as a function of the spatial coordinates. These equations are coupled with the population equation to fully define the amplifier:

$$\frac{dP_k(z)}{dz} = \pm\Gamma_k\sigma_{12}N_1(z)P_k(z) \pm \Gamma_k\sigma_{21}N_2(z)P_k(z) \pm \Gamma_k\sigma_{21}N_2(z)2h\nu_k\Delta\nu_k \,, \tag{2.7}$$

$$N_2(z) = \frac{\sum_k \tau\Gamma_k\sigma_{12}\frac{P_k(z)}{h\nu_k\pi a^2}}{1 + \sum_k \tau\Gamma_k(\sigma_{12}+\sigma_{21})\frac{P_k(z)}{h\nu_k\pi a^2}} N_t \,, \tag{2.8}$$

$$N_t = N_1(z) + N_2(z) \,, \tag{2.9}$$

where Γ_k are the overlap integrals of the field with the doped core:

$$\Gamma_k = \int_0^a \int_0^{2\pi} i(r,\phi,z)\, d\phi\, dr \,. \tag{2.10}$$

It is worth noting that the last term in Eq. (2.7) represents the contribution of *amplified spontaneous emission - (ASE)*. Furthermore, the subscript k and the symbol $\pm$ take in consideration all the signals involved in the amplification, considering also the counter-propagating contributions. Finally, it is important to stress that cross-sections are frequency dependent, so different wavelengths contribute differently in the absorption-emission mechanism, as an example in Fig. 2.3 are shown emission and absorption cross-sections of ytterbium doped glass. As long as population inversion is maintained, the emission at the target wavelength is stronger than absorptions, consequently the input signal is amplified.

It is possible to exploit the properties of different rare earth dopant to obtain amplification in different regions of visible or near infrared. Ytterbium, pumped at

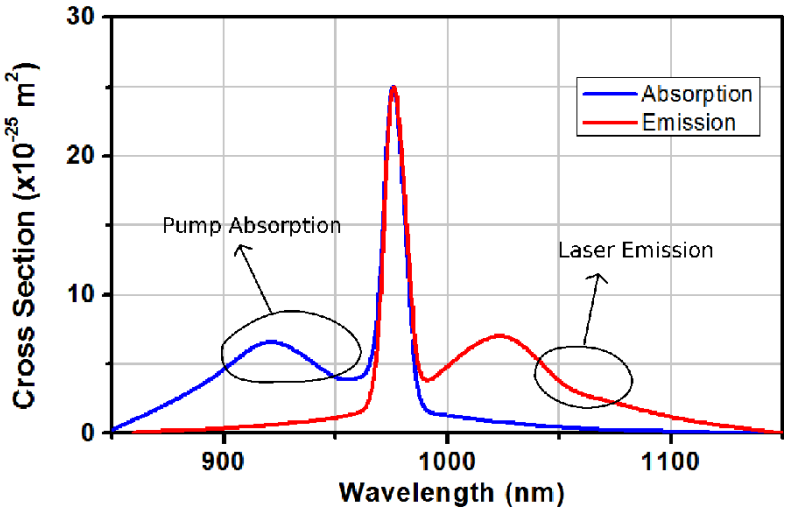

Figure 2.3: Emission and absorption cross-section of ytterbium doped silica glass.

975 nm and emitting at 1064 nm, is usually the most common solution for high power fiber laser, principally for its low quantum defect which permits an excellent optical efficiency with low distortion due to the thermal load [46]. In Tab. 2.1 the region of emission of the most common rare earth dopants are shown.

2.1.2 Continuous wave operation

In order to build a laser, two components are mandatory: an active medium which supplies gain and a cavity to create one or more resonant modes amplified by the active medium. A fiber laser is not an exception. In the previous section, it has been demonstrated the effectiveness of rare earth doped fiber amplifiers, in particular the ones doped with ytterbium, so the active medium offered by fiber amplifier represents an excellent and efficient solution for lasing. The issue is now to create a cavity. Fortunately, it is not really difficult, simply cutting and cleaving the fiber ends it

Ion	Host media	Emission wavelength
Nd^{3+}	YAG, YVO_4, YLF, silica	1.03↔1.1 µm, 0.9↔0.95 µm, 1.32↔1.35 µm
Yb^{3+}	YAG, tungstates, silica	1.00↔1.1 µm
Er^{3+}	YAG, silica	1.5↔1.6 µm, 2.7 µm, 0.55 µm
Tm^{3+}	YAG, silica, fluoride glasses	1.8↔2.1 µm, 1.45↔1.53 µm, 0.48 µm, 0.8 µm
Ho^{3+}	YAG, YLF, silica	2.1 µm, 2.8↔2.9 µm
Pr^{3+}	silica, fluoride glasses	1.3 µm, 0.635 µm, 0.6 µm, 0.52 µm, 0.49 µm

Table 2.1: Most common rare earth dopant used in optical fiber and optical crystals, with the common host media and the emission wavelengths.

creates a sufficient feedback inside the structure according to the principles of *Fresnel reflection*. This basic scheme, shown in Fig. 2.4(a), can be effectively used to create a *laser oscillator* using some meters of fiber amplifier and controlling the feedback at the end faces. This can be done tailoring the reflectivity using an external mirror or covering the cleaved face of the fiber with a dielectric coating. Another method, mainly used in commercial applications, involves the use of *fiber Bragg gratings*, which can be directly inscribed inside the fiber, as reflectors. This method offers a more reliable solution. Another common way to obtain a oscillator is to use a closed loop amplifier. Inside this scheme, the pump is coupled with a multiplexer, and the laser signal is retrieved through a fiber coupler, the schematic is shown in Fig. 2.4(b).

The described fiber laser sources generate a continuous wave laser emission, which is in general weak. To obtain a high power operation, it is necessary to use a more advanced option. A high gain is usually achieved using *master oscillator power amplifier - (MOPA)* scheme, also called *MOFA*, i.e. master oscillator fiber amplifier, when referred to fiber lasers. In this configuration a laser oscillator, which can be obtained with a fiber amplifier as described previously, is used as a seed input for a high power optical amplifier. The amplification section can be efficiently built using a cascade of different amplifier stages. Figure 2.5 shows an example of two stage amplification, a preamplifier and a high power amplifier. The use of multi-stage amplification is fostered because of various reasons. Having more stages, it is easier to

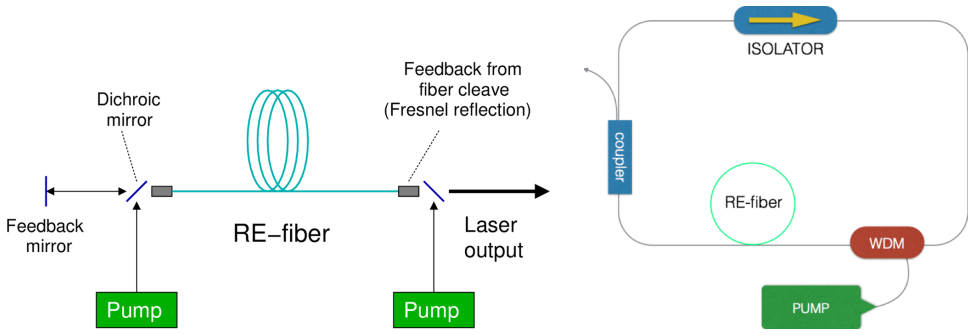

Figure 2.4: Two common laser oscillators schemes: (a) linear cavity obtained with a straight amplifier and reflectors at the ends; (b) closed loop configuration.

avoid gain saturation, making the pumping process far more efficient. Between two stages it is also possible to filter or modify the signal, or recover its polarization state [46]. Regarding to the final amplifier stage, it is important to explain that it represents the most critical part of the amplifier stage to obtain high power output. The final amplifier is responsible for the most of the power conversion between pump and signal, therefore particular attention is carried out to design it for maximizing its efficiency. The main technological breakthrough which have permitted a so rapid scaling of output power can be identified in the introduction of *cladding pumping* [47]. Cladding pumping consists in a pumping strategy where a rough high power multi-mode pump source is injected and guided inside the cladding. The part of its light intensity which overlaps with the doped core is responsible for population inversion. To improve the efficiency of this strategy a new class of *double cladding - (DC)* optical fibers has been introduced.

2.1.3 Pulsed operation

Fiber laser technology offers several key points of attraction. Not only the high average powers that can be achieved is of interest, but also the variety of output properties in the domain of time that are supported. Because of the large bandwidth offered by

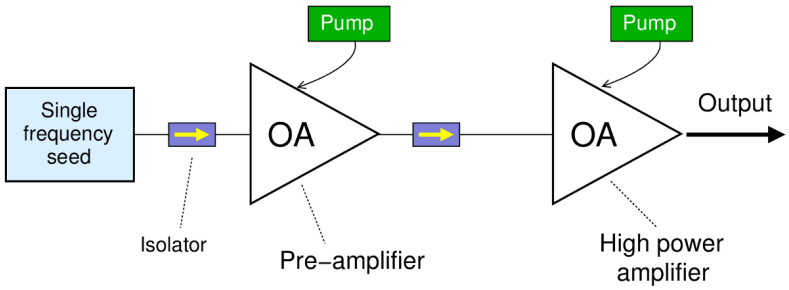

Figure 2.5: Master Oscillator Power Amplifier (MOPA) configuration, with two stages of amplification.

rare earth glasses, optical fiber lasers can be set not only to work in CW but also in pulsed operation with a large amount of possible configurations. To characterize the behavior of a fiber laser in pulsed regime, three parameters are fundamental: pulse energy, pulse duration and pulse rate. Directly derived from these parameters is the average power of pulse operation. The flexibility of fiber laser configuration permits most of the combination of pulse duration and pulse rate showing a fast increase of average power output. In a pulsed fiber laser system, pulse generation is given by the particular configuration of the laser oscillator, while it is possible to use MOPA concept to achieve significant output power, scaling the peak energy and the average power. In the amplification stage, the biggest challenge is to preserve the quality and the shape of the seed, avoiding detrimental effects like fiber non-linearities, saturation, chromatic dispersion and thermal driven distortion. In general, the goal is to preserve as much as possible the temporal and the spectral properties of the pulse train generated by the master oscillator.

In order to generate a train of pulses inside a fiber oscillator, several techniques can be used. The most common are *Q-switching* and *mode locking*.

Q-switching. The principle of Q-switching is to change the Q-factor of the cavity in order to generate a giant pulse. To obtain such operation, another component is needed in the laser cavity, a Q-switcher. Such a component can be an electrical driven acusto-optical modulator [48]. In that case, it is common to refer as

active Q-switching. In case of a passive component, like a *saturable absorber* [49, 50], it is referred as *passive Q-switching*. The basic idea in this method is to force the gain in active medium till the saturation, while the Q-switcher maintains the absorption in the cavity to a value large enough to impede the oscillation onset. The activation of the Q-switcher reduces drastically the cavity losses making the cavity to reach the lasing threshold and to generate a huge pulse which depletes the active medium. Alternating the activation of Q-switcher, which can be done with an active component or automatically exploiting the property of a saturable absorber, a train of pulses can be generated. Typically with Q-switching technique, pulses in the order of nanoseconds, with repetition rate of several kHz can be achieved. With proper amplification, several mJ are possible [51].

Mode locking. Mode locking is based on the idea to modulate a laser frequency using the same spectral distance which exists between the longitudinal modes of the cavity inside the gain band. In this way, it is possible to generate a spectral comb where every component is in phase. The beating between each component shapes a train of pulses inside the cavity. As the case of Q-switching, modulation can be achieved using an active electro-optical modulator [52] or the modulation offered by a passive component like a saturable absorber [53]. Pulse duration in mode locking configuration is typically in a range between tens of fs and tens of ps, with repetition rate of GHz. Pulse energy achievable is more moderate with respect to Q-switching.

The most critical part of a pulsed fiber laser system is the high power amplification section. The need to preserve the properties of pulses generated in the oscillator is fundamental. To achieve this result, the idea is to reduce as much as possible the impact of non-linear effects. Non-linear effects are actually proportional to the length of the optical fiber used as amplifier and inversely proportional to the *Effective Area* of the propagating mode, as well as the fiber core diameter. Basically, the solution of this problem is to design fiber amplifiers with *large mode area - (LMA)*, short length and strong gain. However, a larger core area, induces the propagation of higher order

modes in fiber, which is detrimental with respect to the quality of output beam. Furthermore, a larger core depletes thermal dispersion causing an additional distortion to the propagating modes, and causing unwanted effects like thermal lensing that again fosters the propagation of higher order modes. The challenging gaol is to design a larger core while maintaining single mode operation. Microstructured fiber and PCF offer the best solution to this problem [54].

2.2 Fiber design for high power fiber laser

The primary goal to obtain high power amplification in a fiber laser system is to preserve the beam output quality, both in CW and in pulsed operation, reducing the detrimental effects of non linearities. This concept transfers the target of fiber design in enlarging the mode area, preserving the single mode operation. Furthermore, a better pump absorption is required to improve the amplification, avoiding the onset of non-linearities during light propagation. To reach such ambitious goals, two important milestones have marked the evolution of fiber design. One is the introduction of *double cladding* fibers [47], and the other is the discover of PCF. While the former strategy design permits a better pump absorption control, fostering higher power operation, reducing the length of fiber amplifier, the latter design represents a platform to enlarge effective area of modes, finely controlling the single mode operation. Such control is impeded in normal SIF due to the technological difficulties to calibrate the index contrast [55].

2.2.1 Double cladding fibers

The idea of double cladding, which has permitted to efficiently clad pumping rare earth doped fiber amplifier, largely increasing the output power, is to build a fiber with two different collinear cladding, one internal, the *inner cladding*, also called pump cladding, and another one external, the *outer cladding*. As shown in the schematic of Fig. 2.6(a), the outer cladding refractive index is substantially lower respect to the index of inner cladding, while as usual, core refractive index is the highest one. In this configuration, the couple of core and inner cladding acts like a normal SIF for the

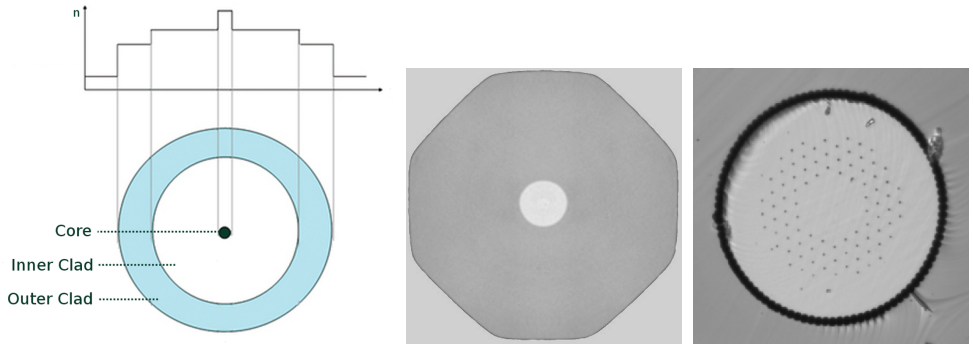

(a) (b) (c)

Figure 2.6: Double cladding configuration: (a) double cladding schematic and typical index profile; (b) Yb-1200-25/250 double cladding SIF produced by nLight, notice that the inner cladding has octagonal shape and the outer cladding is made of a low-index polymer coating; (c) typical large mode area double cladding PCF, with air-cladding.

signal to amplify, while inner cladding plus outer cladding offer a large waveguide to propagate the pump. Refractive indices are chosen in a way that index contrast between core and cladding is low to guide signal in single mode regime, while index contrast between inner cladding and outer cladding is much higher to guide the pump in multi-mode regime. Typically, numerical aperture of the couple core inner-clad is $NA_1 < 0.1$ and the numerical aperture between inner-clad and outer-clad is $NA_2 > 0.46$. In addition to dopant concentration, pump absorption efficiency depends on the overlap between the group of cladding modes and the core region, so it also depends on the ratio between core and inner cladding areas. Double cladding SIFs are commercially available with different solutions and different inner cladding shapes, to maximize the cladding mode distribution over the pump cladding area. Figure 2.6(b) shows an example with octagonal pump cladding. Outer cladding in such fiber is obtained using a low index acrylate [56] , with the double function to guide the pump and to coat the fiber.

In microstructured fiber, like PCF it is more common, mainly to improve the fab-

rication process, to obtain double cladding using the *air cladding* solution. In PCF outer and inner cladding are typically made of pure silica, while the guidance properties are given by a holes lattice. To obtain the pump cladding is therefore created a larger ring of air hole which surrounds the holey cladding. Every hole, in the air cladding ring is separated by a thin silica bridge. Even if air cladding is usually not so thick, like few μm, the confinement of pump modes is pledged by the strong index contrast between air and silica. An example of double cladding PCF with air cladding is depicted in Fig. 2.6(c).

2.2.2 LMA fiber designs

Enlarging mode area is not a trivial job. Considering a SIF and looking at the definition of $V-$number 1.7, it is possible to notice that increasing core area, V increases as well. Since V is strictly related to the number of modes, supported by the structure, the fiber loses its single mode operation, becoming a multi-mode fiber. It is possible, in principle, to operate on the index contrast to maintain constant $V-$number, but this has a strong limitation which derives from the fact that refractive indices of the doped glasses, used in fiber, can not be engineered with an infinite precision. Technologically, it is difficult to achieve very low core aperture number NA_1, and values less than 0.06 are not available for rare earth doped fiber [57]. Such value allows a core diameter which can not overstep a maximum of 13 μm for operation in the region of ytterbium emission. Commercially larger core SIF are available, with value of core diameter around 30 μm. In these fibers, which support a small number of modes and are called *few modes fibers*, single mode operation is recovered imposing bending loss in the structure [58]. This is a good solution which anyway suffers by a further limitation. In a bent fiber, the mode scalability in order to maintain the same modal properties is proportional to the cube of bending radius [59]. This implies that, for larger core diameter, the guidance, and consequently bending loss, of all the modes becomes more sensible to small variation of bending radius. Furthermore, gaussian shape of fundamental mode results in strong distortion.

Considering the limitations of SIF design to achieve larger mode area, a better approach is the use of solid core microstructured fibers or PCFs. The nature of this class

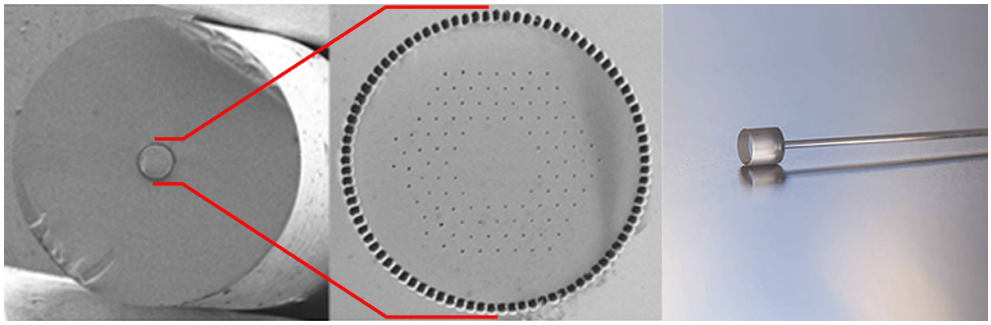

Figure 2.7: Rod-type PCF. This fiber is rigid because the presence of an outer cladding diameter larger than 1 mm.

of fibers, and the possibility to operate on lattice parameters to finely tailor the index contrast, give the opportunity to dramatically increase the core diameter, preserving robust single mode operation [28]. With the use of PCFs, *very large mode area* fibers, i.e. fibers where mode field diameter is more than 50 time larger than operation wavelength [54], are possible. Not only, the degrees of freedom in PCF design are not limited to the main lattice parameters: holes diameter d and pitch between holes Λ. As a result, more specialized and effective designs are possible. Treating with very large core diameter, high loss in guidance due to the bending remains a serious problem. In some fiber design, this issue is bypassed avoiding bending with the use of a particular type of rigid structures known as *rod-type fibers* [60]. A rod fiber is a PCF structure where the outer silica cladding is enlarged till more than 1 mm of diameter making the fiber unbendable. As this kind of fibers shall be used straight, their length is maintained short typically 1 m, while their doping is quite high to ensure a good amplification. An example of rod-type PCF is shown in Fig 2.7.

In present days, special fiber designs, with the aim to enlarge as much as possible mode area, have reached remarkable results, in particular fiber design suitable for ytterbium doping. Microstructured PCFs offer the best solution, however other designs, which exploit different principles, are proposed. Here is an overview of the most effective and promising LMA designs.

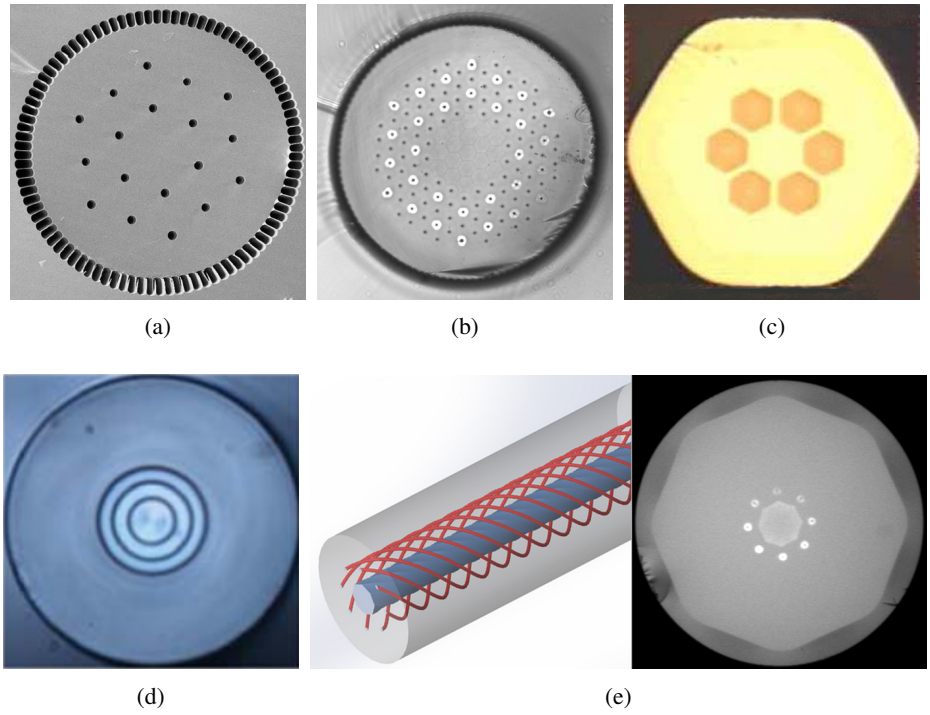

(a) (b) (c)

(d) (e)

Figure 2.8: Large mode area fiber design: (a) Yb-doped LPF with 135 µm core diameter; (b) Yb-doped DMF-PCF with 85 µm produced by NKTPhotonics; (c) Yb-doped LCF with 50 µm core diameter; (d) MTF design with 30 µm optimized for 1 µm operation, larger cores are possible; (e) Yb-doped CCC with 55 µm core diameter.

Large Pitch Fibers - (LPFs). This family of PCF has the characteristic to have a large space between the holes, at least 10 times larger than the operation wavelength, so this design strongly exploits the concept of mode sieve. The guiding principles are the same of a normal PCF, while the HOMs delocalization is assisted by avoided crossing with cladding modes [61]. HOMs delocalization creates a differential between FM overlap and HOMs overlap with the doped core. Single mode operation inside an amplifier is obtained for the different gain that each mode experiences during propagation. Typically, LPF fiber is

build with a rod support, because bending would have detrimental effects on FM guidance. With this design, a ytterbium doped LPF-based amplifier with core larger than 100 µm has been demonstrated [62, 51]. A LPF with 135 µm core diameter is shown in Fig. 2.8(a).

Distributed Mode Filtering PCF - (DMF-PCFs) This fiber, which is produced by NKTPhotonics and is commercially available, uses the principle of higher order modes delocalization. This delocalization is obtained exploiting a particular mechanism of mode filtering [63]. Inside the lattice of holes, some of them are surrounded by a higher refractive index ring, made of silica doped with germanium. The effect of these features is to increase the guidance of some cladding modes in a particular range of wavelength. Consequently, guided core modes can couple with the cladding modes of the germanium features. Geometrical parameters of this fiber can be arranged to delocalize only the HOMs, while maintaining FM well confined in the core [64]. NKTPhotonics uses this design with 85 µm core diameter in their Yb-doped rod amplifiers, cross section is depicted in Fig. 2.8(b).

Leakage Channel Fibers - (LCFs) Respect to the previous analyzed microstructured design, this one is not based on the properties of a holey photonic crystals. Instead, the fiber is structured with a core surrounded with one or two ring of low index fluorine doped glass. The structure is very open and the principles of higher order mode suppression is based on the differential losses experienced by core modes [65]. With the proper parameters settings, like the distance between fluorine rods and their doping, it is possible to obtain a good guidance of fundamental mode while HOMs suffer of strong losses. In the amplification process, only FM can survive. HOMs losses are usually assisted by bending. An advantage of this all-solid fiber design is the ease to integrate it in a all fiber system amplifier, since it is more simple to splice a solid fiber respect to a PCFs. With this design ytterbium doped fiber amplifiers with core diameter of more than 50 µm have been demonstrated [66]. An example of LCF is shown in Fig. 2.8(c).

Multi Trench Fibers - (MTFs) This fiber design, recently proposed [67], has the undeniable advantage to posses circular symmetry and, as a consequence, it offers the possibility to be easily fabricate with *modified chemical vapor deposition (MCVD)*. The fiber consists of one or more concentric rings of lower index glass, called trenches. The principles of HOMs suppression is based on the concept of mode delocalization. Theoretically, a proper arrangement of the trenches distance permits single mode operation in ultra large core fiber of 140 µm diameter at around 1 µm wavelength, [67]. Practically, remarkable results have been demonstrated with fibers of 90 µm core diameter [68], in rod-type configuration, and 30 µm core diameter for coil arrangement [69]. An example of MTF with three trenches is depicted in Fig. 2.8(d).

Chirally Coupled Core fibers - (CCC) As the previous one, also this fiber design is remarkable for its simple all-solid structure. The cross section consists in a ytterbium doped core surrounded by eight germanium satellite small cores. The originality respect to a normal cylindrical structure is given by the fact that this side cores are twisted in the longitudinal direction, Fig. 2.8(e). The operation principles is to enhance HOMs losses fostering their coupling with satellite cores, which present higher losses due to their twisted configuration. With such fiber design, single mode operation has been demonstrated with core diameter larger than 50 µm [70].

2.3 Region of 2 µm operation

The huge scientific interest in developing emitting source around the wavelength of 2 µm can be motivated by the large amount of discoveries of novel light-matter interaction and light propagation phenomena in this region. In addiction, the wide range of existing and potential applications, that can be developed using laser light at 2 µm, is further pushed by the eye-safe nature of such wavelength. In present day, a number of successful applications were reported, and most of these are or can be successfully implemented using fiber laser technology. In the family of rare earth doped glasses, *thulium doped amplifiers (TDFs)* are an excellent candidate to be the paramount so-

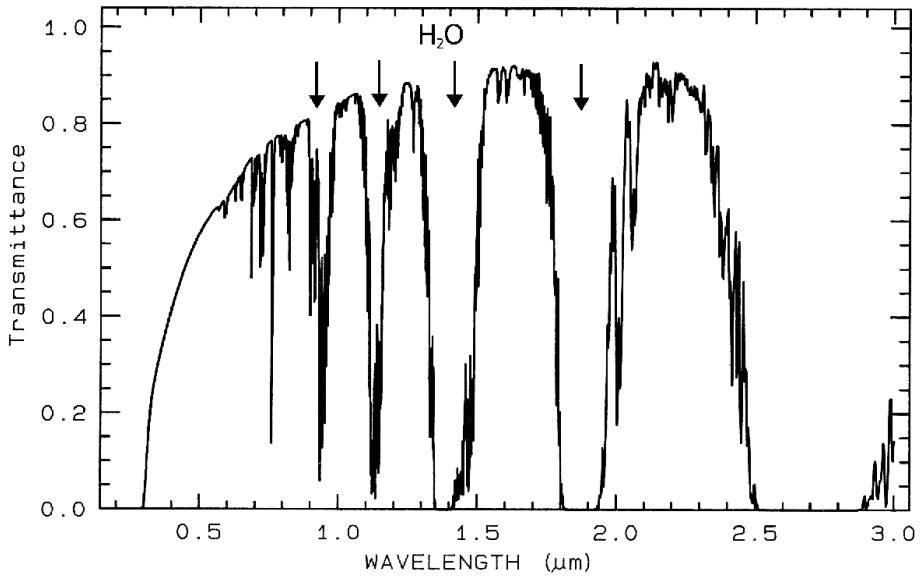

Figure 2.9: Transmittance of middle latitude summer atmosphere. Main water absorption windows are marked with an arrow.

lution for suppling a suitable platform [43]. In particular, thulium doped glasses offer a wide emission range from 1.8 µm to 2.1 µm and can be pumped with a low-cost, efficient and commercially available laser diode emitting at 793 nm. Although thulium energy conversion efficiency is not so as high as ytterbium, the solutions achieved in fiber laser technology in the region of 1 µm, in particular exploiting the versatility of DC-PCFs, are pushing the use of thulium doped fiber for covering the needs in the field of 2 µm. The main applications are related to some important properties of 2 µm region. The first is the transparency atmospheric window which extends from 2.025 µm to 2.25 µm, Fig. 2.9. The second is the peak of water absorption at 1.94 µm [71]. A third reason of interest in thulium doped fiber laser, which is not strictly related to the 2 µm region, is due to the wide band of thulium emission that offers several potential in communications. Followings are the short overview of the applications offered by thulium doped fiber technology.

Medical applications. The vibrational reaction of O−H bond to the wavelength of 1.94 µm is the main reason which is promoting research toward the improvement of thulium doped laser sources, both in terms of power and in terms of beam quality. In the field of surgery, it is clear the importance to have clean incision with low carbonization and high ablative properties. Remarkable results with the use of Tm-doped fiber lasers have already been obtained, in urology [72, 73, 74], in skin disease treatment [75], and in internal surgery [76, 77]. Furthermore, the geometry of fiber is well suitable for endoscopy purpose [78].

Remote sensing. LIDAR, which is the acronym for light detection and ranging, is a tool operating with the same principles of microwave radar, with the advantage of much more resolution and accuracy because of the use of shorter wavelength. Furthermore, the use of a laser source, with the possibility to tailor CW or pulsed operation at different levels, gives a huge versatility in the use of LIDAR systems. However, atmospheric propagation, in particular absorption from H_2O and CO_2 is detrimental for LIDAR performance. Windows of transparency around 2 µm offers a better option respect to 1 µm region [79].

Military application. In this field, an intense light is required for directed energy applications and propagation over long distances. Fiber lasers emitting at 1 µm have been used to detonate land mines or unexploded bombs [80]. All of these applications need a near-diffraction limited beam. Light emitted by a 2 µm fiber lasers cannot pass through the retina, so it is much more safer than lasers operating at shorter wavelengths.

Supercontinuum generation. The possibility of generating ultra short pulses in the range of tenth of fs with high average power, combined with the strong and efficient amplification, offered by double cladding fiber laser system, are extremely interesting in the field of supercontinuum generation. With the advantage to offer wide amplifier bandwidth and large dispersion thulium doped fibers foster near linear amplification for supercontinuum source in Mid-IR range [81, 82].

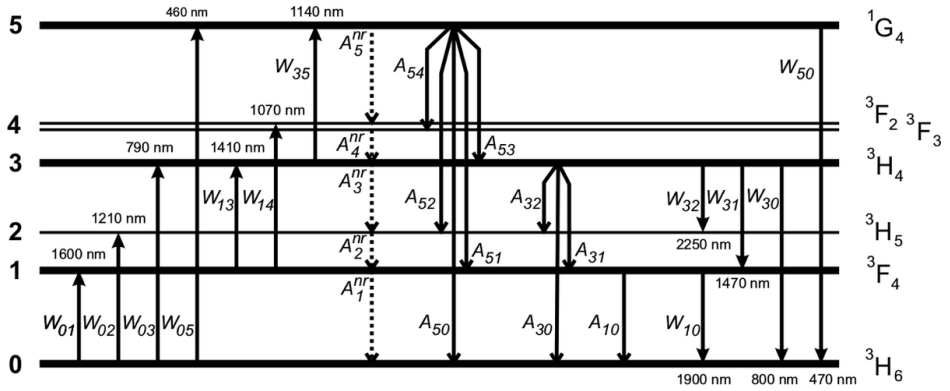

Figure 2.10: Thulium energy level diagram with all transitions involved in the model.

Telecommunication. In the field of optical communications, the key role is occupied by the use of erbium doped fiber mainly for the fact that amplification is in the window of minimum loss of silica transmission medium, i.e. 1.55 µm. Nevertheless, thulium doped fiber has the advantage to dispose of a wide band of amplification that spans over 30 THz, offering the possibility to host multi mode, multi channel transmission, improving significantly the data throughput. It is clear that a long transmission optical system based on silica fiber is not suitable to work around 2 µm because of the high loss of silica, but a local area network can exploit quite well the properties of TDF. Furthermore, considering future improvement of hollow core optical fiber technology, with loss minimum around 2 µm, the combination with thulium amplification can open a new outlook in long range communications [83].

2.3.1 Thulium doped fiber amplification

Thulium doped glass has a quite complicated energy scheme, far more complex with respect to the one of ytterbium, involving several energy levels and showing effects like cross-relaxation and up-conversion [84, 85]. The mechanism of absorption and emission is complex, however in general can be modeled with a quasi-three levels

system. The main process of amplification involves four levels: the ground level $^3H_6$, the excited states $^3F_4$, $^3H_5$ and $^3H_4$. In this process, the pump radiation, at 790 µm, excites electrons from ground $^3H_6$ to level $^3H_4$. A fast, non radiative, decay brings electrons from level $^3H_4$ to level $^3F_4$ directly or passing through level $^3H_5$, in both cases fluorescence lifetime is small compared to the lifetime in level $^3F_4$. From this level, a radiative event, for spontaneous or stimulated emission, can bring back electrons to the ground state, emitting photons with wavelength ranging from 1800 nm to 2100 nm. The mechanism described is modeled with the following system of equations:

$$\frac{dN_0}{dt} = \sum_{i=1}^{3} A_{i0}N_i + \Gamma_1 N_1 - W_0 3 - CR_1 - CR_2 + \Big(S_f(z) + S_r(z)\Big)\Big(\sigma_e(\lambda_s)N_1 + \sigma_a(\lambda_s)N_0\Big)\,, \tag{2.11}$$

$$\frac{dN_1}{dt} = \sum_{i=2}^{3} A_{i1}N_i + \Gamma_2 N_2 - \big(A_{10} + \Gamma_1\big)N_1 + 2CR_1 + 2CR_2 - \Big(S_f(z) + S_r(z)\Big)\Big(\sigma_e(\lambda_s)N_1 + \sigma_a(\lambda_s)N_0\Big)\,, \tag{2.12}$$

$$\frac{dN_2}{dt} = A_{32}N_3 + \Gamma_3 N_3 - \left(\sum_{j=0}^{1} A_{2j}\Gamma_2\right)N_2 - CR_2\,, \tag{2.13}$$

$$\frac{dN_3}{dt} = W_{03} - \left(\sum_{j=0}^{2} A_{3j}\Gamma_3\right)N_3 - CR_1\,, \tag{2.14}$$

where pump absorption is given by the term W_{03}:

$$W_{03} = \sigma_a(\lambda_p)\Big(P_f(z) + P_r(z)\Big)N_0\,. \tag{2.15}$$

In the previous equations the terms P_f, P_r, S_f and S_r represent the pump and the signal field in both directions of propagation. The terms A_{ij} are the spontaneous transition rate from every level, σ_a and σ_e are the cross-section of absorption and emission respectively, finally the terms Γ_i take in consideration the rate of non radiative transition. A more ample discussion shall be done on the coefficients CR_1 and CR_2, which represent the cross relaxation effects. A cross relaxation can be defined as an upgrade transition stimulated by a non radiative decay. The amount of cross relaxation can be

described with the following equations:

$$CR_1 = k_{3101} N_3 N_0 - k_{1310} N_1^2 , \tag{2.16}$$

$$CR_2 = k_{2101} N_2 N_0 - k_{1012} N_1^2 . \tag{2.17}$$

The most important between these two cross relaxation events, considering the mechanism of pumping under investigation, is the first one, which represents the upgrade transition between the level $^3H_6$ and the level $^3F_4$, stimulated by the non radiative decay between $^3H_4$ and the level $^3F_4$. The total effect of cross relaxation is, in principle, to populate the level $^3F_4$, the one involved in the laser emission, with two electrons every pump photon absorbed. In practice, this effect is relevant only for high thulium doping concentration, which exceeds 2.5 wt.%. Such a high concentration increases the index contrast between doped silica and pure silica, decreasing the flexibility in fiber design [43]. In the region of low doping, under 2.5 wt.%, the effect of cross relaxation can be neglected and the thulium doped system can be modeled as a simplified three level system, where the main effect is given by the cross sections of absorption and emission, as depicted in Fig. 2.11. It is worth noting the presence of a wide cross-section of absorption centered in 1600 nm, which partially overlaps the emission cross-section centered in 1850 nm. This absorption region partially reabsorb the amplified signal, decreasing the level of gain.

Thulium doped fibers, nevertheless their huge potential, suffer from a big issue that makes their use quite inefficient with respect to ytterbium, which is in general preferred in high power applications where emission wavelength is not a key requirement. As stressed previously, the mechanism is basically, an absorption at 790 nm and an emission around 2 µm, with a lot of non radiative emission in between, which in general is dissipated as vibrational motions, called phonons, inside the structure. Even if a part of these phonons can be absorbed again through the cross-relaxation mechanism, in the case of high doping, most of them contribute to the thermal load generated inside the doped region. To quantify this detrimental effect, it is possible to introduce the definition of *quantum defect*:

$$q = h\nu_p - h\nu_s = h\nu_p \left(1 - \frac{\lambda_p}{\lambda_s} \right) , \tag{2.18}$$

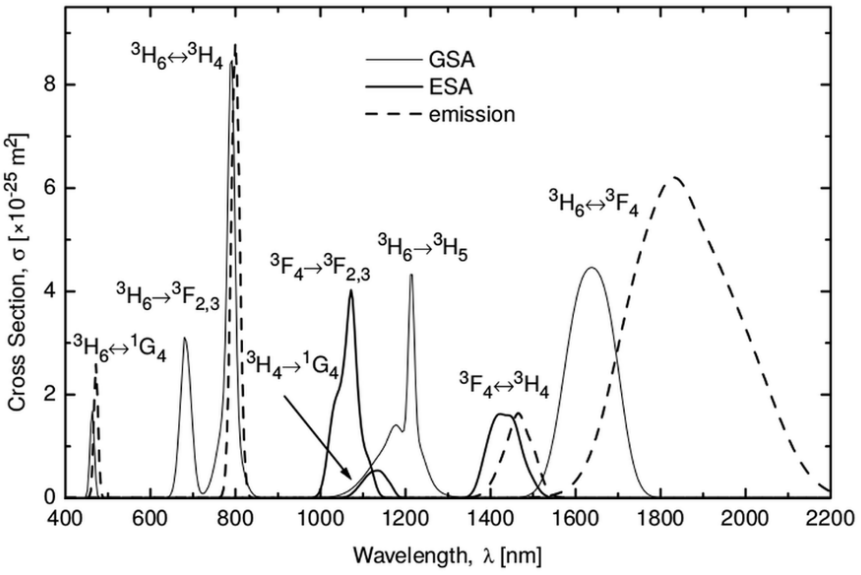

Figure 2.11: Thulium cross section of emission and absorption. The thin solid line represents the ground state absorption (GSE), while the thick solid line the excited state absorption (ESA).

where $h\nu_p$ is the energy of a pump photon, and λ_p and λ_s are the wavelength of the pump and the signal respectively. As it is possible to see from the definition, quantum defect normalized by the pump energy is, in the worst case not considering cross relaxation, roughly equal to 0.60 for thulium, which means that 60% of pump energy is converted in thermal load. Compared to the value obtained for ytterbium, more or less 8%, this value is extremely high. This high thermal load is one of the main problem to overcome in a lasers system using thulium doped fiber, not only because high temperature can damage the fiber, but also because the temperature gradient between core and cladding changes radically the guidance properties of the fiber.

To explain how thermal load is influencing the guidance of fiber, it is mandatory to model the thermal diffusion inside the fiber structure. To do that, some assump-

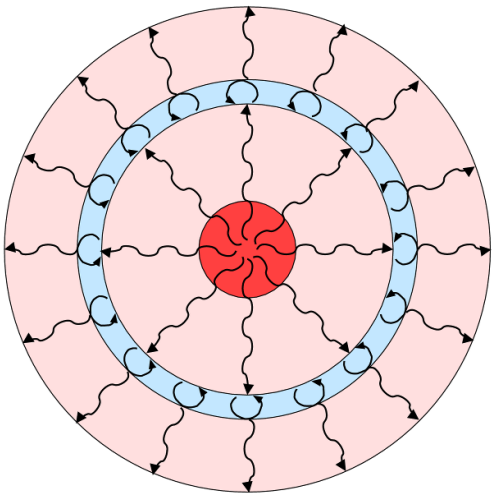

Figure 2.12: Schematic of heat diffusion in a large mode area DC-PCF. In the solid core, inner and outer cladding heat load diffuses by conductivity. In the air cladding otherwise the mechanism of heat transfer is due by air convection.

tions and simplifications shall be done. At first, it is supposed to work with a large mode area, double cladding PCF, i.e. a fiber which is specially designed to have a large core and to support single mode operation. The fiber can be assumed to be a structure made with concentric layers, a schematic is shown in Fig 2.12, each of them with different thermal properties [86, 87]. The solid doped core is the heat generator because phonons are produced only in the doped region. The holey cladding can be considered also as solid, in fact in a single mode operation PCF, holes are small and their impact on heat diffusion is negligible [88]. Doped core and cladding are described by the same coefficient of thermal conductivity of the pure silica. Air cladding, if included in the structure, shall be treated as a region of air convection. The interface of the fiber surface with the ambient represents the boundary condition for the differential problem of heat diffusion, with a constant temperature fixed by the method chosen to cool down the fiber, as an example air convection, or cold water. Another important assumption is that, heat diffusion is only radial and not longitudi-

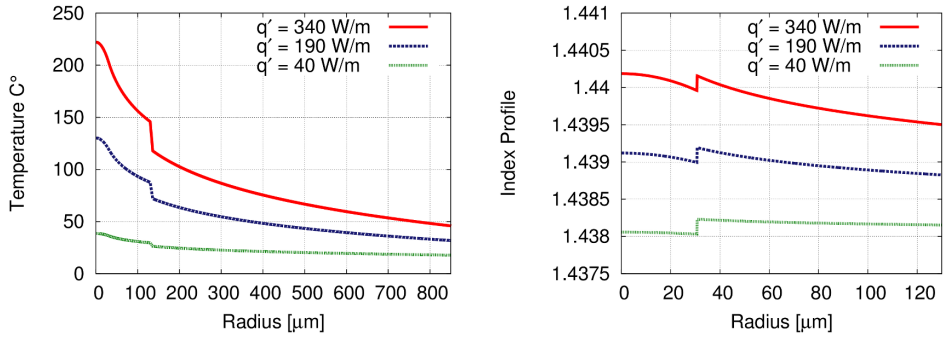

(a) (b)

Figure 2.13: (a) An example of temperature profile in a LMA DC-PCF, with core diameter of 32 µm, and inner cladding diameter of 130 µm, calculated with three different heat densities over the core area. Notice that the core is down-doped. (b) index profile variation caused by temperature gradient.

nal. The differential equation which characterizes the heat diffusion can be written in cylindrical coordinates as follows:

$$\frac{1}{r}\frac{\partial}{\partial r}\left(r\frac{\partial T(r)}{\partial r}\right) = -\frac{Q}{k_i}, \tag{2.19}$$

where T is the temperature, Q the heat power density and k_i the thermal conductivity of each material in the concentric rings multilayer.

Solving the equation Eq. (2.19), imposing the heat load generated by quantum defect in the core and imposing the boundary conditions, the temperature profile can be easyly calculated. The temperature assumes a parabolic profile in the core and a logarithmic decay in the cladding, as shown in Fig. 2.13(a). The temperature gradient is the main reason for refractive index change, according to the thermo-optic effect given by the following formula:

$$\Delta n = \beta\left(T - T_0\right), \tag{2.20}$$

where T_0 is the reference temperature of the environment, typically 25 °C, and β is the thermo-optic coefficient of the silica, whose value is 1.16×10^{-5} K^{-1}. This parabolic

increase of refractive index of the core is known as *thermal lens*, the effect is shown in Fig. 2.13(b). A strong thermal lens effect can dramatically change the guidance properties in the fiber, pushing a single mode fiber to become multi-mode.

Large mode area fiber design proposed for high power thulium doped laser, usually are scaled versions of designs successfully used for operating in ytterbium doped systems [89, 90, 91]. Due to the strong impact caused by thermal lens, simply scaling a Yb-optimum design is not the perfect solution. Furthermore, regarding flexible fibers, index profile variation caused by bending effects impedes to directly apply the scaling law. For these reason, it is clear that fiber design, operating at 2 µm, with thulium as dopant, requires a specific calibration to obtain the best results.

Chapter 3

Polarization maintaining LMA Tm-dopded fiber design

In this chapter, flexible thulium doped *polarization maintaining (PM)* fiber designs with a core of 80 µm are presented. A commercial PM-PCF, designed to work in 1 µm region, has been scaled for 2 µm region obtaining an 80 µm diameter core. The fiber has been numerically analyzed with the help of a full vectorial Finite Element Method (FEM) based software, varying the bending radius from a value of 60 cm to 20 cm. Starting from the issues emerged analyzing this fiber, a new LMA PM-PCF has been designed and numerically investigated. The new fiber has the same core diameter of 80 µm. Holes arrangement has been achieved in agreement with the stack-and-draw technique, which guarantees an easy and cheap fabrication. Birefringence is obtained inserting, along the slow axis, two symmetrical boron doped stress applying parts (SAPs). With this expedients, the new fiber is able to achieve a single mode, single polarization operation with a doped core overlap higher than 0.85 and with low propagation losses in a range of bending radius between 33 to 40 cm. The disadvantaged polarization of FM and the most significant HOMs are effectively suppressed.

3.1 Overview on PM TDF

In recent time, the laser around 2 µm operation is gaining interest in the scientific community, thanks to its intrinsic property to be eye-safe and thanks to the several applications that can be developed in this region. Water absorption which is particularly strong at 1.94 µm is of interest both in soft-tissue medical applications and laser imaging detection and ranging (LIDAR). The window of high atmospheric transparency at 2.02-2.25 µm instead can be efficiently used in remote sensing, communications and industrial processing [43]. Thulium doped fibers can be considered a good solution to supply amplification in the 2 µm region, offering a wide spectrum of emission between 1.8 µm and 2.1 µm and absorbing at 790 nm which is a wavelength covered by commercially available photo-diodes.

It is possible, in principle, to scale the existing 1 µm fiber designs to make them working in 2 µm region, but the result is in general not efficient for a number of reasons. First of all, thulium suffers for a higher quantum defect with respect to ytterbium, so laser operations inducing a considerable thermal load in the fiber core are affected by thermal lens effect [92]; secondly, in case of flexible fibers, the bending effects can be detrimental to single mode operation also considering large bending diameter [59]. Focusing on the latter drawback, the simplest solution is to avoid bending, designing fiber that are artificially straight. This solution is implemented creating a solid silica outer cladding of more than 1 mm . This class of fibers, known as rod-type fibers, quite common in ytterbium doped fiber design, has been recently investigated also with thulium doping [91, 89]. It is obvious that such solution is quite effective, but it excludes all those types of fibers which get benefit from bending in their operation, in particular the polarizing maintaining (PM) fibers where a single mode and single polarization operation can be obtained tunning the bending radius with the birefringence caused by the induced lateral stress [93, 94]. A PM fiber is extremely useful when it is necessary to amplify a polarized input seed or when it is necessary to clean the seed from its spurious polarization, obtaining a high quality output beam. Furthermore, working with a flexible fiber offers operational advantages related to the best choice of fiber length and related to the compactness of the

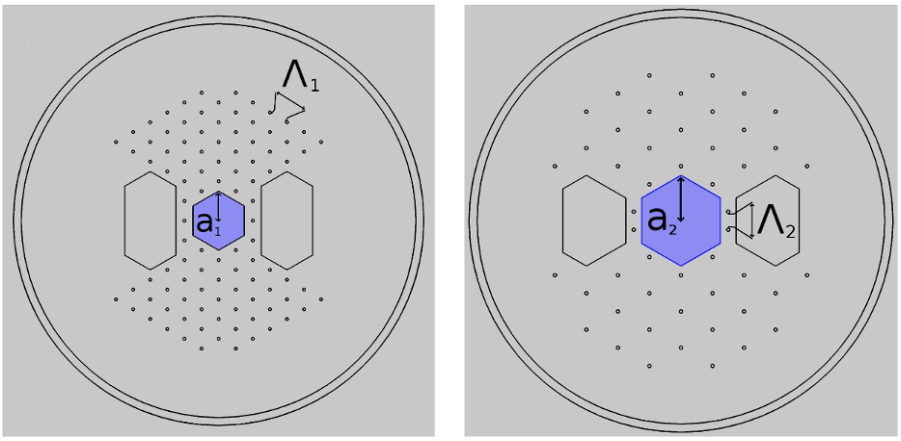

(a) (b)

Figure 3.1: Cross-section of the fibers under examination: (a) scaled version of a commercial PM-PCF largely used for 1 µm operation; (b) new thulium doped PCF.

experimental setup. Unfortunately, very few thulium doped PM fiber designs have been proposed in literature [90].

3.2 Fibers design

3.2.1 Fibers cross sections

Cross-section schematics of the PCFs analyzed in this contribution are shown in Fig. 3.1(a) and (b). A commercial PM-PCF, originally optimized for 1 µm region, has been scaled to work in 2 µm region. This fiber is depicted in Fig. 3.1(a). The structure is composed by an ensemble of hexagonal cells following the technique of stack-and-draw. The core is obtained substituting the innermost 7 cells with thulium doped silica cells. The pitch Λ_1 is defined as the minimum distance between two holes and its value has been fixed to 20 µm. As a consequence, the core diameter, considering hole-to-hole distance, is 80 µm. The thulium doped region can be approximated as an hexagon with side equal to 30 µm. The cladding is composed by 6

holes rings partially closed in order to house boron doped SAPs. The ratio between hole diameter and pitch d/Λ_1 is equal to 0.18. An air cladding with thickness of 6 µm and a radius of 200 µm has been placed. The substrate is pure silica with refractive index $n_{Si} = 1.4381$ calculated at 2 µm. Core index has been considered down-doped by a value of -2×10^{-4} respect to silica. SAPs has been considered with a realistic boron doping level which has been chosen to be 16 *wt %*. At this concentration of boron the SAPs refractive index has a value of -6×10^{-3} with respect to pure silica.

In Fig. 3.1(b) is shown the new fiber design. Like the previous one, this fiber design is based on a triangular lattice, following stack-and-draw cells arrangement. The core is obtained substituting the innermost 19 cells with thulium doped silica. The pitch Λ_2 corresponds to the cell-to-cell distance, and its value has been fixed to 13.4 µm, therefore the core diameter is 80 µm. The thulium doped hexagonal region has side equal to 33.5 µm. The cladding is composed by four holes rings, where the outermost ones are partially filled because of the presence of SAPs. The distance between the holes is equivalent to the doubled cell-to-cell distance except for the holes positioned between core and SAPs. The parameter d/Λ_2 has been fixed to 0.18. Boron doped SAPs occupy a trapezoidal region along the slow axis of the fiber. The air cladding has thickness of 6 µm and diameter of 150 µm. The refractive index of the silica and the SAPs parameters are the same as the previous illustrated design while core index, supposing a proper co-doping, has been matched with respect to silica value.

3.2.2 Numerical analisys

The numerical analysis has been performed in two separated steps, the first one involves the calculation of the anisotropic refractive index change induced by SAPs while in the second one the new refractive index tensor is used in the solution of Maxwell equation via FEM. Elasto-optic effect induced by stress can be described

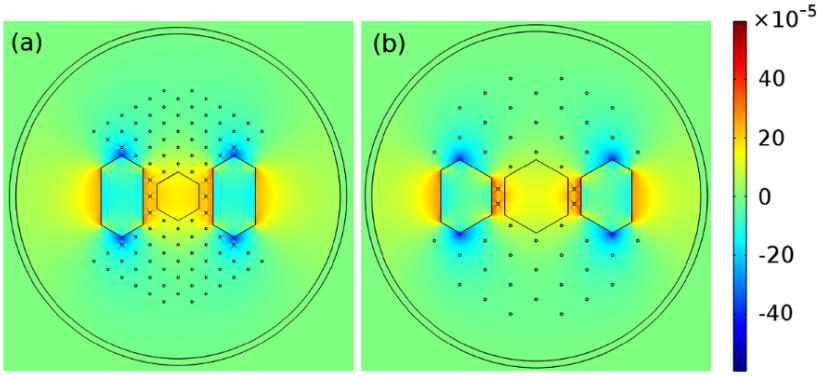

Figure 3.2: Birefringence distribution over PCF cross-section under analysis: (a) scaled version of a commercial PM-PCF; (b) new thulium doped PCF.]

by the following model:

$$-\nabla\sigma = -\nabla\cdot\left(\begin{bmatrix}\varepsilon_x\\ \varepsilon_y\\ \gamma_{xy}\end{bmatrix} - \begin{bmatrix}\alpha\\ \alpha\\ 0\end{bmatrix}(1+\nu)(T-T_{ref})\right) \tag{3.1a}$$

$$\Delta n = -C\sigma \tag{3.1b}$$

$$B = (C_2 - C_1)(\sigma_1 - \sigma_2) = n_x - n_y \tag{3.1c}$$

where σ is the stress tensor, ε_x ε_y γ_{xy} are the strain components, ν is Poisson's ratio, α is the silica coefficient of thermal expansion (CTE), T is the annealing temperature, T_{ref} is the room temperature, $C_{1,2}$ are the photoelastic coefficients. For the physical meaning and the values of these coefficients, it is possible to see references [93] and [94] with the only exception of boron doped glass CTE which is strongly dependent on the level of boron concentration, in agreement with the concentration used in this work, its value is fixed to $18.5\times10^{-7}\,\mathrm{K}^{-1}$. With this value of SAPs CTE, the birefringence B assumes the distribution shown in Fig. 3.2(a) and (b), referring to both PCFs proposed in this work. It is possible to notice that birefringence is well distributed over the core region with a value that roughly ranges from 1×10^{-4} to 2×10^{-4}. In the case of the scaled design, Fig. 3.2(a), birefringence is stronger respect to the

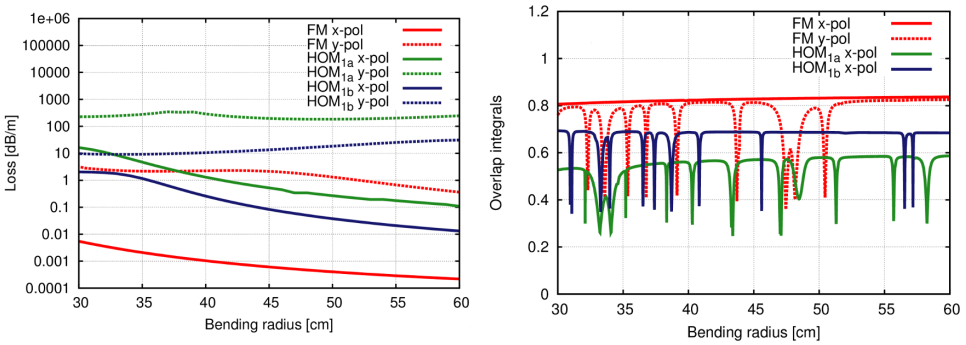

(a) (b)

Figure 3.3: Cross-section of the fibers under examination: (a) scaled version of a commercial PM-PCF largely used for 1 µm operation; (b) new thulium doped PCF.

new fiber, Fig. 3.2(b), because of the larger ratio between SAPs size and core diameter. Nevertheless, the birefringence achieved in the new fiber is enough to obtain an effective single polarization as depicted in the last part of this section. The second step of numerical analysis involves the calculation of mode properties. Bending losses have been calculated by removing the air cladding and solving for the complex propagation constant. In principle, this method gives a good picture of the modal properties, but it is incomplete and in such a way an ideal case, because it considers an infinitely extended cladding. In DC LMA the reflection due to the air cladding strongly enhances the interaction between cladding modes and core modes, generating phenomenona like anti-crossing, fostering in fact the confinement of HOMs and weakening single mode operation [61]. So a second analysis has been done on the complete cross section calculating modes overlap integral with the doped core. Overlap difference between FM and the other modes gives an important information about modes discrimination. In principle, FM overlap greater than 0.8 and an overlap difference between FM and the other modes larger than 0.25 can be considered a good index of single mode operation.

With these operational principles the fiber shown in Fig. 3.1(a) has been inves-

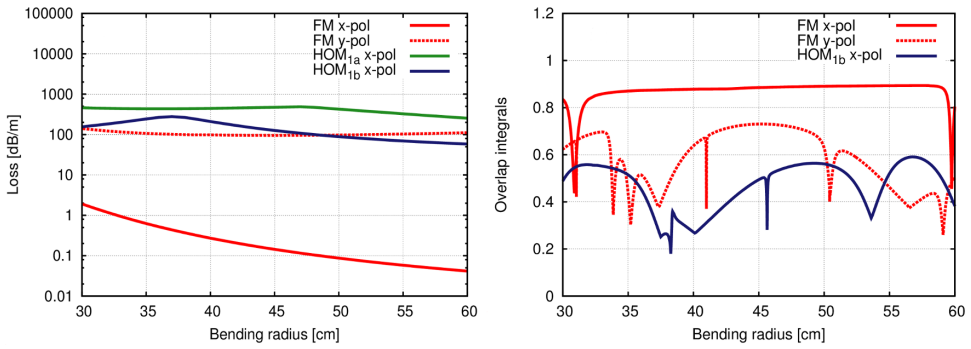

(a) (b)

Figure 3.4: New fiber numerical results: (a) losses of FM and first HOM components, some first HOM components are not shown because the impossibility to distinguish them from cladding modes, their loss value is extremely high; (b) overlap integrals of FM components and the most detrimental fist HOM components.

tigated. Results are shown in Figs. 3.3(a) and (b). From Fig. 3.3(a) it is possible to notice the x-pol of the FM, i.e. the polarization with electric field oriented along the slow axis, has low losses while the y-pol of FM and the components of the first HOM suffer larger losses. This situation is critical, because the FM y-pol and HOM_{1b} x-pol, i.e. the component of the first HOM with its lobs along the slow axis, show losses around 2-3 dB/m that is not enough to justify their suppression, in particular in a fiber with high dopant concentration and strong amplification. In principle the situation can be improved shrinking the holes or imposing more bending, making all the modes more lossy. However, as shown in Fig. 3.3(b), FM overlap is near the limit of 0.8 and some HOM's component has high overlap too, with differential overlap less than 0.2. Any further attempt to decrease HOMs content would compromise also FM integrity and its near gaussian shape. It is worth noting that bending induce several anti-crossing effects not observable in the loss analysis of Fig. 3.3(a), leading HOMs of the same LP_{xy} family to interact and exchange their role.

Starting from these observations, the new design has been developed. In the new

fiber, Fig. 3.1(b), a larger ratio between core area and doped area, has been achieved using a 19-cells design. Such solution decreases also the relative distance between core and SAPs improving birefringence. To counteract the HOMs confinement, in particular the component of the first HOM with lobes shielded by the lower index of SAPs, a more open structure has been realized, with a larger distance between holes, less holes rings, and with SAPs that occupy smaller angular portion. To improve the circular shape of the FM, two small distance holes between core and SAPs have been placed. This solution is trade-off between the the x-polarization confinement given by the higher refractive index induced by birefringence and the larger modes sieve given by the looser holes lattice.

Results, shown in Figs. 3.4(a)-(b), confirm the effectiveness of the new design. From Fig. 3.4(b) it is possible to see that FM overlap is larger than 0.88 for bending radius larger than 32 cm while the most detrimental HOM component overlap is under 0.6. Furthermore, it is possible to see the disadvantage polarization of FM become extremely lossy, showing an overlap which is in general less than 0.72 and lower than 0.63 in the optimum operation window between 33 cm and 40 cm . This choice of leaky structure has a considerable impact on modes loss. As Shown in Fig. 3.4(a), loss of FM y-pol and loss of first HOM most detrimental components has moved over 100 dB/m while FM x-pol is lower 1 dB/m for bending radius larger 33 cm. In general, higher FM loss can be acceptable for strong doped amplifiers. Anyway to compensate for such loss, the pump region has been reduced shrinking air cladding radius to 150 µm. With this expedient, the ratio between doped core and pump region is 0.041, more than double with respect to the scaled commercial design. This is supposed to be beneficial to pump absorption and in general to amplification effectiveness. Another consideration shall be done with respect to the FM behavior in the complete structure. The presence of air cladding as stressed before can increase the interaction between cladding and core mode, this is particularly true in a more open structure. It is possible for particular bending radii to create a coupling between some external modes, which can appear in the space between cladding lattice and air cladding, and FM mode. This coupling effect is in general limited to a small range or bending, and does not affect the FM modal properties outside its range. In the case

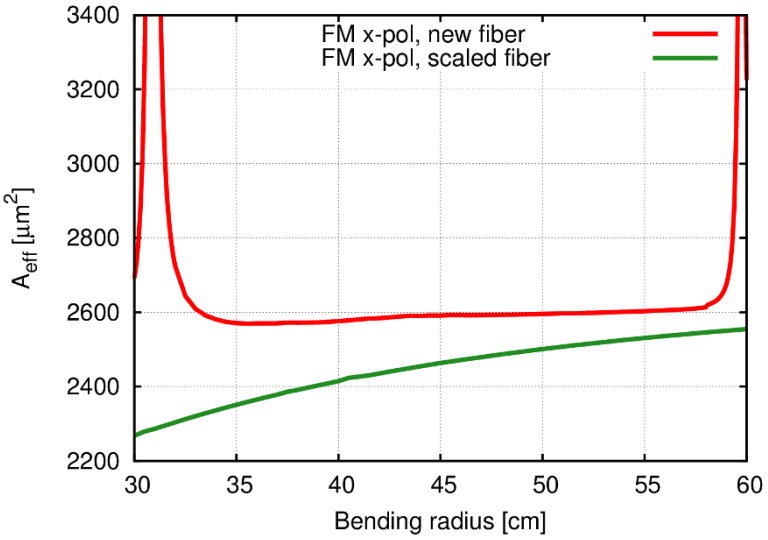

Figure 3.5: FM *x*-pol effective area vs bending radius of both fiber analyzed.

reported, it appears for bending radius intervals around 60 cm and 32 cm. This effect can be counteract acting on the holes diameter to change the interaction between core and cladding, or con be suppressed adding a hole in the position where the side mode is generated.

The principal polarization of new fiber design exhibits a remarkable value of effective area around 2600 μm^2, in the range where no cladding coupling interferes with the FM guidance. This value is larger with respect to value calculated for the scaled fiber as shown in Fig. 3.5.

3.3 Conclusion

In summary, a PM-LMA DC-PCF has been designed to efficiently work in a wavelength regime around 2 µm, by considering the manufacturability. The fiber presents a thulium doped core with a diameter of 80 µm. The PM properties has been achieved including two boron doped SAPs inside the holes lattice. The fiber has been com-

pared with a scaled commercial fiber design. Numerical results display a robust single mode, single polarization operation with a FM mode overlap larger than 0.85, when the bending radius is set in a range between 33 cm to 40 cm. The disadvantaged FM polarization and the HOMs are effectively suppressed. A remarkable value of 2600 μm^2 has been achieved for the advantaged FM polarization effective area.

Chapter 4

Thermal assisted Tm-doped PCF symmetry-free design

In this chapter, the design of a Tm-doped DC-PCF with Symmetry-Free cladding (SF-PCF) with a core diameter of 80 µm is presented, and the fiber guiding properties are thoroughly analyzed by means of a full-vector modal solver based on the finite-element method [95, 96]. The basic idea of this design is focused on breaking the $C_{6\nu}$ symmetry of the fiber cladding to improve delocalization of the most detrimental HOMs, while keeping the Fundamental Mode (FM) confined in the doped core [97, 98]. Moreover, a thermal model is applied to investigate how thermally-induced refractive index change affects the SM properties [99]. The results are compared with those obtained for a Large-Pitch Fiber (LPF) with similar core size, which represents the current state-of-art of large-mode area Tm-doped fibers [91]. The chapter is organized as follows. In the next section, it will be briefly illustrated the main issue of large mode area thulium doped fiber for high power laser operation. The second section will be dedicated to show the characteristics of the SF-PCF and to illustrate the simulation procedure. In the third section, the mode discrimination properties of the fiber will be shown, and the effect of different design parameters and heating conditions will be considered. In the forth section, the focus will be put on the effective area, showing that the SF-PCF is capable of maintaining a very large mode area on

a wide transmission band even at high pump power levels. Conclusion will be drawn in the final section.

4.1 State of art of TDF amplifier

Several applications, including soft-tissue medicine, remote sensing, communication, industrial processing and defense, are currently pushing the research of high power sources in the range between 2 µm and 3 µm, which is also attractive, thanks to of the eye-safe nature of light at these wavelengths [43]. Thulium-doped fiber lasers, with the possibility to obtain emission on a relatively wide band spanning from 1.8 µm to 2.1 µm, are of particular interest for these applications [100]. A huge research effort has been dedicated to the improvement of high power fiber lasers in the last decade, mostly focusing on 1 µm sources, which can exploit the excellent spectroscopic properties of ytterbium ions [101]. In principle, the same fiber design used for Yb-doped fibers can be scaled and applied to the design of Tm-doped fibers [89, 90], with the advantage that operation at longer wavelengths allows SM propagation with larger effective area, therefore pushing the threshold for non-linear phenomena towards higher power levels. Nevertheless, the development of large mode area Tm-doped amplifier with robust single-mode operation is hindered by the much larger quantum defect of thulium ions with respect to ytterbium [102]. That causes remarkable heating of the doped core at relatively low pump power with consequent guidance problem related to the thermal lens effect [86].

4.2 SF-PCF numerical analysis

The schematic of the considered SF-PCF cross-section is reported in Fig. 4.1(a). The inner cladding is obtained from a common triangular lattice where several air-holes have been removed to form two hexagonal layers, rotated with respect to each other. Three more air-holes, marked with arrows in the picture, have been kept to further weaken symmetry of the cross-section, similarly to what was done with the all-solid fiber in [103]. The 19 innermost unit cells are replaced with Tm-doped silica ele-

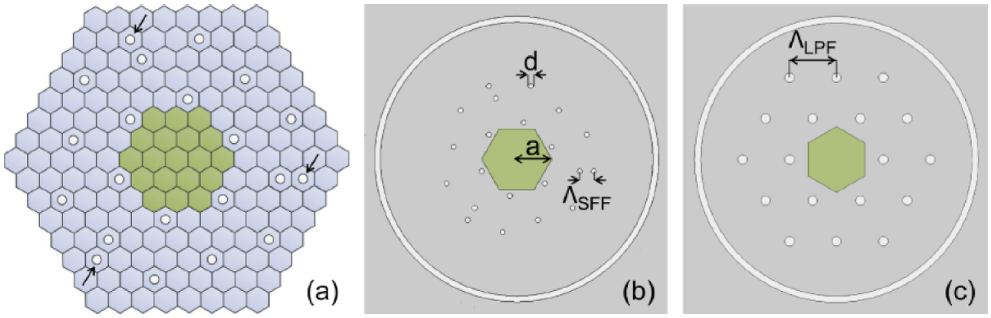

Figure 4.1: (a) Schematic of the cross-section of the symmetry-free PCF. Cross-sections of the simulated (b) symmetry-free and (c) large-pitch fibers.

ments to obtain the active core. The DC SF-PCF considered in the simulations is shown in Fig. 4.1(b), where the key parameters are also indicated. All the considered symmetry-free fibers have a underlying lattice pitch $\Lambda_{SFF} = 14.4\mu m$, which is also the distance between closest air-holes. The fiber core has a corner-to-corner distance d_{cc} of about 80 µm, which would be the distance between corner air-holes if the structure were not rotated with respect to the triangular lattice, and the edge a of resulting doped hexagonal region is 36 µm. A 6 µm thick air-cladding with inner radius of 260 µm surrounds the cross-section, to provide pump guiding. To assess the advantages provided by the SF-PCF over current state-of-art fibers, the simulation results have been compared with those obtained with the LPF shown in Fig. 4.1(c), which is characterized by hole-to-hole spacing $\Lambda_{LPF} = 45\mu m$, core corner-to-corner distance d_{cc} of roughly 81 µm and doped region with edge $a = 31.5\mu m$ [91]. Down-doping of the active region to compensate for the thermally-induced refractive index increase has been taken into account for both fibers.

The degree of confinement of the guided modes has been evaluated considering their overlap integral Γ over the doped area, which has been calculated according to the expression:

$$\Gamma = \iint_S i(x,y)\,dxdy\,, \tag{4.1}$$

where $i(x,y)$ the mode normalized intensity distribution and S the doped core region

[104]. The modal discrimination $\Delta\Gamma$ between the FM and the most confined HOM, which is the difference of their overlap integral values, has been used to assess the SM properties. According to previous works, a $\Delta\Gamma$ value higher than 0.25 can be assumed to be sufficient to provide enough suppression of the HOMs in the gain competition to ensure SM guiding, in this case a safer value of 0.3 has been chosen [64, 103].

Thermal effects have been implemented by calculating the temperature distribution along the fiber cross-section $T = T(x,y)$ with a computationally efficient thermal model, which has been already successfully applied to study the thermo-optic effect in rod-type PCFs with resonant structures [99, 92]. The thermal model assumes that rod fiber is divided in four concentric layers: core, inner cladding, air-cladding, and outer cladding. Each layer, with radius r_i, has its thermal properties characterized by isotropic thermal conductivity k_i. The heat power density Q_0 which has dimension of $\mathrm{W\,m^{-1}}$ is generated in the core. Heat dissipation occurs outside the fiber through convective transfer on fiber edge due to some forced convective system, which can be air or water based, characterized by a convection coefficient h with dimension $\mathrm{W\,m^{-2}\,K^{-1}}$ and a fixed temperature T_a. Under the assumption of negligible longitudinal heat transfer, it is possible to write the steady-state heat equation as a function of the distance r from the center of the structure:

$$\frac{1}{r}\frac{\partial}{\partial r}\left(r\frac{\partial T(r)}{\partial r}\right) = -\frac{Q}{k_i}, \tag{4.2}$$

where the heat power density Q assumes value of Q_0 in the core and 0 elsewhere, T is the temperature . Typical value of silica thermal conductivity k_{Si} is $1.38\,\mathrm{W\,m^{-1}\,K^{-1}}$. This value is used to characterize the core, the inner and the outer cladding regions. The presence of the holes in the inner cladding is negligible [88]. On the other side, the large relative size of air-cladding holes with respect to the silica bridges requires to set an equivalent thermal conductivity k_{eq}, able to describe both contributions to heat transfer. This value can be derived from the thermal resistance approach:

$$k_{eq} = k_{air}\frac{N\cdot b\cdot k_{Si}}{2\pi(r_3 - r_2)}\ln\left(\frac{r_3}{r_2}\right), \tag{4.3}$$

where k_{air} is the thermal conductivity of air with value $0.023\,\mathrm{W\,m^{-1}\,K^{-1}}$, N is he number of silica bridges in the air cladding and b is their width. r_2 and r_3 are the

inner and outer air-cladding radii, respectively. Now the problem is easy to solve by applying continuity condition at the inner interfaces and convective heat flow at the outer boundary which is described by this law:

$$\frac{\partial T(r=R)}{\partial r} = \frac{h}{k_{Si}}(T_a - T(r=R)), \tag{4.4}$$

where R is the outer cladding radius or the rod fiber. The consequent refractive index change in silica and doped silica $\Delta n_t h$ can be obtained by applying thermo-optic relation $\Delta n_{th} = \beta \cdot (T - T_0)$, being β equal to $1.16 \times 10^{-5}\,\mathrm{K}^{-1}$ the thermo-optic coefficient for silica and T_0 equal to 25 °C.

Both the SF-PCF and the LPF have been assumed to be 1 m long rod-type fibers, with outer diameter of 1.7 mm. Convection cooling with forced water flow at the temperature of 14 °C and convective transfer coefficient h equal to $2000\,\mathrm{W\,m^{-2}\,K^{-1}}$ has been applied as boundary condition at the outer fiber edge. Temperature gradient on the fiber cross-section is generated by quantum defect heating of the active core, which is responsible of a heat load q':

$$q' = \frac{1 - 10^{-\alpha \frac{dL}{10}}}{dL} \cdot \left(1 - \frac{\lambda_p}{\lambda_s}\right) \cdot P, \tag{4.5}$$

where α, equal to 9 dB/m, is the pump absorption, $\lambda_p = 793$ nm the pump wavelength, λ_s the emission wavelength, dL the fiber length where the average optical to heat energy conversion is calculated and P the pump power [92]. Heat load is related to heat density Q_0 by the relation $q' = Q_0 \cdot A_{core}$, being A_{core} the doped core area. q' values between $0\,\mathrm{W\,m^{-1}}$ and $340\,\mathrm{W\,m^{-1}}$ have been considered for the simulations, which correspond to the average heat load obtained from (4.5) in the last 10 cm of the fiber closer to the pumping end, for a coupled pump power P between 0 and 300 W.

4.3 Single mode regime

In order to optimize the SF-PCF design to provide the best SM properties in different operating scenarios, the $\Delta\Gamma$ value has been calculated for different choice of the air holes diameter d between $0.18 \cdot \Lambda_{SFF}$ and $0.30 \cdot \Lambda_{SFF}$, taking into account heat load

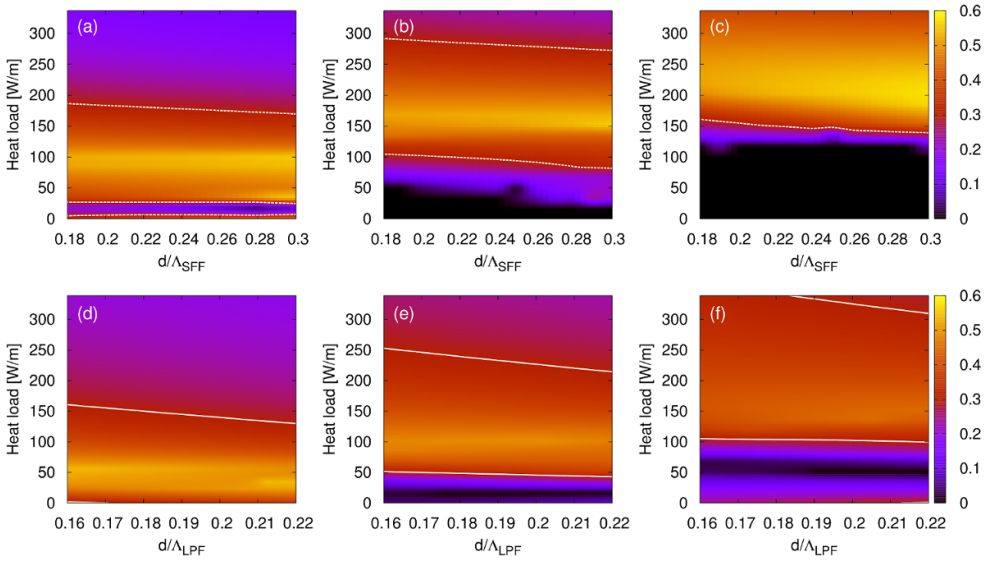

Figure 4.2: (a) Overlap integral difference $\Delta\Gamma$ between the FM and the most detrimental HOM of the SF-PCF, as a function of the normalized air-hole diameter and heat load, obtained with (a) no core down-doping, (b) with core down-doping $\Delta n = -10^{-4}$, and (c) with $\Delta n = -2 \times 10^{-4}$. Same results obtained for large-pitch fibers are reported in (d) for no core down-doping, (e) for $\Delta n = -10^{-4}$ and (f) for $\Delta n = -2 \times 10^{-4}$. White lines are drawn at $\Delta\Gamma$ = 0.3.

values spanning from $0\,\mathrm{W\,m^{-1}}$ to $340\,\mathrm{W\,m^{-1}}$. The value of operating wavelength λ has been considered equal to $2\,\mu\mathrm{m}$ and 80 modes have been calculated for each parameter combination to find the most confined ones. The simulation results are shown in Fig. 4.2(a)-(c), for a core down-doping $\Delta n = 0$, -1×10^{-4} and -2×10^{-4}, respectively. The same procedure has been applied to the large-pitch fiber for d/Λ_{LPF} values between 0.16 and 0.22, and the results are shown in Fig. 4.2(d)-(f).

Clearly, none of the considered designs of the SF-PCF or LPF is able to provide SM guidance over the full range of considered heat load values. All fibers show a similar temperature dependent behavior, which is more evident in down-doped fibers. At low heat load values, for example approximately below 80-100 $\mathrm{W\,m^{-1}}$ for the

SF-PCFs with $\Delta n = -1 \times 10^{-4}$ of Fig. 4.2(b), the confinement of the FM is poor and its overlap integral is close the one of the HOMs, which is below 0.4 in most cases. In some extreme conditions, corresponding to the black areas of Fig. 4.2(b) and Fig. 4.2(c), the overlap integral of the most confined HOM is even higher than the one of the FM. All the modes propagate mostly outside from the doped core, and poor amplification efficiency is expected. As the heat load increases the FM becomes significantly better confined than the HOMs, and the modal discrimination increases up to the maximum value, which is found at about $150\,\mathrm{W\,m^{-1}}$ for the SF-PCFs with $\Delta n = -1 \times 10^{-4}$. After that point, any further increase of the core temperature decreases the modal discrimination by providing better confinement to the HOMs, up to the point where $\Delta\Gamma$ is again below 0.3 and the fiber operates in multimode regime.

By comparing Fig. 4.2(a)-(c) it is possible to notice that SM operation can be shifted to significantly higher power levels by acting on core refractive index. Indeed, the SF-PCF without core down-doping can provide SM propagation for heat load between about $25\,\mathrm{W\,m^{-1}}$ and $180\,\mathrm{W\,m^{-1}}$, while with $\Delta n = -1 \times 10\ -4$ the SM regime is found between $90\,\mathrm{W\,m^{-1}}$ and $290\,\mathrm{W\,m^{-1}}$ and from $150\,\mathrm{W\,m^{-1}}$ up to more than $350\,\mathrm{W\,m^{-1}}$ for $\Delta n = -2 \times 10^{-4}$. This means that a SF-PCF with suitable core down-doping is capable to maintain SM propagation even with a coupled pump power larger than 300 W. On the other side, the use of a too depressed core is detrimental for the operation at low pump power, and therefore core refractive index must be chosen according to the application. It is worth noting that in a real world scenario the heat load is not uniform along the fiber, being significantly lower far away from the pumping end, that is at the seed side assuming a counter-propagating pumping scheme. As a consequence, the FM is less confined and its overlap with the doped area is lower, resulting in a decrease of the amplifier efficiency. Considering the results of Fig. 4.2, it is thereby preferable to choose a fiber design that allows operation close to the upper edge of the SM region at the pumping end, so that FM confinement and SM regime are preserved throughout most of the fiber length.

Air-hole size has a weaker impact on the guiding properties of the SF-PCF with respect to down-doping, resulting in a small shift of the SM region towards lower heat load values for increasing d/Λ_{SFF} , that can be explained with the increased index

contrast of the fibers with largest air-holes.

The main advantage of the SF-PCF approach is the possibility to provide very high modal discrimination at high pump power levels. The maximum value of $\Delta\Lambda$ achieved is above 0.54 for all the three considered values of core down-doping, and it is found at a heat load of about $100\,\mathrm{W\,m^{-1}}$, $150\,\mathrm{W\,m^{-1}}$ and $200\,\mathrm{W\,m^{-1}}$ for the fibers having $\Delta n = 0$, -1×10^{-4} and -2×10^{-4} , respectively. Remarkably, similar mode discrimination has been reported for the all-solid version of the symmetry-free fiber without considering thermal effects [103], and is among the highest values reported so far for any index-guiding LMA fiber design. By choosing a suitable level of core down-doping it is possible to obtain SM guiding at high heat load also with the LPF, but the index depression is detrimental to the modal discrimination, as can be inferred by the comparison of Fig. 4.2(d) and Fig. 4.2(f). Indeed, with the LPF without core down-doping it is possible to reach a $\Delta\Gamma$ value larger than 0.5 at about $50\,\mathrm{W\,m^{-1}}$, while a maximum overlap difference of only 0.42 is obtained with a core down-doping of -2×10^{-4}.

To give a deeper insight on the effect of fiber heating on mode confinement, Fig. 4.3(a) reports the overlap integral of the four most relevant modes of the SF-PCF, calculated at λ equal to 2 µm for the fiber with $d/\Lambda_{SFF} = 0.24$ and $\Delta n = -2\times10^{-4}$, as a function of the heat load. Notice that when the fiber is relatively cold both the fundamental LP_{01}-like mode, whose field intensity distribution is shown in Fig. 4.3(b), and the LP_{11}-like one, shown in Fig. 4.3(c), are poorly confined, with Γ values below 0.2. Under this heating conditions the mode with the highest overlap is the LP_{03}-like, shown in Fig. 4.3(e), whose overlap integral may even exceed 0.5. This behavior is due to core down-doping, which causes the modes that are naturally localized in the core to be poorly guided due to the lower refractive index of the doped region with respect to the cladding. The increase of the heat load compensates the core down-doping, improving the confinement of the LP_{01}-like mode while decreasing the overlap integral of the LP_{03}-like one. The FM has the highest overlap integral for q higher than $120\,\mathrm{W\,m^{-1}}$ and its value rapidly increases with the heat load. Between q' equal to $145\,\mathrm{W\,m^{-1}}$ and q' equal to $200\,\mathrm{W\,m^{-1}}$ the role of the most detrimental HOM is played by the LP_{02}-like, shown in Fig. 4.3(d), whose Γ value is anyway below

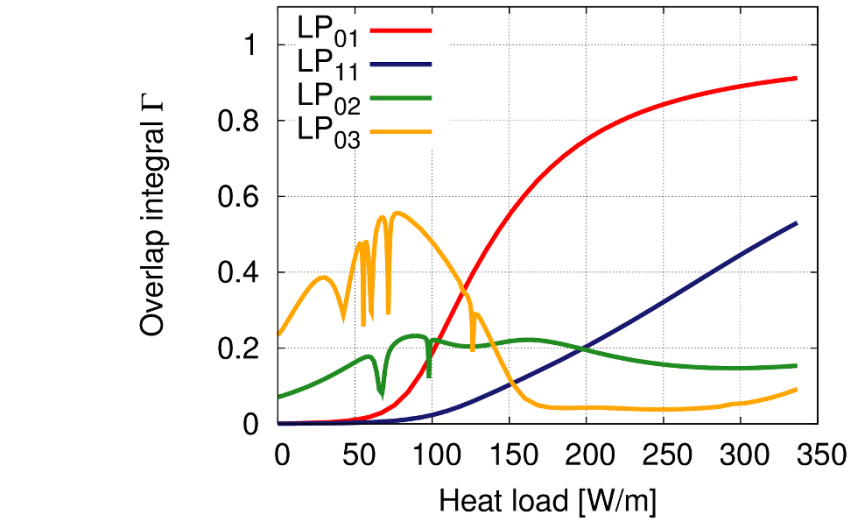

(a)

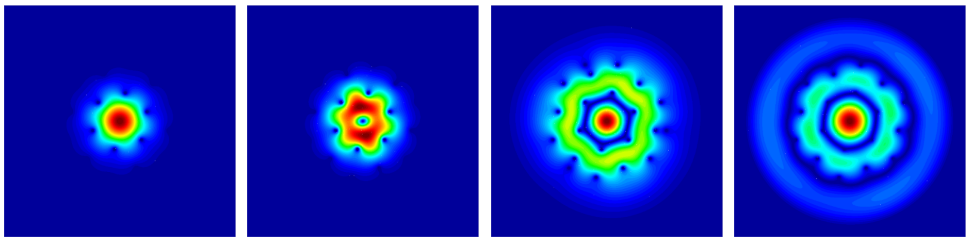

(b) (c) (d) (e)

Figure 4.3: Overlap integral of the most relevant guided modes of the SF-PCF as a function of the heat load, calculated at λ equal to 2 µm. Magnetic field modulus distribution of the (b) LP_{01}-like, (c) LP_{11}-like, (d) LP_{02}-like and (e) LP_{03}-like modes of the SF-PCF.

0.25. As a consequence, for q' greater than 150 W m^{-1} the SF-PCF is SM. Finally, at very high power levels the thermally-induced refractive index gradient is so strong to force the fiber to behave effectively as graded-index C_{6v}-symmetric waveguide. For q' greater than 200 W m^{-1} the LP_{11}-like HOM becomes the most detrimental one, its

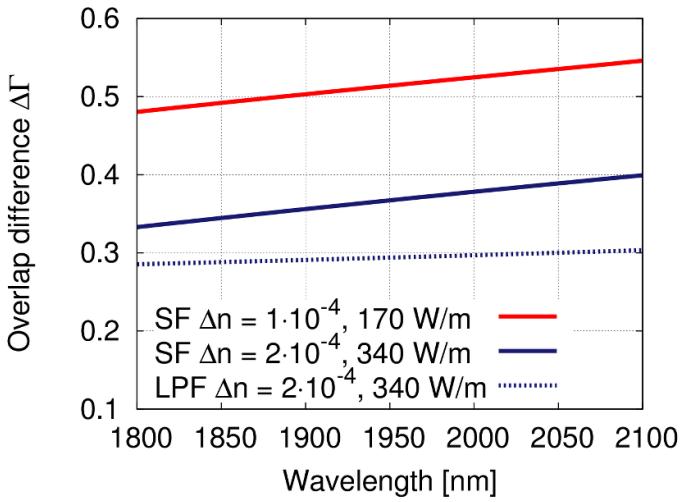

Figure 4.4: $\Delta\Gamma$ between the LP_{01}-like and the LP_{11}-like modes of the SF-PCF (solid lines) and of the LPF (dashed lines).

overlap integral increasing almost linearly with the heat load beyond this heat load value. Finally, it is worth noting that this SF-PCF is not only capable of providing strong delocalization of the HOMs even at high thermal load, but also to guarantee tight FM confinement, with overlap higher than 0.9 at q' larger than 225 $\mathrm{W\,m^{-1}}$.

In order to demonstrate that the good HOM suppression properties of the SF-PCF are maintained over the whole spectrum of interest for Tm emission, the modal discrimination between the FM and the LP_{11}-like HOM has been calculated between 1800 nm and 2100 nm in two representative cases, and compared with the results provided by a LPF, as depicted in Fig. 4.4. Simulations have been performed on a SF-PCF with d/Λ_{SFF} equal to 0.24 and core down-doping Δn equal to -1×10^{-4} and q' with value of 170 $\mathrm{W\,m^{-1}}$, which roughly corresponds to the condition where the maximum $\Delta\Gamma$ is observed at λ equal to 2 µm, and on a SF-PCF with the same pitch but $\Delta n=-2\times10^{-4}$ at q' equal to 340 $\mathrm{W\,m^{-1}}$, which is the maximum value of the heat load taken into account. The results have been compared with those obtained for a LPF with $d/\Lambda_{LPF}=0.20$ with $\Delta n=-2\times10^{4}$, operating with q' equal to 340 $\mathrm{W\,m^{-1}}$.

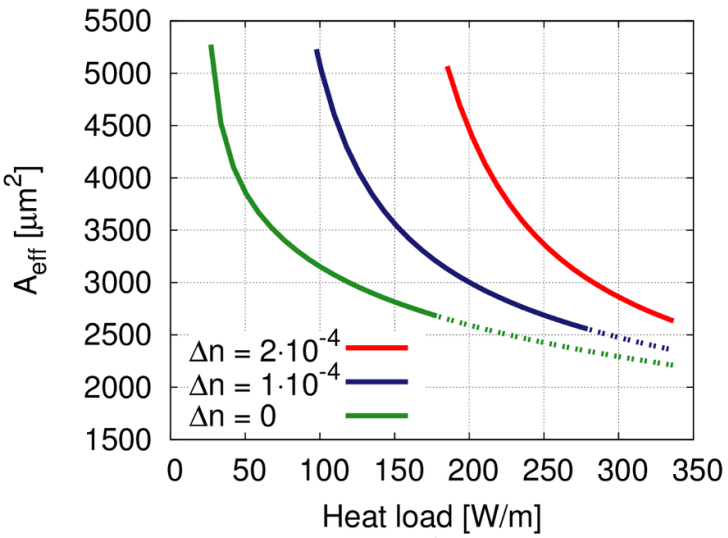

Figure 4.5: Effective area of the SF-PCF with $d/\Lambda_{SFF} = 0.24$ and different values of core down-doping, calculated at $\lambda = 2\mu m$ as a function of the heat load. Dashed lines are used where fibers operate in multi-mode regime.

The overlap difference for both SF-PCF slightly increases with the wavelength, with a variation of about 0.08 over the considered range. The SF-PCF operating at q' equal to 170 W m^{-1} shows a remarkable overlap difference close to 0.5 over the whole band, with maximum value of 0.54 at 2100 nm. Despite a lower $\Delta\Gamma$, also the SF-PCF operating at q' equal to 340 W m^{-1} is SM over the whole range, reaching Δn values between 0.33 and 0.4. These performances are better than those obtained by the LPF for the same heat load, being its overlap difference close to the threshold for SM operation at $\Delta\Gamma = 0.3$ throughout the considered wavelength span.

4.4 Effective area

Figure 4.5 shows the effective area calculated at λ equal to 2 µm for the LP_{01}-like mode of the SF-PCFs with the three considered values of core down-doping and

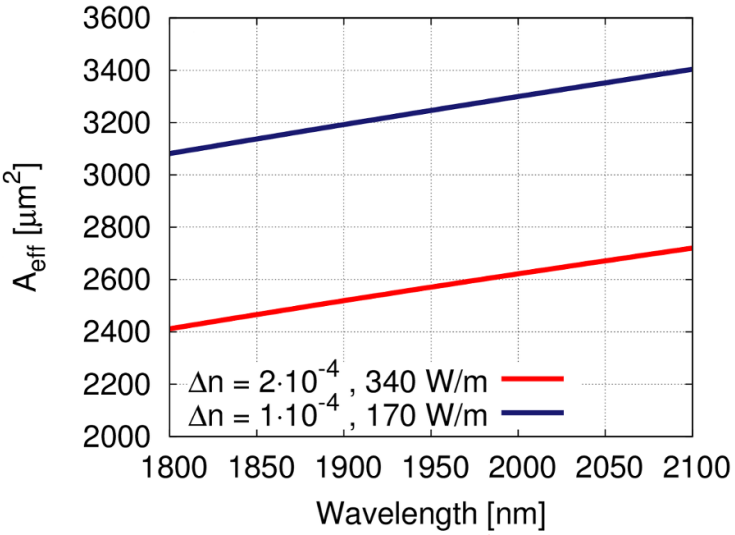

Figure 4.6: Effective area of the SF-PCF with $d/\Lambda_{SFF} = 0.24$ and $\Delta n = -2 \times 10^{-4}$ for a heat load of $340\,\mathrm{W\,m^{-1}}$ (red line) and of the SF-PCF with $d/\Lambda_{SFF} = 0.24$ and $\Delta n = -1 \times 10^{-4}$ for a heat load of $170\,\mathrm{W\,m^{-1}}$ (blue line).

$d/\Lambda_{SFF} = 0.24$, as a function of the heat load. The curves have been drawn only for values of q' that ensure an overlap larger than 0.7, since lower values of Γ are not suitable for amplification, and are dashed where the fibers operate in multi-mode regime. The intense heating of the fiber has a remarkable effect on A_{eff} , roughly halving its value from about $5000\,\mu\mathrm{m}^2$ to about $2600\,\mu\mathrm{m}^2$ at the maximum heat load allowed for SM operation. Notice that down-doping does not affect these limits, but only determines the heat load at which these values of A_{eff} are obtained. For example, an effective area of $3000\,\mu\mathrm{m}^2$ is reached by the fiber without core down-doping at q' equal to $120\,\mathrm{W\,m^{-1}}$, at q' equal to $200\,\mathrm{W\,m^{-1}}$ by the fiber with $\Delta n = -1 \times 10^{-4}$ and at q' equal to $280\,\mathrm{W\,m^{-1}}$ by the fiber with $\Delta n = -2 \times 10^{-4}$. Notice also that the effective area shrinking due to heating is comparable to the values that have been found experimentally for the Tm-doped fiber laser based on the LPF with similar core diameter [91].

The effective area as a function of the wavelength of the two SF-PCFs already considered in Fig. 4.4, with the same heat load conditions previously used, is reported in Fig. 4.6. In both cases, the effective area change with the wavelength has a similar slope, with an increase over the considered wavelength range of about $350\,\mu m^2$. When the maximum mode discrimination is achieved, that is by the fiber with $\Delta n = -1 \times 10^{-4}$ at q' equal to $170\,W\,m^{-1}$, A_{eff} is between $3100\,\mu m^2$ at λ equal to 1800 nm and $3400\,\mu m^2$ at λ equal to 2100 nm. On the other hand, by considering the fiber with $\Delta n = -2 \times 10^{-4}$ at q' equal to $340\,W\,m^{-1}$, an effective area between $2400\,\mu m^2$ at λ equal to 1800 nm and $2700\,\mu m^2$ at λ equal to 2100 nm is found.

4.5 Conclusion

In this chapter, the design of a double-cladding photonic crystal fiber with 80 µm-core and reduced cladding symmetry has been investigated, aiming to obtain robust SM guiding even at high heat load values, such as those generated during operation of high-power Tm-doped fiber lasers. A full-vector modal solver based on the finite-element method with integrated thermal model to calculate temperature-induced refractive index change has been applied to analyze the effects of the main fiber design parameters on the modal discrimination for different heating conditions. The results have shown that the SF-PCF is capable of providing efficient suppression of the HOMs, with maximum overlap difference between the FM and the most detrimental HOM larger than 0.5, even when relevant heat load is assumed. This modal discrimination is among the highest reported so far for index guiding PCFs, being surpassed only on narrow transmission bands by PCF exploiting resonant features [105]. Moreover, SM propagation with A_{eff} larger than $2500\,\mu m^2$ has been demonstrated at heat load of $340\,W\,m^{-1}$.

Chapter 5

Improvement of mode area in Tm-doped SF-PCF

In this chapter, is presented an improved design, with respect to the one in the previous chapter, of a rod-type Tm-doped PCF with reduced cladding symmetry. This new design shows the possibility to scale its core diameter up to more than 120 µm while maintaining single mode operation. The new fiber can work well under severe heat load. Modal properties have been analyzed by means of a full-vector modal solver based on the finite-element method, with an embedded thermal model to account for thermally-induced refractive index change. Simulation results show that this new proposed design is able to achieve SM propagation with effective area larger than $5000\,\mu m^2$ under a heat load of $250\,W\,m^{-1}$ and about $3800\,\mu m^2$ for a heat load of $300\,W\,m^{-1}$, after a proper optimization of the design parameters.

The chapter is organized as follow. The next section will introduce the Tm-doped PCF with reduced cladding symmetry and describe the simulation procedure. In the second section, the modal properties of the proposed fiber will be discussed, and the effects of the change of the cross-section parameters on the HOM suppression capabilities will be evaluated for a wide range of heating conditions. In the the third section, it will be shown that it is possible to significantly increase the core size obtaining remarkable values of modal effective area. The forth section will be dedicated

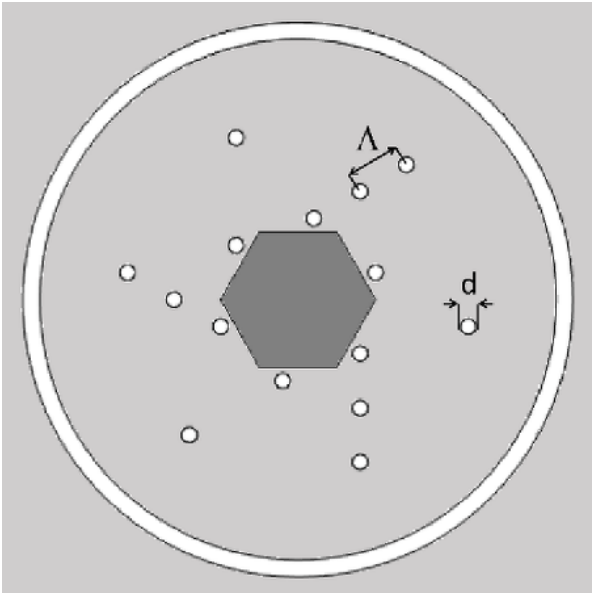

Figure 5.1: Cross-section of the SF-PCF under investigation. Symmetry breaking is obtained with the rotation of the first rings of holes, and with the insert of three spiral arranged branches of holes. The stack and draw scheme is maintained.

on the analysis of beam quality through the investigation of M^2 parameter, a further consideration on the possibility to extend the results obtained on a wide range of operation wavelength will be discussed. The final Section will draw the conclusion.

5.1 Modeling of DC-PCF with low cladding symmetry

The schematic of the cross-section of the considered Symmetry-Free PCF (SF-PCF) is shown in Fig.5.1. The fiber is based on a triangular lattice of air-holes, which has been deeply modified to remove any mirror symmetry. The 19 innermost cells form the Tm-doped core, which has a hexagonal shape. Only six air-holes have been kept in the first cladding ring, and they have been chosen not to be aligned with the corners of the doped hexagonal area. Three arms, made each of three air holes, extend into

the cladding providing a clockwise *spin* to the cross-section. Three further air-holes are added in order to avoid excessive leakage of the fundamental mode (FM). The whole structure is surrounded by an 8 µm air-cladding, to provide pump confinement. The particular design of the inner cladding has been chosen according to a number of observations. The first one is that the modes are naturally influenced by the structural symmetry of the fiber [106]. Therefore, the removal of any mirror symmetry can be beneficial to suppress the high order modes with a mirror-symmetric distribution, such as the LP_{11} and the LP_{31} , which are usually the most detrimental in LMA DC-PCFs [103, 107]. Furthermore, severe thermal lensing is expected to arise during laser operation due to the large quantum defect of Thulium, which will increase core *NA* and provide stronger confinement to all the modes. As a consequence, a very open cladding structure was used, with few air-holes and very large silica regions to favor leakage of the high-order modes and their consequent delocalization. Finally, the proposed design is built over an underlying triangular lattice, which provides several practical advantages in the manufacturing of the fiber with respect to other non-symmetric designs, such as the pentagonal fiber proposed in [98].

The main fiber design parameters that it will be considered in the proceeding of the analysis are the underlying PCF lattice hole-to-hole spacing Λ, which is the minimum distance between cladding air-holes, the normalized air-hole diameter d/Λ and the doped-core refractive index. The SF-PCF is assumed to be a rod-type fiber, with an outer diameter of 1.7 mm.

The guided modes of the SF-PCF have been calculated by means of a full-vector modal solver based on the finite-element method [95, 108], considering operation at the wavelength λ equal to 2000 nm. In order to assess the confinement of each mode the overlap integral Γ on the doped core has been considered, which has been calculated as the integral of magnetic field intensity over the doped area, normalized to the total intensity. The formal definition has been given in Eq. (4.1). The SM properties of the SF-PCF have been evaluated by considering the modal discrimination $\Delta\Gamma$ [109], which is defined as the difference between the overlap integral values of the FM and the one of the most confined HOM. According to previous publications, effective SM propagation in the gain competition is assumed to occur with $\Delta\Gamma$ be-

tween the LP_{01}-like mode and the most detrimental HOM larger than 0.3 [64, 103]. In order to include the effects of thermally induced refractive index change along the fiber cross-section, a computationally efficient thermal model has been applied [99]. The model assumes that a heat load q' per unit length is generated in the fiber core as a consequence of the amplification process, which is related to the pump and signal wavelengths λ_p and λ_s , pump absorption α and pump power P by Eq. (4.5). The fiber is assumed to be convection cooled at the outer boundary assuming convective transfer coefficient h equal to 2000 $\mathrm{W\,m^{-2}\,K^{-1}}$, which is appropriate for forced water flow, at the temperature of 14 °C. The heating and cooling process leads to a temperature gradient across the fiber, with a parabolic shape in the core and a logarithmic decay in the cladding. Thermo-optic effect causes a temperature related increase of the refractive index of silica and doped silica, which is $\Delta n_{th} = \beta \cdot (T - T_0)$, with β equal to $1.16 \times 10^{-5}\,\mathrm{K^{-1}}$ and T_0 fixed to the standard environment temperature of 25 °C [86, 110]. In the FEM simulations, the refractive index on each mesh triangle has been updated according to the thermally induced refractive index change for any considered generated heat value. q' values between 0 and 340 $\mathrm{W\,m^{-1}}$ have been used in the simulations, which correspond to the average heat load in the last 10 cm of the fiber closer to the pumping end, for a coupled pump power P between 0 and 300 W, assuming typical pump absorption $alpha$ equal to 9 dB/m. Pump wavelength is assumed to be 793 µm, which is the typical absorption line of thulium ions easily achievable by high brightness commercially available laser diode.

5.2 Higher order modes suppression

Prior to any optimization of the SF-PCF fiber it is important to provide a clear picture of the most relevant guided modes and of the effects of thermal load on the guiding properties. Fig. 5.2(a) and (b) shows the calculated overlap integral as a function of the heat load of the most relevant modes of two SF-PCFs with λ equal to 14.4 µm, $d/\Lambda = 0.4$ and air-cladding diameter 240 µm, the first one without considering core down-doping and the second with core down-doping Δn equal to -2×10^{-4} . Because of the presence of the air-cladding and due to the very few air holes in the inner

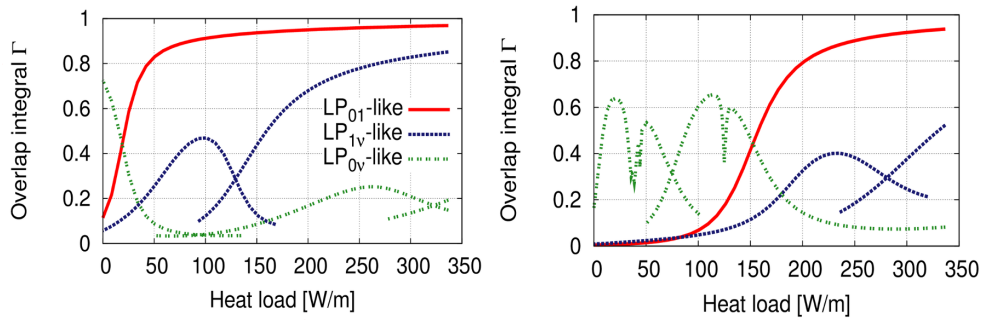

Figure 5.2: Overlap integral of the most relevant modes of the SF-PCF, calculated as a function of the heat load q' for a fiber (a) without core down-doping and (b) with core down-doping Δn equal to -2×10^{-4} .

cladding, it is not always possible to clearly separate core guided and cladding modes. Typically, guided modes are well confined in the fiber core at high heat load, and have a clean $LP_{\nu\mu}$-like field distribution. As the core temperature decreases, they are gradually pushed outside from the core, into the large silica regions of the cladding. At the same time, modes with a similar field distribution in the core and several peaks in the cladding become more and more confined, eventually reaching Γ larger than 0.6 in some cases. These modes are the result of the coupling between the $LP_{\nu\mu}$-like modes and several cladding modes. As a consequence of this behavior, all the modes originating from the fundamental LP_{01}-like mode shall be grouped into $LP_{01,x}$-like family, being x an index identifying the cladding mode involved, while all those descending from the coupling of the LP_{11}-like HOM shall be grouped into $LP_{11,x}$-like ones. In Fig. 5.2(a) and (b) overlap integrals are shown using this norm.

As an example, the LP_{11}-like mode is well confined for q' equal to $350\,\mathrm{W\,m^{-1}}$ in the SF-PCF with no down-doping, as shown by the field distribution in Fig. 5.3(a), with an overlap larger than 0.8. Decreasing the temperature favors its leakage, and the mode becomes almost completely spread outside from the core when q' equal to $100\,\mathrm{W\,m^{-1}}$, as shown in Fig. 5.3(b). At this heat load value the HOM with the

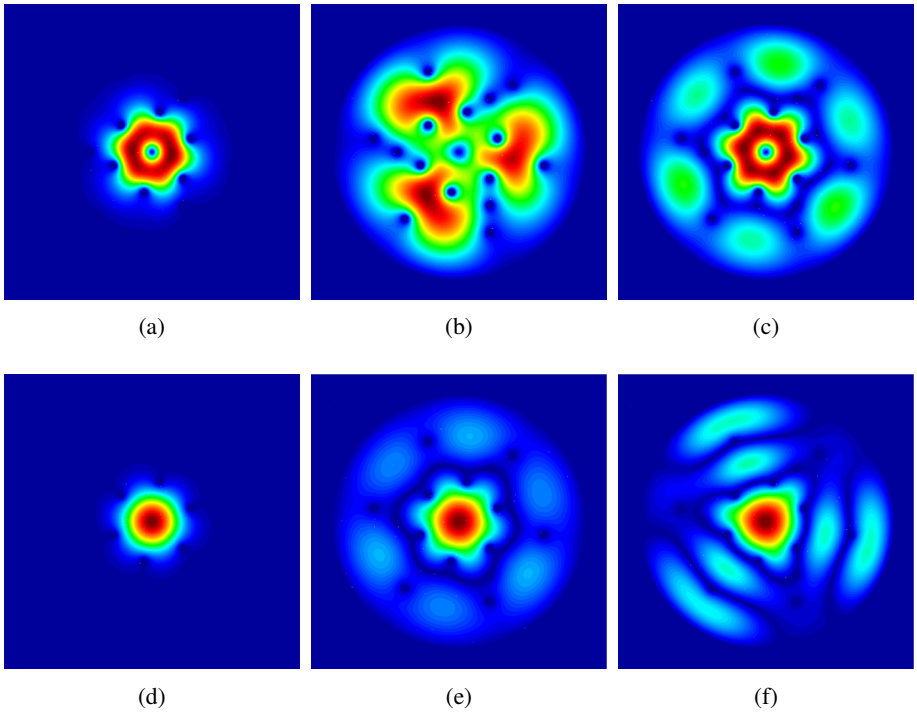

Figure 5.3: Magnetic field modulus distribution of (a) the LP_{11}-like mode at q' equal to $350\,W\,m^{-1}$, (b) the LP_{11}-like mode at q' equal to $100\,W\,m^{-1}$, (c) of the $LP_{11,1}$-like mode at q' equal to $100\,W\,m^{-1}$, obtained with $\Delta n = 0$. Magnetic field modulus distribution of (d) the LP_{01}-like mode at q' equal to $350\,W\,m^{-1}$, (e) the $LP_{01,1}$-like mode at q' equal to $120\,W\,m^{-1}$, (f) of the $LP_{01,2}$-like mode at q' equal to $50\,W\,m^{-1}$, obtained with $\Delta n = -2 \times 10^4$.

highest Γ is the $LP_{11,1}$-like of Fig. 5.3(c), which is the result of the coupling between the LP_{11}-like mode and a mode located in the silica cladding. Similar behavior is observed also for the FM, especially in the down-doped PCF. The field intensity distribution of the uncoupled LP_{01}-like mode at q' equal to $350\,W\,m^{-1}$, of the $LP_{01,1}$-like at q' equal to $120\,W\,m^{-1}$ and of the $LP_{01,2}$-like at q' equal to $50\,W\,m^{-1}$ are shown in Fig. 5.3(d)-(e), respectively. Such interaction, known as avoided crossing, between

core and cladding modes is not uncommon in double-cladding PCFs, and has been already reported in several publications [61, 111]. Notice that the presence of secondary intensity peaks in the cladding causes a significant degradation of the beam quality and of the amplification efficiency, and therefore the fiber should operate at power levels high enough not to allow coupling of the FM with any cladding mode. In order to easily identify this regime, the clean LP_{01}-like mode, which is not coupled to any cladding mode, was not grouped with the other $LP_{01,x}$-like in Fig. 5.2(a) and (b). As shown in Fig. 5.2(a), under a heat load lower than about $350\,W\,m^{-1}$ the LP_{01}-like mode is poorly confined even in the SF-PCF without core down-doping, having Γ values lower than 0.6, which are not suitable for efficient amplification. Increasing the thermal load causes a steep raise of the FM overlap, which quickly exceeds 0.9. On the contrary, it requires an heat load higher than $175\,W\,m^{-1}$ to the most detrimental HOM to reach $\Gamma = 0.6$, therefore providing $\Delta\Gamma > 0.3$ and enabling SM operation for q' between about $40\,W\,m^{-1}$ and $190\,W\,m^{-1}$. Further increase of the pump power leads to an insufficient modal discrimination to allow effective suppression of the HOM. One possible solution to obtain SM regime under heavier heat load is to apply core down-doping. As shown in Fig. 5.2(b), with Δn equal to -2×10^{-4} it is possible to maintain a mode discrimination higher than 0.3 even with q' up to the maximum considered value, but this choice does not allow amplification at low power levels, being the overlap of the LP_{01}-like mode lower than 0.6 for any q' lower than $170\,W\,m^{-1}$.

In order to optimize the design parameters, the modal discrimination $\Delta\Gamma$ between the FM and the most detrimental HOM has been calculated for different combinations of d/Λ and core refractive index, taking into account a heat load $0\,W\,m^{-1}$ to $340\,W\,m^{-1}$. The FEM-based solver was set to calculate 100 solutions for each simulation, and the two modes with the highest overlap have always been found to belong to the $LP_{01,x}$-like and $LP_{11,x}$-like groups. The obtained $\Delta\Gamma$ values are shown in Fig. 5.4(a)-(c) for core down-doping Δn equal to 0, -1×10^{-4} and -2×10^{-4}, respectively. White lines are drawn to highlight the edges of the SM region, corresponding to $\Delta\Gamma = 0.3$. Regardless of the choice of the air-hole size, all the PCFs provide modal discrimination larger than 0.3 over a wide range of values of q'. The minimum

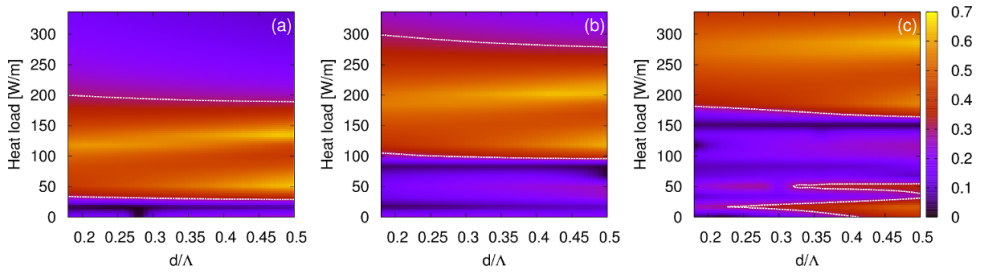

Figure 5.4: Modal discrimination $\Delta\Gamma$ between the FM and the most detrimental HOM as a function of the air-hole diameter and heat load, for a SF-PCF with hole-to-hole spacing 14.4 µm and (a) no core down-doping, (b) Δn equal to -1×10^{-4} and (c) Δn equal to -2×10^{-4} . White lines are drawn at $\Delta\Gamma = 0.3$.

heat load required for SM propagation increases with the amount of down-doping, being about 70 W m^{-1} for $\Delta n = 0$, 100 W m^{-1} for $\Delta n = -1\times10^{-4}$ and 175 W m^{-1} at $\Delta n = -2\times10^{-4}$. Also the upper heat load limit for SM propagation is increased by a deeper down-doping, so that the net effect of core down-doping is to push the SM regime towards higher heat load. Notice that $\Delta\Gamma$ higher than 0.3 is found also at very low q' for the fiber with the strongest core down doping, but in this case the FM field distribution presents several peaks in the cladding due to coupling with cladding modes, as shown in Fig. 5.3(d)-(f), and therefore this regime is not suitable for operation. Modal discrimination higher than 0.4 is obtained over most of the SM windows. The maximum value of $\Delta\Gamma$ is about 0.64, significantly improving the results obtained by the SF-PCF presented in the previous chapter, and it is found at q' about 140, 200, and 280 W m^{-1}, for Δn equal to 0, Δn equal to -1×10^{-4} and Δn equal to -2×10^{-4} respectively. Increasing the air hole diameter can provide slightly better overall HOM suppression, as can be inferred by the brighter colors closer to the right edges of Fig. 5.4(a)-(c), but it would also cause deformation of the FM field distribution due to the larger air-holes surrounding the core. As a consequence, an intermediate value $d/\Lambda = 0.4$ has been be considered.

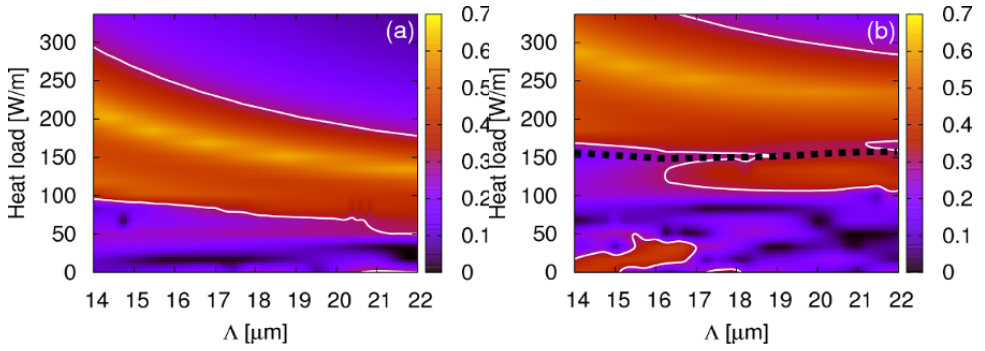

(a) (b)

Figure 5.5: Mode discrimination $\Delta\Gamma$ between the FM and the most detrimental HOM as a function of the hole-to-hole spacing Λ and heat load, for a SF-PCF with $d/\Lambda = 0.4$ and (a) $\Delta n = -1 \times 10^4$ and (b) $\Delta n = -2 \times 10^4$.

5.3 Mode area scaling

In order to evaluate the possibility to scale the effective area of the SF-PCF without jeopardizing the effective SM behavior, the modal discrimination has been calculated again as a function of the hole-to-hole spacing Λ and the heat load q', assuming a constant ratio between the core and the air-cladding diameters and fixed $d/\Lambda = 0.4$. The simulation results are shown in Fig. 5.5(a) and (b) for $\Delta n = -1 \times 10^4$ and $\Delta n = -2 \times 10^4$, respectively. In general, smaller Λ allows SM guiding for a wider range of q', while for increasing values of the pitch the maximum heat load at which HOM suppression is still possible decreases significantly, regardless of the core down-doping level, due to the tighter confinement of the HOMs. For what concerns the SF-PCF with $\Delta n = -1 \times 10^4$, $\Delta\Gamma \geq 0.3$ between q' equal to $100\,\mathrm{W\,m^{-1}}$ and q' equal to $300\,\mathrm{W\,m^{-1}}$, with Λ equal to $14\,\mu\mathrm{m}$ and between q' equal to $50\,\mathrm{W\,m^{-1}}$ and q' equal to $170\,\mathrm{W\,m^{-1}}$, with Λ equal to $22\,\mu\mathrm{m}$. With this large hole-to-hole spacing it is still possible to reach very high values of modal discrimination, up to about 0.6 for a generated heat of $150\,\mathrm{W\,m^{-1}}$. By applying a stronger down-doping further increase of the power limit for effective SM propagation can be achieved, even when very

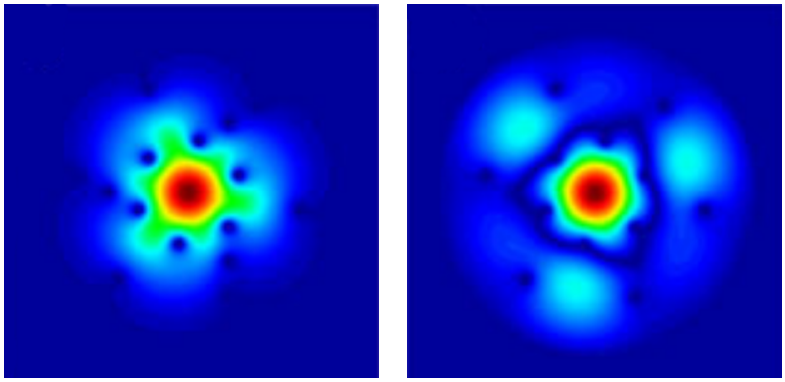

(a) (b)

Figure 5.6: Magnetic field modulus distribution, calculated for the SF-PCF with Λ equal to 17 µm and $\Delta n = -2 \times 10^4$, of the (c) LP_{01}-like mode at q' equal to 170 W m^{-1} and (d) $LP_{01,1}$-like mode at q' equal to 130 W m^{-1} .

large pitch is considered. As shown in Fig. 5.5(b), with a Δn value of -2×10^{-4} it is possible to obtain $\Delta\Gamma$ larger than 0.3 for generated heat up to 270 W m^{-1} and Λ equal to 22 µm, which corresponds to a core diameter of about 120 µm. Notice that in the SF-PCF with Δn equal to -2×10^{-4} the FM can maintain an high overlap integral even when the LP_{01}-like mode is strongly coupled with cladding modes, as already shown in Fig. 5.2(b). A dashed black line in Fig. 5.5(b) shows the minimum heat load required to ensure that the most confined $LP_{01,x}$-like mode is the LP_{01}-like , with no secondary peaks in the cladding.

The magnetic field modulus distribution of the LP_{01}-like mode calculated just above this line is shown in Fig. 5.6(a). Operation below this line, even with high $\Delta\Lambda$, should be avoided, being the field distribution of the FM very distorted and the beam quality destroyed, as shown by the magnetic field modulus distribution reported in Fig. 5.6(b), which has been calculated at q' equal to 130 W m^{-1}, just below the dashed line. The possibility to maintain SM guiding with larger hole-to-hole spacing allows a significant scaling of the effective area. Figure 5.7(a) reports the calculated FM A_{eff} as a function of Λ, for different values of q' and $\Delta n = -1 \times 10^4$. The effective area

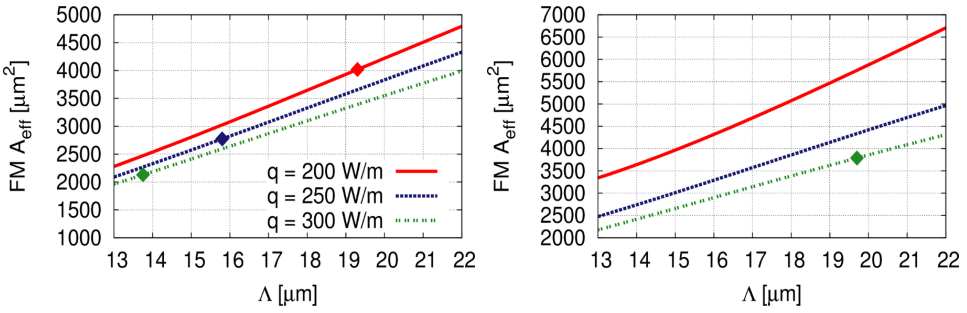

Figure 5.7: Effective area of the FM as a function of the hole-to-hole spacing Λ, for different values of the heat load and (a) $\Delta n = -1 \times 10^4$ and (b) $\Delta n = -2 \times 10^4$. Diamond markers are placed in correspondence with the highest A_{eff} values that can be reached while maintaining $\Delta\Gamma \geq 0.3$. Curves with no markers correspond to heating conditions which allow SM guiding for any Λ value in the considered range .

increases with the pitch, as a consequence of the larger core size, almost doubling its value when passing from Λ equal to 13 µm to Λ equal to 22 µm. The transition to the multimode regime, which corresponds to the maximum Λ which allows $\Delta\Gamma \geq 0.3$ at a given value of q', sets the upper limit to the exploitable effective area, which is indicated with diamond markers on the curves of Fig. 5.7(a). Notice also that the increase of the heat load shrinks the FM field distribution, lowering the effective area for any given value of Λ. As a consequence, the maximum achievable A_{eff} with SM propagation is about 4000 µm^2 at q' equal to 200 W m^{-1}, 2800 µm^2 at q' equal to 250 W m^{-1}, and 2100 µm^2 at q' equal to 300 W m^{-1}, which is obtained with hole-to-hole spacing of 19.4 µm, 15.9 µm and 13.8 µm, respectively. Further increase of the achievable effective area can be obtained by exploiting deeper core down-doping, as can be inferred by the comparison of Fig. 5.7(a) with Fig. 5.7(b), where the same curves are plotted for a SF-PCF with $\Delta n = -2 \times 10^4$. In the latter case, the maximum Λ allowing effectively SM propagation is pushed beyond the limit of the considered range of parameters for q' equal to 200 W m^{-1} and q' equal to 200 W m^{-1}, resulting in a maximum effective area larger than 6700 µm^2 and 5000 µm^2 , respectively. For a

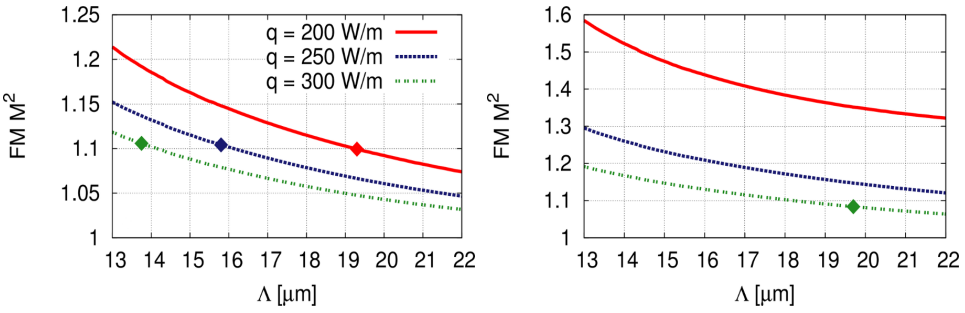

Figure 5.8: M^2 value as a function of the hole-to-hole spacing, calculated under different heating conditions for the FM of SC-PCFs with (a) $\Delta n = -1 \times 10^4$ and (b) $\Delta n = -2 \times 10^4$.

generated heat of 300 W m^{-1} the fiber is SM with hole-to-hole spacing up to 19.7 μm, which corresponds to an effective area of about 3800 μm^2 , providing a significant enhancement over the SF-PCF design proposed in the previous chapter.

5.4 Beam quality

One more critical parameter that must be taken into account is the beam quality. In particular, it is important to ensure that the reduced cladding symmetry and the core down-doping do not cause significant departure of the FM from the ideal gaussian profile, which would void the effort to suppress the HOMs for what concerns the output beam quality. The M^2 factor of the fundamental mode of the SF-PCFs with the same structural parameters that have been considered for Fig. 5.7 has been calculated at q' equal to 200 W m^{-1}, to 250 W m^{-1} to 300 W m^{-1}, according to the method proposed in [112]. As shown in Fig. 5.8(a), the M^2 of the fiber with $\Delta n = -1 \times 10^4$ is below 1.22 for any considered heating condition and pitch size, thereby providing a beam quality comparable to Tm-doped LMA PCFs reported so far [91, 89]. Moreover, the increase of the core generated heat and the scaling of the pitch favor the confinement of the FM, limiting its leakage between the air-holes of the first cladding

q' [W m^{-1}]	Δn	Λ [µm]	$\Delta\Gamma$	A_{eff} [µm^2]	M^2
200	1×10^{-4}	19.3	0.3	4018	1.10
200	2×10^{-4}	22	0.44	6706	1.32
250	1×10^{-4}	15.8	0.3	2772	1.10
250	2×10^{-4}	22	0.45	4963	1.12
300	1×10^{-4}	13.75	0.3	2129	1.11
300	2×10^{-4}	19.7	0.3	3788	1.08

Table 5.1: List of structural parameters and properties of the most relevant SF-PCF designs

ring, to the benefit of the mode shape. As a consequence, a lower M^2 is found with higher q' or Λ values. Notice that the M^2 values corresponding to the maximum hole-to-hole spacing providing $\Delta\Gamma \geq 0.3$, which are indicated with diamond markers in Fig. 5.8(a), are about 1.1 at all the considered heating conditions. This apparently critical M^2 value is probably due to the fact that a somehow constant relation exists between the confinement of the FM and the one of the most detrimental HOM. As a consequence, the combination of heat load and hole-to-hole spacing that allows to have M^2 lower than 1.1, that is to confine the FM enough to almost remove the tails of the field distribution which extend between the first ring of cladding air-holes, also prevents effective suppression the LP_{11}-like mode.

Figure 5.8(b) reports the same results obtained for a SF-PCF with $\Delta n = -2\times10^4$. Notice that the stronger down-doping causes a degradation of the beam quality, which is more evident at the lower temperatures. On the other hand, it is possible to operate in the SM regime with larger pitch size and under stronger thermal load, whose effect is to compensate to some extent the degradation of the beam quality caused by the core index depression. As a consequence, the M^2 obtained for Λ equal to 19.7 µm at q' equal to 300 W m^{-1}, which corresponds to the maximum achievable effective area in SM regime for that heat load, is only 1.08, very close to the ideal M^2 equal to 1 of the diffraction-limited beam. A summary of the results obtained at the considered q'

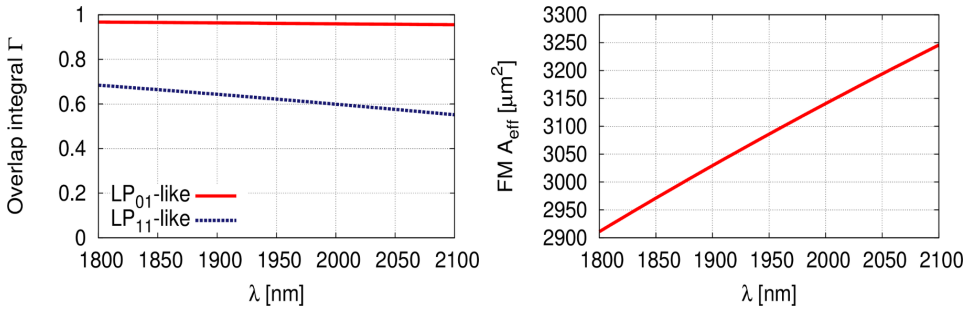

Figure 5.9: (a) Overlap integral of the fundamental LP_{01}-like and LP_{11}-like modes and (b) effective area, calculated for a SF-PCF with $\Lambda = 17\,\mu m$, $d/\Lambda = 0.4$ and $\Delta n = -2 \times 10^{-4}$ at q' equal to $300\,W\,m^{-1}$, as a function of the wavelength.

values with the optimized designs is reported in Tab. 5.1.

It is important to underline that, even if the results presented so far are limited to equal to $2\,\mu m$, the considered SF-PCFs can operate at any wavelength in the Tm gain region without compromising their guiding properties. To give an idea of how the change in wavelength affects the HOM suppression capabilities at high power levels, the overlap integral spectra of the LP_{01}-like and LP_{11}-like modes have been calculated for a SF-PCF with Λ equal to $17\,\mu m$, d/Λ equal to 0.4 and Δn equal to -2×10^{-4} , assuming a heat load of $300\,W\,m^{-1}$. The simulation results are shown in Fig.5.9(a). Notice that the modal discrimination is larger than 0.3 at any λ longer than 1850 nm and that the FM overlap is steadily above 0.95 throughout the whole band. The LP_{11}-like mode is more affected by the change of wavelength, leaking more and more into the cladding as λ increases. As a consequence, its Γ value is reduced from about 0.68 at equal to 1800 nm to 0.55 at equal to 2100 nm. The change of wavelength has a moderate impact on the effective area, as shown in Fig.5.9(b). Indeed an increase of about 10 percent of A_{eff} is observed throughout the wavelength range, from about $2900\,\mu m^2$ at 1800 nm to $3250\,\mu m^2$ at 2100 nm.

5.5 Conclusion

In this chapter, the design of an innovative Tm-doped rod-type double-cladding PCF with reduced symmetry has been thoroughly analyzed by means of a full-vector modal solver based on the finite-element method. The effects of severe heating, due to the large quantum defect of Tm ions, have been included in the model, to account for the behavior of the investigated PCF in a plausible operating scenario, where thermo-optic effect may cause the increase of the core effective index by a few percent. The impact on the guiding properties of the change of the main design parameters, that is the hole-to-hole spacing, the air-hole diameter and the core refractive index, has been evaluated in conjunction with the thermal effects, with the aim to demonstrate the possibility to achieve effective high-order mode suppression and very large mode area at high power levels. The simulation results have shown that for a proper choice of the design parameters it is possible to obtain SM guiding with effective area of about $3800\,\mu m^2$ when a heat load of $300\,W\,m^{-1}$ is generated in the core, and an effective area larger than $5000\,\mu m^2$ with $250\,W\,m^{-1}$ of generated heat. Moreover, a fundamental mode M^2 parameter of about 1.1 has been calculated under these condition.

Chapter 6

Disordered material and random lasing

In this chapter, a 2D disordered structure, similar to that designed by Liang in order to demonstrate random lasing in Mid-IR region [113], has been investigated. After a brief introduction to explain the properties of light transport in disordered media and to introduce the concept of random lasing, the second section is dedicated to the numerical analysis of the structure supposing to work with a passive media. In this structure, the amount of scattering has been varied through the control of holes filling factor, while the impact of disorder has been modified from a periodic lattice to a full random pattern of scatterers, to understand the relation between light transport in disordered media and the degree of disorder. The modal properties have been studied with different numerical strategies, varying the amount of the disorder and the level of scattering in the structure. The first numerical approach, based on Finite Element Method, has been used to evaluate the resonant modes, their spectral distribution, and their confinement degree, considering a lossy structure without any gain effect. The second approach, based on Monte Carlo strategy , has been exploited to obtain information about the statistical parameters, such as scattering distance and travel distance, that influence the light diffusion inside the material. In the third section, the structure has been considered in presence of gain. With the justified hypothesis of weak scat-

tering condition, the structure has been numerically investigated through the help of a custom software based on Monte Carlo method. The software has been implemented combining Monte Carlo method with a simple but complete model which includes the pumping system and the gain with particular attention to consider the local effects due to the resource competition. Structures with different amount of scattering has been simulated, progressively increasing the input power, focusing on the analysis of photon packets travel distance in order to explain the emission behavior. Eventually conclusions are drawn.

6.1 Overview on light transport in random media

Light transport in disordered structures is a wide research topic that covers an ample range of applications. It includes lasers technology [114], spectrometry [115], photovoltaic field where the disorder enhancement is promising to improve the absorption efficiency of thin-film solar cells [116] and speckle-free imaging [117]. Multiple scattering plays a key role in the properties of the disordered optical media, where the dielectric constant is a random function of the spatial coordinates. The multiple scattering phenomenon is quite common in nature and appears in all of the opaque materials, for example clouds, milk or sugar powder. The light, traveling through such materials, is scattered thousands of times in a fashion that can be compared to a random walk [118]. Nevertheless, because of the interference between the light paths inside disordered media, the multiple scattering is a complete coherent phenomenon. This fact leads to the formation of electromagnetic modes [114, 119], which are eigensolutions of Maxwell's equations in the disordered structure.

The scattering intensity is fundamental to explain the light transport. Increasing its contribution, the transport changes from ballistic to diffusive, reaching a localized regime when the scattering is enough intense [120]. Localization can be described as the development of close channels where light is trapped by the feedback due to the scattering [121]. This situation is referred as strong localization and can be reached when the modified Ioffe-Regel criterion $kl \leq 1$ is satisfied, where k is the wave number and l is the photon mean free path [118]. Backscattering is a second

mechanism identified to explain localized regime. Its action is considered a transition between diffusion and localization, therefore it is referred as weak localization [120].

As theoretically predicted by Letokhov [122] and later demonstrated by Lawandy [123], the disorder combined with the amplification given by an active material can be exploited to create a new class of lasers with particular properties. Inside a disordered active material the light, forced to travel through longer paths, can reach the lasing threshold showing an emission spectrum characterized by narrow peaks apparently not correlated with each others [114]. Comparing to a traditional laser, the feedback mechanism is due to the scattering and not to the action of an optical cavity. This class of laser is normally referred as random laser [124]. Random lasing is a complex phenomenon, which can not be explained with the only help of localization theory. In a strong scattering regime, the interference can give birth to amplified optical modes characterized by a high Q-factor and spatial separation, namely localized modes. In a low scattering regime, the light is diffused all over the material and lasing peaks can be explained as the amplification of the photons which experience very long paths. Such events can be improperly referred as extended open modes [125]. While there is a clear relation emerging from the comparison between leaky modes and amplified modes in localized regime [126], such relation appears very weak in diffusive regime. A rigorous explanation of this behaviour has been given in [127], where it is evidence the substantial difference between passive and active modes. While the passive modes can be described as poles of a unitary scattering matrix, in an active system the gain makes the scattering matrix no more unitary. A direct consequence is the onset of a shift in frequency and field distribution between modes of passive system and amplified modes. For high Q-factor modes in localized regime, this shift is minimum. In contrast, in a weak scattering regime such shift leads to a complete inconsistency between leaky and amplified modes. The complexity of random lasing phenomenon emerges from several experiments, where it has been shown that modes can interact with each others [128], and the emission spectra can be characterized by the co-existence between localized and extended modes [129, 130].

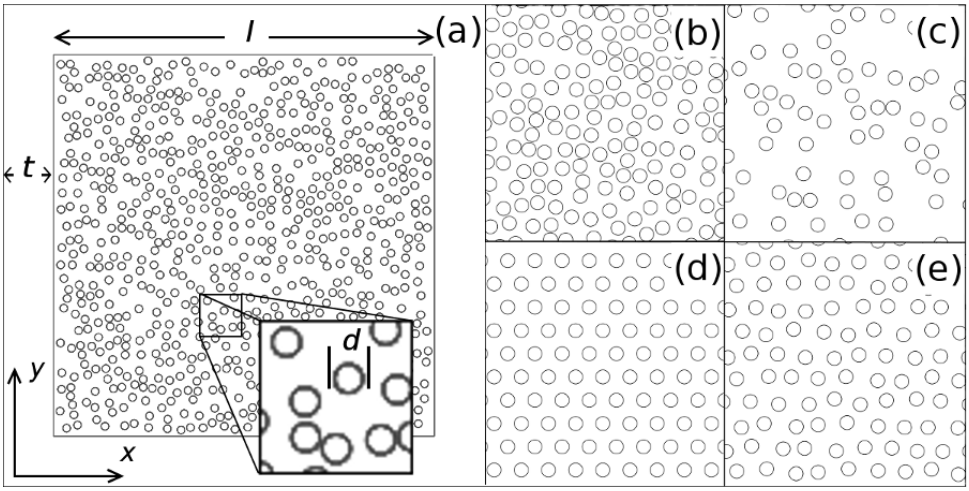

Figure 6.1: (a) Schematic of a full disordered structure with filling factor $FF = 0.3$. Detail of a structure with filling factor: (b) $FF = 0.5$, (c) $FF = 0.1$. Detail of a structure with shift coefficient: (d) $K_s = 0$ equivalent to a triangular lattice and (e) $K_s = 0.6$.

6.2 2D planar structure under investigation

The structure under investigation has been modeled on the device, developed by Liang in [113] in order to operate as a random laser source in the Mid-IR region with a wavelength around 10 µm which is approximately equivalent to a frequency of 30 THz. The main structure is a square slab with side length l equal to 150 µm and thickness t equal to 2.2 µm, obtained in a Quantum Cascade Laser (QCL) heterostructure of $In_{0.53}Ga_{0.47}As/In_{0.52}Al_{0.48}As$ with a refractive index n_s equal to 3.35 . Considering the ratio between the slab surface width and the thickness, and considering that the QCL heterostructure guides primely TM modes [131], it is possible to model the system as a 2D structure, where x and y axes are in plane. Random structures in 2D approximation play an important role in this research field, being the simplest systems to achieve a complete light transport transition from diffusive to localized regime, and being enough versatile to be engineered [132, 133]. A pattern

of circular air holes, the scatterers, with a diameter d equal to 3 µm and a refractive index n_a equal to 1, has been obtained inside this slab, with different dispositions according to the strength of the scattering and to the amount of disorder. The scattering has been varied modifying the number of holes, which is equivalent to modify the filling factor FF [126], a parameter defined as the ratio between the holes total area and the square slab area. The disorder has been varied generating the holes pattern exploiting two different algorithms. The first random pattern has been obtained choosing x and y components of the holes centers, uniformly distributed between 0 and l, avoiding superpositions between holes and discarding the holes that partially fall outside the slab. To obtain a more realistic structure, a minimum distance $d_{\min}$, with a value of 150 nm, has been assigned between adjacent holes. An example of full random pattern structure with FF equal to 0.3 is shown in Fig. 6.1(a), while some details of full random patterns with FF equal to 0.5 and to 0.1 are shown respectively in Figs. 6.1(b) and 6.1(c). The second algorithm is intended to gradually move the holes from a periodic triangular lattice to a random configuration, using the parameter K_s which defines a random variable S as the shift of the holes centers with respect to the holes position in the periodic lattice:

$$0 \leq S \leq K_s \frac{\Lambda - d_{\min}}{2} \quad , \tag{6.1}$$

where Λ is the pitch of the periodic lattice and $d_{\min}$ is the minimum distance between holes. The angular direction of the shift is also a random variable and it is uniformly distributed between 0 and 2π. Figure 6.1(d) depicts the triangular lattice while Fig. 6.1(e) shows an example of pattern shifted with a weight equal to 0.6, both of these structure are generated considering a filling factor equal to 0.3.

6.3 Passive medium

6.3.1 Modes spectra analysis

This analysis has been performed using the FEM in order to solve for Maxwell's equations in the frequency domain. The slab, modeled as shown in Fig. 6.1(a), has

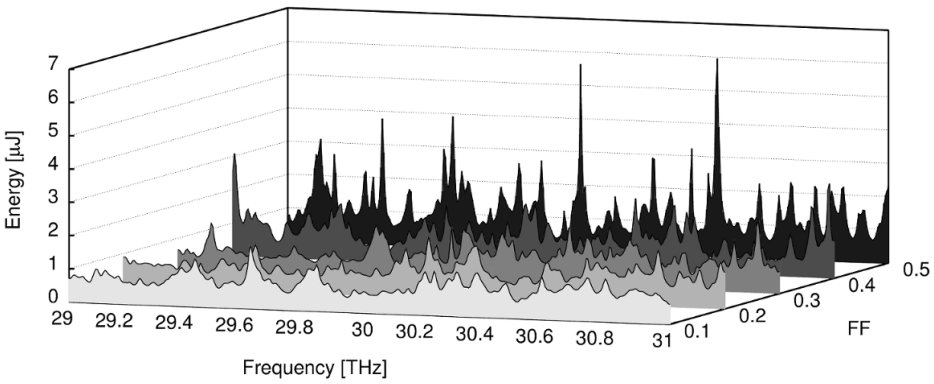

Figure 6.2: Spectral energy distribution between 29 THz and 31 THz varying the scatterers filling factor.

been surrounded by an empty region of 30 μm which terminates with a Perfectly Matched Layer (PML) framework. The boundary conditions have been chosen according to the scattering theory. These strategies pledge an irrelevant reflection due to the boundaries, fundamental in this case of study. In order to obtain solutions totally independent from the discretization of the problem, a particular attention has been given to the mesh parameters, setting the maximum elements size less than one seventh of the wavelength. In the setup phase of this FEM simulation work, different levels of mesh fineness have been tested in order to improve the accuracy of the solutions keeping the calculation time reasonably small. The maximum elements size has been chosen equivalent to the reference wavelength inside the media, which is similar to the expected fluctuation of solutions due to the light interference. With a heuristic procedure, the elements size has been decreased evaluating the numerical stability of a reference group of eigenfrequencies near 30 THz region. It has been observed that for elements size smaller than one seventh of the wavelength the solutions remained constant with a large number of digits, enough to obtain a confident values of quality factor, as further defined.

The first study has been focused to investigate the spectral behavior of the structure, performing a sweep in a range between 29 THz and 31 THz, using a step of

5 GHz. Due to the nature of the slab material, a QCL heterostructure, the modes of interest, i.e. TMs with $H_z = 0$, have been stimulated imposing 1 A of line current, perpendicular to the *xy* plane. As emerged in [113], the slab has been uniformly pumped to stimulate TM modes over the whole structure. To obtain a similar behavior, the source injection current has been distributed over a large number of points, precisely 5000, located on the active substrate. With this number, the average distance between two points is roughly the wavelength in the medium. The location of these points is carried out by the same algorithm that generates the full random pattern. For the output, the electromagnetic energy has been recorded on the area of the square slab. Following this operative method, the impact of the scattering weight on the system has been investigated. Numerous realizations of full random patterns, with filling factor varying in a range from 0.1 to 0.5, have been simulated. Figure 6.2 shows the comparison between five energy spectral distributions starting from a low scattering case with *FF* equal to 0.1 and ending to strong scattering case with *FF* equal to 0.5 . It is possible to notice the evolution of energy inside the system. With a filling factor smaller than 0.3, the spectrum appears as a sequence of smooth peaks and valley, with rare well defined peaks. At filling factor equal to 0.3, the first sharp peaks arise sharing the band with wider gather of energy. At values of filling factor larger than 0.3, peaks become narrow and well separated between each other. To give an interpretation of these spectra, a second study has been performed using FEM solver searching for eigevalues and eigevectors of the electromagnetic problem in frequency domain. Investigating for the modes located near the frequencies corresponding to a maximum of energy, it is possible to see that a sharp and narrow peak corresponds to a well definite mode, while a wide and smooth maximum of energy is associated to the superposition of different modes which share the same band and the same area in the slab. Defining the quality factor as:

$$Q_{\mathrm{f}} = \frac{\omega}{2|\delta|} \quad , \tag{6.2}$$

where δ is the attenuation and ω is the resonant frequency of the complex eigenfrequency $\omega_c = j\omega + \delta$, it is easy to show that the Q_{f} is high when a peak is sharp and narrow while is low in correspondence of a wider energy maximum. A pictorial

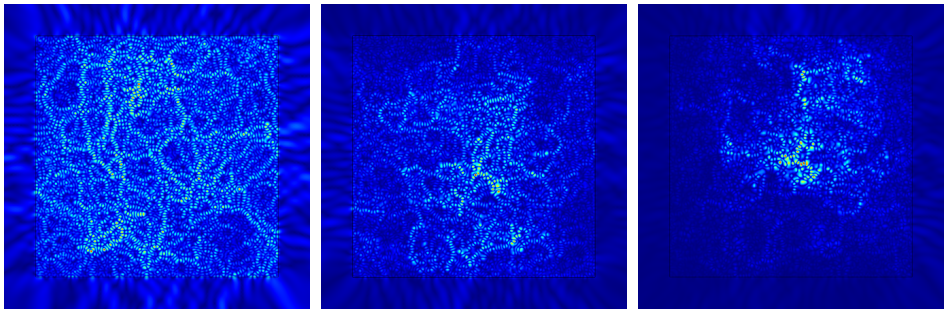

(a) (b) (c)

Figure 6.3: (a) Mode field at 29.60 THz in the structure with $FF = 0.1$. (b) Mode field at 29.91 THz in the structure with $FF = 0.3$. (c) Mode field at 29.98 THz in the structure with $FF = 0.5$.

example is reported in Figs. 6.3(a) - 6.3(c). Figure 6.3(a) shows the principal mode located at 29.60 THz in the structure with FF equal to 0.1 . It is clearly a lossy extended mode, occupying all the area of the slab, its calculated Q_{f} is equal to 1247 and its nature can be associated to a diffusive transport. Figure 6.3(b) shows the mode located at 29.91 THz in the structure with FF equal to 0.3 . Unlike the previous one, this mode corresponds to a narrow peak and its quality factor is substantially higher with a value of 2819 . It is a mode with a transient behavior toward a localized regime, which is reached in the structure with filling factor equal to 0.5 , as depicted in Fig. 6.3(c), where it is possible to see the mode corresponding to peak at 29.98 THz. This mode exhibits a Q_{f} larger than 4500 .

Following the same procedure described previously, the 2D slab has been analyzed shifting from a condition of perfect periodicity to a disordered situation. Triangular lattice has been chosen as the basic periodic pattern, while randomness has been added varying the shift coefficient K_s from 0.1 to 0.9. Figure 6.4 shows the change in the spectrum at different level of K_s, the filling factor of these random patterns is set at 0.3 . The spectrum of triangular pattern is almost flat exhibiting some isolate

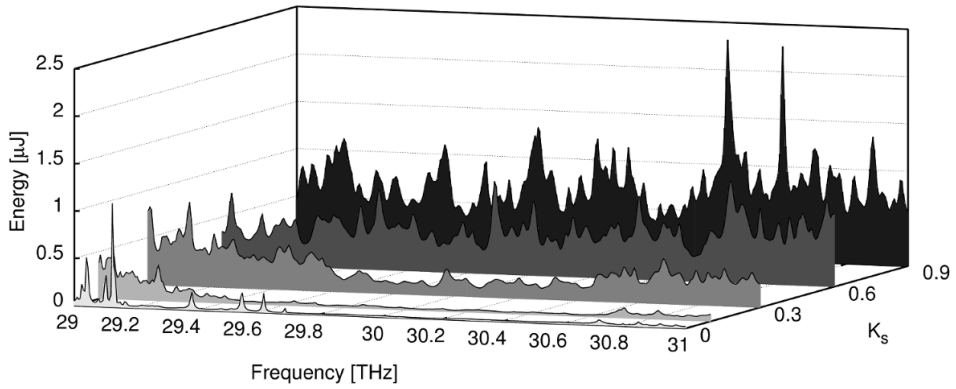

Figure 6.4: Spectral energy distribution between 29 THz and 31 THz varying the shift coefficient K_s, the filling factor is 0.3 .

energy peak in correspondence of the frequencies where the solutions of Maxwell's equations assume a form with an envelope that varies periodically with the pitch of the lattice. These solutions show a quality factor very high, for instance the peak, located at 29.12 THz, has a calculated Q_{f} greater than 6100 as shown in Fig. 6.5(b), this value is two times larger with respect to the maximum Q_{f} found in the full random pattern. Disturbing the positions of the holes from the periodic lattice, it is possible to see evolution of the energy inside the slab area. With K_s equal to 0.1, corresponding to a very small shift, some wide and distinct energy stacks starts to grow in correspondence of the periodic lattice peaks which are absorbed inside the stacks. This trend is more clear at K_s equal to 0.3, while at K_s equal to 0.6 the energy spectrum is uncorrelated with respect to the periodic spectrum. With values of K_s larger than 0.6, the spectrum is actually similar to the one obtained using the full random algorithm. This evolution can be also highlighted examining the evolution of the average quality factor. Figure 6.5(a) shows the mean Q_f calculated at different *FFs*, referring to the periodic lattice, to the full random pattern, and to different shift values . The mean has been calculated by averaging 400 modes, roughly all the modes in the band under examination, using 10 different realizations of disorder. The Q_{f} curve of periodic

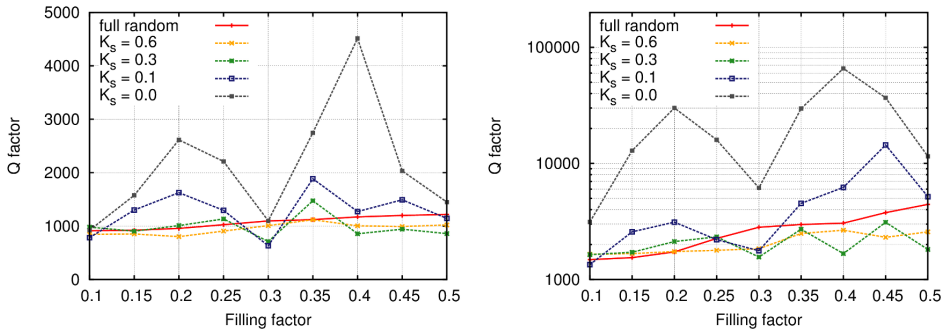

(a) (b)

Figure 6.5: (a) Average quality factor calculated at different values of filling factor and different values of K_s. (b) Peak quality factor calculated at different values of filling factor and different values of K_s.

lattice gradually gets close to the Q_f curve of the full random pattern, increasing the value of K_s. At $K_s = 0.6$, the average quality factor is practically equal to the full random pattern. This trend is more evident when strong resonant frequencies in the periodic pattern fall inside the band between 29 THz and 31 THz, this is evident for the patterns with filling factors equal to 0.2 and to 0.4.

It is interesting to notice that the random shift, generated by the algorithm previously explained, and described by the coefficient $K_s = 0.6$, is particular small, remaining highly correlated with the periodic pattern, as it is evident in the comparison between Figs. 6.1(d) and 6.1(e). Nevertheless, such disturbance with respect to the periodic lattice is enough to lead the system to show a spectrum similar to a full random generated pattern . This consideration suggests to give an alternative interpretation of disorder. As previously underlined, the localization, one of the key phenomenon that leads to random lasing, can be explained as the development of closed scattering paths in the case of strong localization, or as backscattering enhanced paths in the case of weak localization. In both cases, these paths shall be a multiple of the

resonant wavelength, which can be written as:

$$\lambda = \frac{1}{m} F\left(\sum^{n} l_s\right) \quad , \tag{6.3}$$

where λ is a generic resonant frequency, l_s is the scattering distance, defined as the free path between two scattering events [124], m is a positive integer and $F(\bullet)$ is a function that weighs all the possible jumps between two scatterers. λ and l_s are random variables. Although $F(\bullet)$ can be written explicitly only for special and easy cases, for instance a multilayer random structure [134, 135], Eq. (6.3) suggests that the resonant modes statistic depends on the statistic of the scattering distance partial sum. Under this point of view, a small disturbance in the periodic lattice, i.e. a random variable l_s with a small variance, can generate resonant frequencies with a large variance, if the sum is large enough. Effectively, to understand the modes statistic, it is helpful to investigate the statistic of the light travel distance inside the structure, which is equivalent to $\sum^{n} l_s$.

6.4 Statistical analysis

In order to collect informations about the statistic of light diffusion in this system, it has been chosen to simulate the structure through a Monte Carlo method , which is particularly suitable to analyze complex disordered structures [136, 137]. A custom software has been implemented assuming that photons are traveling grouped in packets identified by their energy. The scattering has been calculated in accordance with the Mie theory, approximating the phase function with the Henyey-Greenstein function [138]. To better simulate the structure, the program has been provided with a pumping system and with a complete model which implements absorption, spontaneous and stimulated emission. To make the software numerically efficient and reliable, random number generation for Monte Carlo operations, has been implemented with a single instance pseudo-random sequence, using singleton design pattern, and using the Marsenne Twister-64 bit algorithm provided by C++11 standard library. Further details on Monte Carlo method and its implementation will be given in the section dedicated to the active medium.

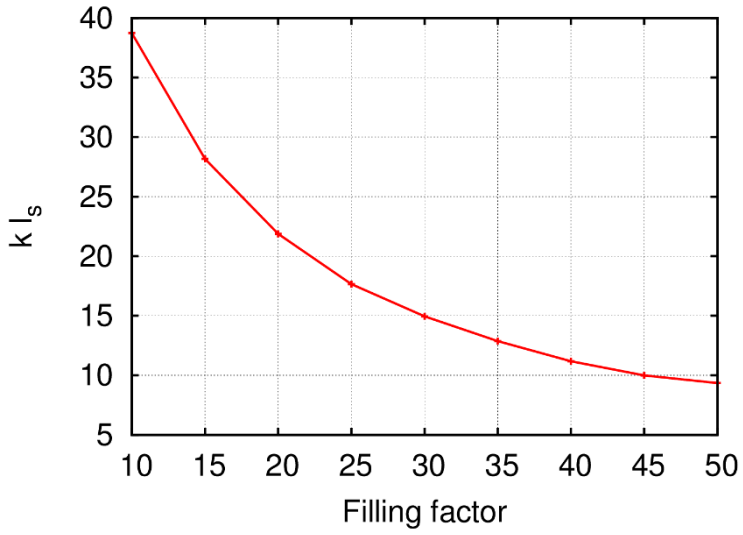

Figure 6.6: Product between the wavenumber k and the scattering mean free path $\bar{l}_s$, considering a full random holes pattern, varying the filling factor .

The simulations has been performed supposing to electronically pump the system at negative time, to stop the pump at $t = 0$ and to start spontaneous emission at positive time. The system has been set and with a negligible absorption and without gain, to be coherent with the simulations described in the previous section. With these settings, the software has been run in order to diffuse and collect statistics from a large number of photons packets, roughly 100×10^6. The structure has been simulated varying the filling factor and the shift coefficient, in agreement with the FEM analysis performed in the previous section, searching for the statistic of the photons scattering distance, l_s, and for the statistic of travel distance, $\sum^n l_s$. For every disorder configuration and for every scattering configuration, results have been averaged over 10 different realizations. Figure 6.6 shows the product between the wavenumber k and the scattering mean free path $\bar{l}_s$ calculated with the structure generated with the help of full random algorithm and varying the FF parameter. It is possible to notice that there is no circumstance where the Ioffe-Regel criterion has been fulfilled, as the

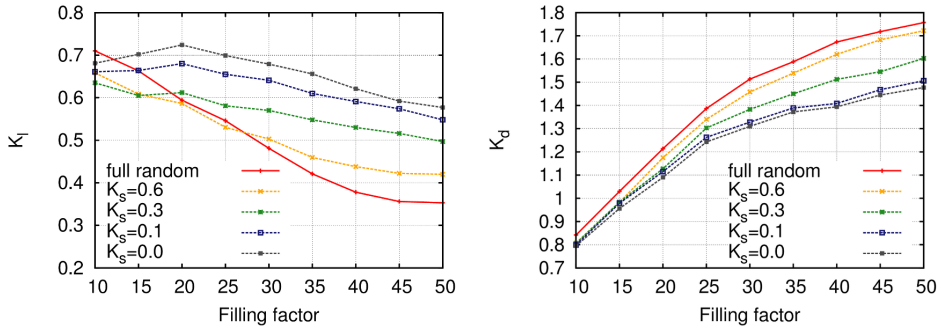

(a) (b)

Figure 6.7: (a) Coefficient K_l, i.e. weighted variance of l_s, vs filling factor for various shift values form periodic lattice. (b) Coefficient K_d, i.e. weighted variance of travel distance, vs filling factor for various shift values form periodic lattice.

minimum calculated value of $k \cdot \bar{l}_s$ is equal to 9.2 when the FF is equal to 0.5 . This result implies that it is not possible to reach a strong localization in these structures, therefore the evolution of localization shown in Figs. 6.3(a)-6.3(c) can be explained using the weak localization mechanism. Similar conclusion has been suggested also by Liang [113].

To better understand how the degree of disorder affects the structure, two important parameters have been defined:

$$K_l = \frac{\sigma_{ls}^2}{\left(E[l_s]\right)^2} \quad , \tag{6.4}$$

where K_l is the variance of the scattering distance weighted with the scattering squared mean free path, and:

$$K_d = \frac{\sigma_{\sum ls}^2}{\left(E\left[\sum l_s\right]\right)^2} \quad , \tag{6.5}$$

where K_d is the variance of travel distance weighted with its average elevated to the square. In Fig. 6.7(a), the K_l trend vs the filling factor has been depicted for various

values of disorder. Considering that the scattering mean free path is weakly dependent on the disorder parameter, it is possible to notice that low disorder structures have a high variance and a K_l roughly flat profile varying the filling factor, while higher disorder structures tend to decrease the variance with the increase of filling factor. This fact can explain the reason why periodic structures support a few number of localized modes with respect to random structures. Encountering a larger scattering step variance, modes tend to spread through the structures and only few frequencies, enveloped with the lattice pitch, can resonate in the system. It is worth noting that for a low filling factor all the disorder configurations have an high K_l, therefore all the modes are extended and the transport regime is diffusive. A similar conclusion can be inferred analyzing the coefficient K_d, Fig. 6.7(b). This parameter is quite useful because it gives informations about localization. When the system begins to support localized modes, the value of K_s increases and the curves at different values of disorder start to separate with each others, showing that high disorder configurations support more resonant frequencies with respect to periodic lattice and low disorder structures. This is evident when the filling factor is high. When filling factor is low all the modes are extended and all the structures have a similar behavior. Furthermore, Fig. 6.7(b) shows that a little increase of the shift from periodic lattice pushes the curves to approach the full random behavior. K_d can measure how fast a disturbance from periodic lattice can behave like a random structure, this means that K_d is a good randomness weight for these planar disorder structures.

6.5 Active medium

6.5.1 Monte Carlo method in active medium

Monte Carlo method is commonly used in bio-imaging and microscopy to model photons propagation in scattering media. With the advantage to be simple and computationally not expensive, this method assumes that photons act as particles interacting with the scattering media with a sequence of random and mutually independent events. Consequently, Monte Carlo strategy ignores the light interference. Even though a correct numerical description of random lasing phenomenon should be car-

ried out exploiting the solution of Maxwell equations, the approximation given by the use of Monte Carlo method can be considered acceptable in the weak scattering region [139]. Furthermore, Monte Carlo makes available the statistics of light diffusion inside the media and makes possible the evaluation of disordered systems in function of filling factor, which is a global parameter independent of a particular realization of random pattern. This fact can be successfully used in the preliminary step of random laser design. Normally Monte Carlo method is applied in passive media where the photons action is independent. To investigate the behavior of the disordered active structure with variable filling factor, a software based on Monte Carlo method has been implemented including a pumping scheme and a gain model. The photon energy has been chosen as the main physical quantity to describe the evolution of the system. The structure has been divided in a discrete grid and every block of the grid has been described as a bucket of energy which can be empty in the case of pump lack or full in case of saturation. Every photons packet, passing in a particular bucket region, interacts with it absorbing energy via stimulated emission. The amount of energy in the bucket is also decreased by spontaneous emission which is the starting spark of random lasing phenomenon in the structure proposed. The equations of spontaneous emission, stimulated emission and absorption have been written to show the energy:

$$\Delta E_{sp} = E_b \left(1 - e^{A\,\Delta t}\right), \tag{6.6}$$

$$\Delta E_{th} = E_{pk} \left(1 - e^{-\Sigma\,\Delta l}\right), \tag{6.7}$$

$$\Delta E_{st} = E_{pk} \left(e^{\sigma \frac{E_b}{h\nu V_b} \Delta l} - 1\right), \tag{6.8}$$

where E_{sp}, E_{st} are the energy released by the upper state through spontaneous emission and stimulated emission respectively, E_{th} is the energy absorbed by the structure and dissipated through thermal effects. E_b and E_{pk} are the energy of a generic discrete bucket and the energy of a generic photon packet running in the media. The parameters A, Σ and σ are the rate of the spontaneous emission, the absorption coefficient and the emission cross section respectively, h is the Planck's constant, ν is the working frequency and V_b is the volume of a single cell. Δt and Δl are respectively

the time step and the distance step emerging from the discretization. The aim of the bucket division is to better describe the interaction of photons packets with matter and their competition to obtain amplification, assuming that carriers diffusion inside the matter is much slower respect to the photons diffusion. To model the disordered QCL substrate, some simplifications have been made. The system has been assumed as a three-level system, operating at a cryogenic temperature of 78 K. Under this realistic consideration, photon re-absorption can be neglected and the Eq. (6.7) can be written considering only the thermal losses. The population inversion is due by the electrons injected in QCL stack through a pumping mechanism which fills equally all the buckets with an energy $\Delta E_b = P\Delta t$, where P the pump power. The gain cross section σ includes the contribution of all the stages in the cascade stack. The spontaneous emission has been modeled randomly choosing a number M of emission cells every time step. The scattering action has been concentrated on scattering centers and the deviation angle statistic has been calculated using the Mie theory with the approximation given by the Henyey-Greenstein function.

6.5.2 Simulations and results

The active structure, with full random lattice, has been simulated using three different values of filling factor: 0.30, 0.25 and 0.18, as in [113]. These FF values suggest a diffusive regime, as shown in the modes evolution depicted in Figs. 6.8(a)-(e). Furthermore referring to these FFs, the calculated Q-factor is low and the Ioffe-Regel criterion is not fulfilled, as shown in Fig. 6.6. As a consequence, the use of Monte Carlo method, which neglects the interference effect, appears justified. For every value of filling factor, ten different realizations of disorder have been considered and the statistical results collected from the simulations have been averaged. The simulations have been performed progressively increasing the input power from 0 to 40 W, which is equivalent to a current density range from 0 to 15 kA cm^{-2} according to the voltage/current characteristic shown in Fig. 6.9(a) and considering a pulsed operation with pulse length of 200 ns and repetition rate of 10 kHz. To model the QCL substrate, the parameters in Eqs. (6.6)-(6.8) have been set to the following values: Σ equal to 1.6×10^5 m^{-1} [140], A equal to 1.7×10^7 Hz and σ equal to 4.5×10^{-21} m^2

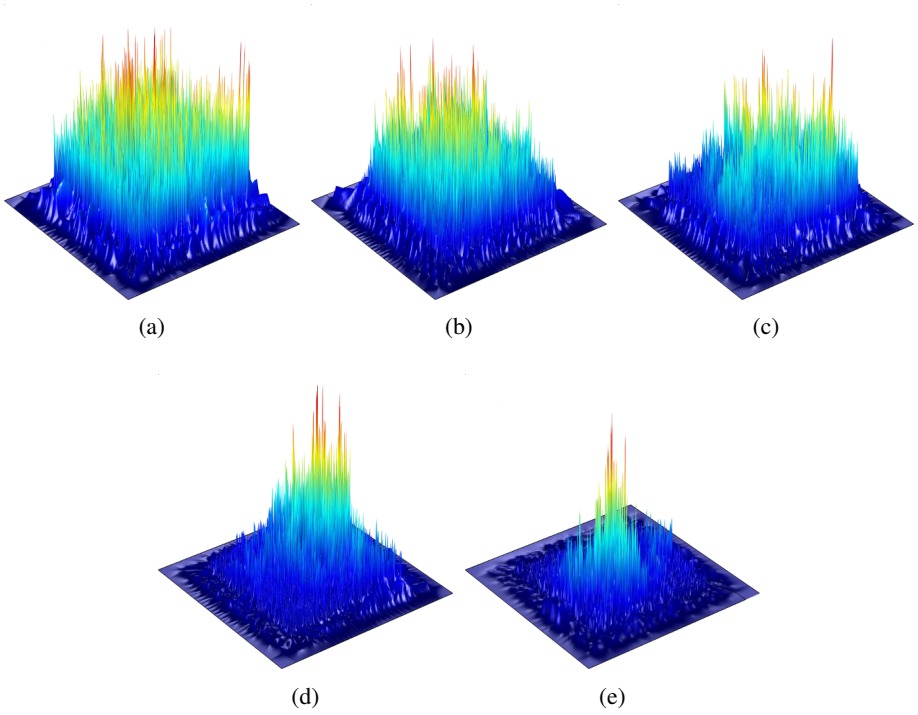

Figure 6.8: Normalized electric field module at different FFs: (a) 0.18, (b) 0.25, (c) 0.30, (d) 0.36, (e) 0.42. Localization onset arises for FF greater than 0.4 .

[141]. Figure 6.9(a) shows the output power versus the current density, it is possible to notice the dependence of the threshold, which requires higher current with the decrease of the filling factor. Furthermore, the transition from non emission to emission region is sharper with respect to higher filling factor. The results obtained by simulation are comparable with experimental results shown in [113]. To better understand the process of amplification which occurs inside the slab, the software has been exploited to record the travel distance of each photons packet form its emission to its life termination, which can be a total absorption or an emission outside the slab. The average travel distance is shown in Fig. 6.9(b). For small current density values, far from the threshold, the absorption dominates over the stimulated emission and the

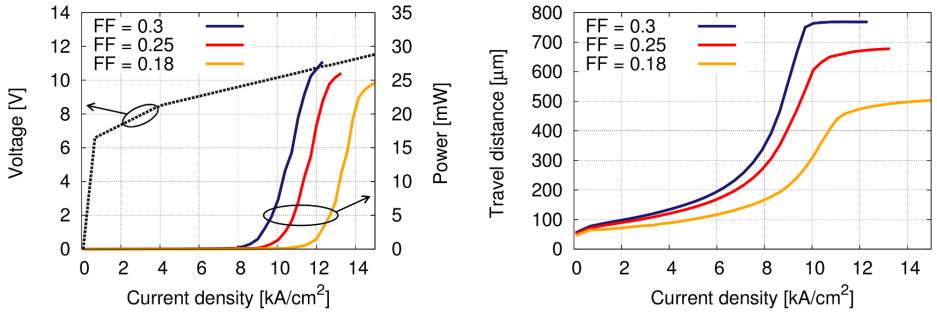

(a) (b)

Figure 6.9: At left: voltage/current characteristic used for the simulation. At right: calculated Output power vs Current density at different values of filling factor FF. (b) Calculated average photon travel distance vs current density.

weak spontaneous emission can not be amplified. The average path length remains low, with a value comparable with slab side, and exhibits a modest slope. Approaching the threshold, the average travel length increases quickly reaching a saturation values just beyond the threshold point. The saturation length can be explained with the equilibrium between the amplified stimulated emission and the output power due to the slab size, while the transition zone before the threshold reflects the gain coefficient trend which locally can become positive with respect to the dynamic of packets diffusion. Such transition area is larger for smaller value of filling factor, justifying the smoother threshold.

The issue emerging from the previous considerations is related to the relative amount of stimulated emission with respect to non-amplified spontaneous emission of the output. Following the idea which explains random lasing in weak scattering as a contribution of open modes, i.e. the development of photon packets with a path enough long to onset lasing phenomenon [136], the Monte Carlo software has been exploited to investigate the statistic of photon packets. The results, shown in Fig. 6.10(a), depict the statistic (probability density function - pdf) of the travel length d_t normalized to its average value $E[d_t]$ in the case of $FF = 0.3$. Four different input

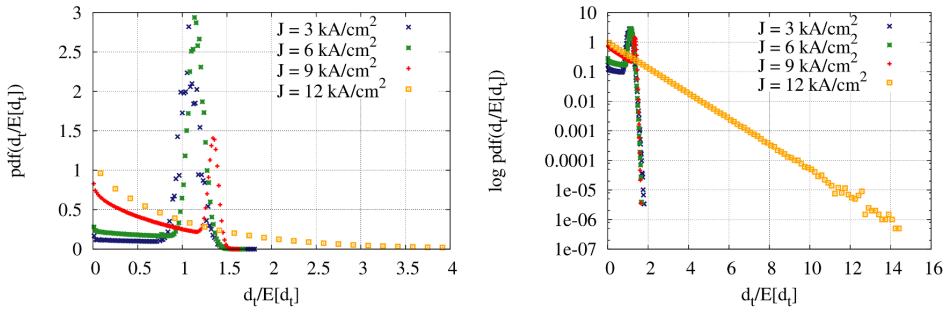

(a) (b)

Figure 6.10: Probability density function (pdf) of the travel length d_t normalized to its average $E(d_t)$ at FF equal to 0.3, written in linear scale (a) and in logarithmic scale (b), calculated at different values of current density J.

current densities have been chosen to exhibit the statistical evolution of the system: 3, 6, 9 and 12 kA cm^{-2}. The first and the second value are in a region far from the threshold, the third is in threshold proximity and the latter is in the emission region. Analysing the plot, it is possible to notice that in the lossy region the majority of the photon packets is characterized by a travel distance almost equal to the average distance, with a distribution that can be roughly compared to a narrow gaussian. In the emission region, instead the pdf is clearly described by a negative exponential distribution. The transition region near the left side of the threshold shows a distribution which is a composition of both these behaviours, revealing an evolution from gaussian to exponential. This scenario is in agreement with the open modes interpretation of the diffusive regime, which describes a system dominated by spontaneous emission at low pumping level, and a system where long path packets can gain enough to lase at a robust pump level. The onset of long path packets is revealed by the transition to negative exponential distribution, as it is shown in Fig. 6.10(b), where the pdf is plotted in logarithmic scale. A relevant fraction of packets has a travel length several times longer than the average.

The travel length statistic dependence on the scattering straightness is also rele-

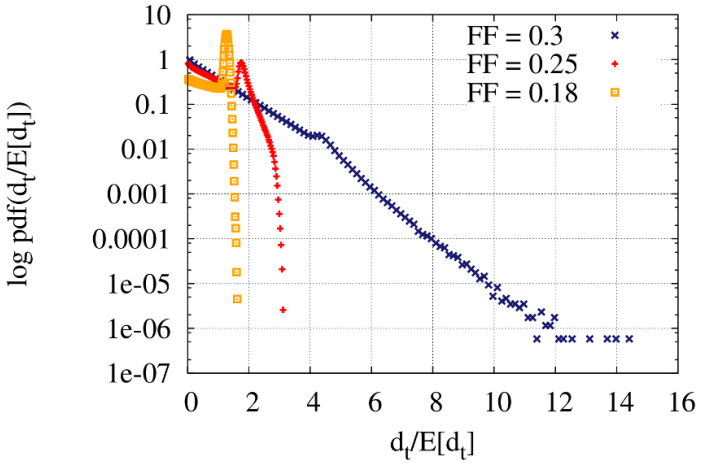

Figure 6.11: pdf calculated for various values of FF at $J = 10\,\mathrm{kA\,cm^{-2}}$, shown in logarithmic scale.

vant. As previously remarked, the filling factor influences the average travel length but the key role is played in relation with the pumping mechanism and the dynamic of the photon diffusion. Figure 6.11 shows the distribution of the travel length at different filling factor values, calculated at the input of $10\,\mathrm{kA\,cm^{-2}}$. Such location is interesting because it groups the statistics at the threshold transition increasing the scattering impact. In the case of $FF = 0.3$, the system is just beyond the threshold revealing the exponential distribution, while at $FF = 0.18$ the distribution is roughly gaussian. The case of $FF = 0.25$ is situated on the threshold transition while the pdf is evolving to exponential shape. These plots clearly explain the sensibility of the investigated planar slab to the change of filling factor. A proper design of the filling factor can, not only tailors the threshold but also the quality of the emission.

6.6 Conclusion

A disordered optical planar structure has been numerically investigated in order to show the modal properties and random lasing effect in the Mid-IR region, around

10 µm. At first, the structure has been considered composed by a passive material and the analysis has been focused to show the nature of light transport, varying the amount of scattering, through the control of filling factor, and the impact of disorder from a periodic lattice to a full random pattern of scatterers. With the help of a Finite Element Method solver, the modes energy distributions has been investigated in a band between 29 THz and 31 THz, highlighting the relation between peaks of energy and resonant frequencies. A clear pictures of quality factor evolution has been given and the transition between diffusive transport regime and localized regime has been identified when the filling factor overcomes 0.3. A particular behavior of the structure, where a small disturbance of the periodic lattice induces the system to acts like a full random structure, has been exhibited, and therefore an explanation has been proposed, underlining the dependence of modes spectral properties on the statistic of light travel distance in the structure. In order to verify this hypothesis, a custom and Monte Carlo method based software has been developed. With this software, the diffusion of photon inside the system has been simulated and information about the statistic of important parameters, like scattering distance and travel distance, has been collected. Two new parameters, the weighted scattering distance K_l and the weighted travel distance K_d have been defined. It has been shown that these parameters can explain the evolution of the modal properties varying the filling factor and the disorder weight. In particular, K_d has been identified as a key parameter to measure randomness in this 2D structure.

In the second step, the structure has been investigated in presence of gain. Thanks to the previous observations it has been assumed that such system is working in a weak scattering region, and the open modes interpretation of light diffusion has been selected to describe the system behavior. A set of simulations, using the software based on a Monte Carlo method, has been performed varying the input current density and the scattering amount, set through the filling factor parameter. The focus has been given to the analysis of photon packets travel distance in order to explain the emission behavior. Results shown that the emission threshold is correlated to the evolution of the travel length statistics from a gaussian-like to an exponential distribution. This fact justifies the amplified long path packets interpretation to explain

lasing emission, dominated by the stimulated emission. Furthermore, the emission characteristics calculated with the application of the modified Monte Carlo method are in good agreement with experiments. This suggests that the simple and resource-inexpensive model proposed can be successfully applied to study and design a random system in regime of weak scattering.

Conclusion

Optical fiber technology has a tremendous impact on the modern society. While optical fiber is the primary transport medium in long range communication, because of its superior advantages in terms of signal attenuation, transmission bandwidth and transmission speed, its use is not limited in the telecommunication field. Optical fiber offers a reliable platform in laser technology, which can compete and overcome traditional solid-state or gas lasers in many applications. From the introduction of rare earth doped fiber amplifiers, fiber has been regarded as an excellent candidate to revolutionize lasers technology. The high gain offered by rare earth doped fiber amplifiers is not the only reason that motivates fiber laser success. The main attractive feature is the geometry of the fiber itself. A cylindrical waveguide with a μm core can emit a near-gaussian, small and intense output spot. On the other hand, the geometrical characteristic of the fiber, i.e. a cylinder with a small diameter compared to its length, is a huge advantage in terms of heat dissipation, pushing the fiber to be an ideal medium in high power fiber lasers, where thermal management is critical. Furthermore, fiber technology offers the possibility to tailor the characteristic of light propagation, permitting single mode operation which is a fundamental requirement to obtain near-diffraction limited high quality output beam. These features, mixed with the additional possibility to design flexible and compact fiber laser system, are extremely attractive in the many applications. In fact, fiber lasers, both in continuous wave and pulsed operation, are perfect in all of those applications where high power density and emission quality are fundamental, as an example industrial applications like machining, cutting, welding, micro drilling, surface scribing or surface texturing.

The main requirements for a superior quality fiber laser, operating at high power, are the efficiency or power conversion and the total power that can be delivered. The first requirement is achieved with the use of double cladding pumping which permits the more efficient cladding pumping, while the second requirement is obtained with the use of large mode area fibers. Enlarging fiber core conflicts with the single mode operation, as larger core supports propagation of many modes. Traditional step index fibers have technological limitations which impede to significantly enlarge mode area. Consequently, for high power fiber laser solutions, different fiber designs shall be exploited, in particular the possibility of tailoring light guidance offered by microstructured photonic crystal fibers (PCF) represents the best option. So far the remarkable results has been achieved in the high power laser technologies, in terms of total power delivered in continuous wave operation or in terms of peak energy in pulsed operation, thanks to the use of photonic crystal fiber design. Most of these results have been obtained in the operating region of 1 μm exploiting the high energy conversion efficiency offered by ytterbium.

However, in recent time the attention of scientific world is focusing on laser sources emitting around 2 μm. Such interest is fostered by the large amount of practical applications in this region of emission, which range from soft tissue surgery and medical applications, to sensing and long ranging arriving to telecommunication. Also in this field, fiber lasers can play a primary role. In particular, thulium ions can be successfully used as dopant in fiber amplifiers and lasers for 2 μm laser operation. Nevertheless thulium, because its high quantum defect, is not endowed with the high efficiency which characterizes ytterbium. Thermal related problems, like thermal lens effect, can limit the effective employment of thulium, preventing a robust single mode operation and consequently decreasing the beam quality achievable. In this context, fiber design becomes critical. A simple scaling of preexisting fibers used for 1 μm region is not an optimum solution, in terms of thermal efficiency and in terms of bending resistance. So, a specific fiber design tailored on the thulium characteristics and to the different operating wavelength is a primary goal to improve the sate of art of 2 μm laser sources.

Under the context given by such preconditions, the work done in this PhD project

has been focused on photonic crystal fiber amplifier design suitable for 2 μm operation with thulium doping. Design work has been done with the help of numerical tools created and optimized by the Group of Applied Electromagnetics at the Information Engineering Department (DII) of the University of Parma. In particular, with the use of a full vectorial modal solver based on finite element method. Such tools have been constantly updated and enriched with new features also during my PhD project. Regarding the fiber design both design solutions, with flexible fibers and with straight rod-type fibers, have been taken in consideration.

In the case of flexible fibers, a polarization maintaining design has been investigated. The fiber has been designed to be included in a 2 μm fiber laser system working in pulsed operation delivering a train of pulses with more than 1 mJ of energy. The fiber core has been set to reach a diameter of 80 μm. Polarizing effects has been induced with the use of two inserts of boron doped glass. As the thermal expansion of boron doped glass is different with respect to pure silica, during the fiber drawing process, a field of anisotropic stress is created in the structure. The direct consequence of this stress is to induce an anisotropic refractive index change which splits the polarizations of light along the perpendicular axis. During the numerical analysis, elasto-optic effect has been considered with a multi-physics simulation. The holey cladding has been designed with a particular symmetry to ensure a good bending resistance and enough hole to hole space to delocalize higher order modes while preserving fundamental mode well confined in the doped core area. Inner cladding area has been reduced, with a trade of between effects like anti-crossing, to improve pump absorption permitting a shorter amplifier to protect pulse broadening from non linear effects. The fiber has been compared with a scaled version commercial polarizing fiber design, usually used to work around 1 μm region with ytterbium doping, to show the effective improvement of the proposed design. Simulations have shown that the new fiber achieves single mode and single polarization operation in the optimum bending region of radius between 33 and 40 cm, with a remarkable large mode area of 2600 μm^2. The preserved polarization of the fundamental mode is propagating with loss less than 1 dB/m and a large overlap on the doped region, roughly 0.87. The depleted fundamental mode polarization and the higher order modes have loss larger

than 100 dB/m with poor overlap on doped region. This results promise an efficient high power operation and in particular, can assure a safe pulses propagation without damage due to non linear effects. It is worth noting that this design have been implemented on a triangular grid to be fabricated with the stack and draw technique, to reduce future fabrication costs.

Although flexible fibers are a good choice for high power fiber lasers, bending radius and the related bending losses, can become impossible to manage in the case of very large mode area design. A better solution is of rod-type fiber design, where the fiber is forced to be maintained straight through the use of a thick solid silica outer cladding. To improve the already existed good and efficient fiber designs, in this work has been adopted the strategy to break mirror symmetry of the cladding holes lattice. This strategy affects more the confinement of the modes which have mirror symmetry, in particular first higher order mode, and less the modes with circular symmetry like fundamental mode. The overall effect, intrinsic in this idea, is to improve the delocalization of the most detrimental modes preserving single mode operation. To verify this idea, two PCF designs as been proposed. The analysis has been done supposing one meter long amplifier with a standard pump absorption of 9 dB/m, and an input pump power varying from 0 to 300 W, including in the simulations the index modification induced by thermal load. Therefore, the design has been tailored to counteract the thermal effects. The first fiber has been modeled with geometrical parameters, i.e. core diameter of 80 µm and air cladding diameter of 260 µm, similar to a thulium doped large pitch fiber that is regarded as the state of art of large mode area design, in order to perform a fair comparison. Numerical results clearly show that the symmetry free PCF design offers better performance in terms of higher order modes suppression and modal area, over the all region of thulium emission, with respect to the large pitch fiber counterpart. The second symmetry-free fiber design proposed has been tailored to enlarge as much as possible the mode area. With a proper spiral holes lattice, and configuring parameters like holes diameter and level of core down doping, it has been numerically demonstrated the possibility to reach, under severe heating condition, a core diameter as large as 120 µm. This is, as far as I know, the largest core thulium doped fiber design ever proposed, which maintains

robust single mode operation. Effective mode area has been pushed till remarkable values larger than 5000 μm^2.

In summary, this PhD work shows the possibility to counteract thulium doped amplifiers problems in order to work efficiently in the region of 2 µm for high power operation, tailoring specialized PCF design. In particular, a new approach of asymmetric design has been introduced and improved. The capability of these designs to maintain single mode operation has been numerically demonstrated. Nevertheless, all the designs proposed have been configured to follow the scheme imposed by the stack and draw technique to take in consideration the fabrication expenses. Future works can go in the direction of searching for new asymmetric designs in order to improve the state of art of large mode area fibers, not limiting the research on the region of 2 µm emission. Another possibility can be offered by the properties of disordered materials, properly engineered in fiber design, suggesting a new topic of research that can be further investigated. The research area of disordered material is quite promising, both in fiber and laser technologies. Recently, the area of random fiber lasers, which represents a challenge for experimental and analytical description, is attracting increased attention in scientific community [142, 143, 144, 145].

List of pubblications

A list of the publications on international journals, international and national conference proceedings, related to the work presented in this thesis is reported below:

International Journal Papers

- C. Molardi, B. Sun, X. Yu, A. Cucinotta, and S. Selleri, *"Polarization-Maintaining Large Mode Area Fiber Design for 2 μm Operation"*, Photonics Technology Letters, Nov. 2015 (submitted).

- C. Molardi, X. Yu, H. Liang, Y. Zhang, C. Qiu, A. Cucinotta, and S. Selleri, *"Analysis of mid-infrared lasing in active random media"*, Opt. Express 23, 12286-12292 (2015).

- C. Molardi, X. Yu, H. Liang, Y. Zhang, A. Cucinotta, and S. Selleri, *"Modal analysis in 2D media with variable disorder"*, Opt. Express 23, 3681-3689 (2015).

- E. Coscelli, C. Molardi, M. Masruri, A. Cucinotta, and S. Selleri, *"Thermally resilient Tm-doped large mode area photonic crystal fiber with symmetry-free cladding"*, Opt. Express 22, 9707-9714 (2014).

- E.Coscelli, C. Molardi, A. Cucinotta, and S. Selleri, *"Symmetry-free Tm-doped photonic crystal fiber with enhanced mode area"*, IEEE Journal of Selected Topics in Quantum Electronics, vol. 20, no.5, 544-550, Sept.-Oct. 2014.

International Conference Papers

- C. Molardi, H. Liang, X. Yu, A. Cucinotta, S. Selleri, and Y. Zhang, *"Modes analysis in random structures varying the disorder magnitude"*, SPIE Photonics West 2015, paper 9357-42, San Francisco USA, February 2015.
- A. Candiani, E. Coscelli, F. Poli, C. Molardi, A. Cucinotta, and S. Selleri, *"Symmetry-free large-mode area rod-type photonic crystal fibers"*, General Assembly and Scientific Symposium (URSI GASS), 2014 XXXIth URSI Beijing China, August 2014.
- E. Coscelli, C. Molardi, F. Poli, A. Cucinotta, and S. Selleri, *"Tm-doped Rod-type Photonic Crystal Fibers with Symmetry-Free Cladding"*, CLEO:2014, JTh2A.22, San Jose USA, June 2014.
- E. Coscelli, C. Molardi, F. Poli, A. Cucinotta, and S. Selleri, *"Double-cladding photonic crystal fibers with reduced cladding symmetry for Tm-doped lasers"*, SPIE Photonics Europe, paper 9128-8, Brussels Belgium, April 2014.
- C. Molardi, E. Coscelli, A. Cucinotta, and S. Selleri, *"Thermo-optical effects in Tm-doped large mode area photonic crystal fibers"*, SPIE Photonic West 2014, paper 8961-97, San Francisco USA, February 2014.
- Masruri, C. Molardi, L. Vincetti, A. Cucinotta, and S. Selleri, *"Confinement Loss Scaling Law Analysis in Tube Lattice Fibers for Terahertz Applications"*, SPIE Photonic West 2014, paper8985-14, San Francisco USA, February 2014.

National Conference Papers

- E. Coscelli, C. Molardi, F. Poli, A. Cucinotta, and S. Selleri, *"Photonic crystal fibers with reduced cladding symmetry for high power lasers"*, XX RiNEm, Padova Italy, September 2014.
- E. Coscelli, C. Molardi, F. Poli, A. Cucinotta, and S. Selleri, *"Symmetry-free designs of rod-type PCFs for high-power applications"*, Fotonica 2014, Naples Italy, May 2014.

- Masruri, C. Molardi, A.M. Cucinotta, S. Selleri, *"Design and Analysis of Large Pitch Fibers for Single Mode Operation"*, Fotonica 2013, Milan Italy ,May 2013.
- C. Molardi, Masruri, E. Coscelli, F. Poli, A. Cucinotta and S. Selleri, *"FEM solver optimization for PCF design"*, XIX RiNEm, Rome Italy, September 2012.

Bibliography

[1] J. D. Colladon. On the reflections of a ray of light inside a parabolic liquid stream. *Comptes Rendus*, 15:800, 1942.

[2] J. Babinet. Note on the transmission of light by sinuous canals. *Comptes Rendus*, 15:802, 1942.

[3] J. Tyndall. Notes of a Course of Nine Lectures on Light Delivered at the Royal Institution of Great Britain. 1970.

[4] H. H. Hopkins and N. S. Kapany. A Flexible Fibrescope, using Static Scanning. *Nature*, 173(4392):39–41, January 1954.

[5] A. L. Schawlow and C. H. Townes. Infrared and optical masers. *Phys. Rev.*, 112:1940–1949, Dec 1958.

[6] K. C. Kao and G. A. Hockham. Dielectric-fibre surface waveguides for optical frequencies. *Proc. Inst. Elect. Eng.*, 113(7):1151–1158, July 1966.

[7] C. J. Koester and E. Snitzer. Amplification in a fiber laser. *Appl. Opt.*, 3(10):1182–1186, Oct 1964.

[8] S. B. Poole, D. N. Payne, and M. E. Fermann. Fabrication of low-loss optical fibres containing rare-earth ions. *Electronics Letters*, 21(17):737–738, August 1985.

[9] J. C. Knight, T. A. Birks, P. St. J. Russell, and D. M. Atkin. All-silica single-mode optical fiber with photonic crystal cladding. *Opt. Lett.*, 21(19):1547–1549, Oct 1996.

[10] R. F. Cregan, B. J. Mangan, J. C. Knight, T. A. Birks, P. St. J. Russell, P. J. Roberts, and D. C. Allan. Single-mode photonic band gap guidance of light in air. *Science*, 285(5433):1537–1539, 1999.

[11] W. A. Gambling. The rise and rise of optical fibers. *Selected Topics in Quantum Electronics, IEEE Journal of*, 6(6):1084–1093, Nov 2000.

[12] O. Ziemann, J. Krauser, P. E. Zamzow, and W. Daum. *POF Handbook - Optical Short Range Transmission Systems*. Springer Berlin Heidelberg, third edition, 2008.

[13] D. Tran, G. Sigel, and B. Bendow. Heavy metal fluoride glasses and fibers: A review. *Lightwave Technology, Journal of*, 2(5):566–586, Oct 1984.

[14] A. Ghatak and K. Thyagarajan. *An Introduction to Fiber Optics*. Cambridge University Press, first edition, June 1998.

[15] P. Bassi, G. Bellanca, and G. Tartarini. *Propagazione ottica libera e guidata*. CLUEB, January 2000.

[16] Corning [online]. URL: `http://www.corning.com/worldwide/en/products/communication-networks/products/fiber.html` [cited 1-12-2015].

[17] J. C. Knight, J. Arriaga, T. A. Birks, A. Ortigosa-Blanch, W. J. Wadsworth, and P. S. J. Russell. Anomalous dispersion in photonic crystal fiber. *Photonics Technology Letters, IEEE*, 12(7):807–809, July 2000.

[18] F. Poli, A. Cucinotta, S. Selleri, and A. H. Bouk. Tailoring of flattened dispersion in highly nonlinear photonic crystal fibers. *Photonics Technology Letters, IEEE*, 16(4):1065–1067, April 2004.

[19] L. F. Mollenauer, R. H. Stolen, and J. P. Gordon. Experimental observation of picosecond pulse narrowing and solitons in optical fibers. *Phys. Rev. Lett.*, 45:1095–1098, Sep 1980.

[20] M. N. Islam. Raman amplifiers for telecommunications. *Selected Topics in Quantum Electronics, IEEE Journal of*, 8(3):548–559, May 2002.

[21] L. F. Mollenauer and R. H. Stolen. The soliton laser. *Opt. Lett.*, 9(1):13–15, Jan 1984.

[22] J. M. Dudley, G. Genty, and S. Coen. Supercontinuum generation in photonic crystal fiber. *Rev. Mod. Phys.*, 78:1135–1184, Oct 2006.

[23] G. P. Agrawal. *Nonlinear Fiber Optics*. Academic Press. Academic Press, 2013.

[24] G. P. Agrawal. *Applications of Nonlinear Fiber Optics*. Academic Press. Academic Press, 2008.

[25] G. P. Agrawal. Nonlinear fiber optics: its history and recent progress. *J. Opt. Soc. Am. B*, 28(12):A1–A10, Dec 2011.

[26] T. A. Birks, J. C. Knight, and P. St. J. Russell. Endlessly single-mode photonic crystal fiber. *Opt. Lett.*, 22(13):961–963, Jul 1997.

[27] P. Russell. Photonic crystal fibers. *Science*, 299(5605):358–362, 2003.

[28] T. T. Alkeskjold, M. Laurila, J. Weirich, M. M. Johansen, C. B. Olausson, O. Lumholt, D. Noordegraaf, M. D. Maack, and C. Jakobsen. Photonic crystal fiber amplifiers for high power ultrafast fiber lasers. *Nanophotonics*, 2(5-6):369âĂŞ–381, Nov 2013.

[29] C. Jauregui, J. Limpert, and A. Tunnermann. High-power fibre lasers. *Nat. Photon.*, 7(11):861–867, Nov 2013.

[30] F. Yu, W. J. Wadsworth, and J. C. Knight. Low loss silica hollow core fibers for 3–4 μm spectral region. *Opt. Express*, 20(10):11153–11158, May 2012.

[31] Z. Wang, W. Belardi, F. Yu, W. J. Wadsworth, and J. C. Knight. Efficient diode-pumped mid-infrared emission from acetylene-filled hollow-core fiber. *Opt. Express*, 22(18):21872–21878, Sep 2014.

[32] S. T. Bauerschmidt, D. Novoa, A. Abdolvand, and P. St.J. Russell. Broadband-tunable lp01 mode frequency shifting by raman coherence waves in a h2-filled hollow-core photonic crystal fiber. *Optica*, 2(6):536–539, Jun 2015.

[33] N. A. Mortensen, J. R. Folkenberg, M. D. Nielsen, and K. P. Hansen. Modal cutoff and the v parameter in photonic crystal fibers. *Opt. Lett.*, 28(20):1879–1881, Oct 2003.

[34] M. Nielsen and N. Mortensen. Photonic crystal fiber design based on the v-parameter. *Opt. Express*, 11(21):2762–2768, Oct 2003.

[35] P. St.J. Russell. Photonic-crystal fibers. *Lightwave Technology, Journal of*, 24(12):4729–4749, Dec 2006.

[36] P. Roberts, F. Couny, H. Sabert, B. Mangan, T. Birks, J. Knight, and P. Russell. Loss in solid-core photonic crystal fibers due to interface roughness scattering. *Opt. Express*, 13(20):7779–7793, Oct 2005.

[37] P. J. Roberts, F., H. Sabert, B. J. Mangan, D. P. Williams, L. Farr, M. W. Mason, A. Tomlinson, T. A. Birks, J. C. Knight, and P. St.J. Russell. Ultimate low loss of hollow-core photonic crystal fibres. *Opt. Express*, 13(1):236–244, Jan 2005.

[38] E. Snitzer. Proposed fiber cavities for optical masers. *Journal of Applied Physics*, 32(1):36–39, 1961.

[39] E. Snitzer. Optical maser action of nd^{+3} in a barium crown glass. *Phys. Rev. Lett.*, 7:444–446, Dec 1961.

[40] R. J. Mears, L. Reekie, S. B. Poole, and D. N. Payne. Neodymium-doped silica single-mode fibre lasers. *Electronics Letters*, 21(17):738–740, August 1985.

[41] H. Zellmer, A. Tunnermann, H. Welling, and V. Reichel. Double-clad fiber laser with 30 w output power. In *Optical Amplifiers and Their Applications*, pages 137–140. Optical Society of America, 1997.

[42] D. C. Hanna, R. M. Percival, I. R. Perry, R. G. Smart, P. J. Suni, and A. C. Tropper. An ytterbium-doped monomode fibre laser: Broadly tunable operation from 1.010 μm to 1.162 μm and three-level operation at 964 nm. *Journal of Modern Optics*, 37(4):517–525, 1990.

[43] S. D. Jackson. Towards high-power mid-infrared emission from a fibre laser. *Nat. Photon.*, 6(7):423–431, Jul 2012.

[44] K. Thyagarajan and A. Ghatak. *Lasers: Fundamentals and Applications*. Graduate Texts in Physics. Springer US, 2010.

[45] O. Svelto. *Principles of Lasers*. Springer US, 2010.

[46] H. M. Pask, R. J. Carman, D. C. Hanna, A. C. Tropper, C. J. Mackechnie, P. R. Barber, and J. M. Dawes. Ytterbium-doped silica fiber lasers: versatile sources for the 1-1.2 μm region. *Selected Topics in Quantum Electronics, IEEE Journal of*, 1(1):2–13, Apr 1995.

[47] E. Snitzer, H. Po, F. Hakimi, R. Tumminelli, and B.C. McCollum. Double clad, offset core nd fiber laser. In *Optical Fiber Sensors*, page PD5. Optical Society of America, 1988.

[48] R. J. Mears, L. Reekie, S. B. Poole, and D. N. Payne. Low-threshold tunable cw and q-switched fibre laser operating at 1.55 μm. *Electronics Letters*, 22(3):159–160, January 1986.

[49] U. Sharma, K. Chang-Seok, and J. U. Kang. Highly stable tunable dual-wavelength q-switched fiber laser for dial applications. *Photonics Technology Letters, IEEE*, 16(5):1277–1279, May 2004.

[50] B. Chen, X. Zhang, K. Wu, H. Wang, J. Wang, and J. Chen. Q-switched fiber laser based on transition metal dichalcogenides mos_2, $mose_2$, ws_2, and wse_2. *Opt. Express*, 23(20):26723–26737, Oct 2015.

[51] F. Stutzki, F. Jansen, A. Liem, C. Jauregui, J. Limpert, and A. Tunnermann. 26 mj, 130 w q-switched fiber-laser system with near-diffraction-limited beam quality. *Opt. Lett.*, 37(6):1073–1075, Mar 2012.

[52] T. Pfeiffer and G. Veith. 40 ghz pulse generation using a widely tunable all-polarisation preserving erbium fibre ring laser. *Electronics Letters*, 29(21):1849–1850, Oct 1993.

[53] A. Martinez and S. Yamashita. Multi-gigahertz repetition rate passively modelocked fiber lasers using carbon nanotubes. *Opt. Express*, 19(7):6155–6163, Mar 2011.

[54] F. Stutzki, F. Jansen, H. J. Otto, C. Jauregui, J. Limpert, and A. Tunnermann. Designing advanced very-large-mode-area fibers for power scaling of fiber-laser systems. *Optica*, 1(4):233–242, Oct 2014.

[55] J. C. Knight, T. A. Birks, R. F. Cregan, P. S. J. Russell, and J. P. de Sandro. Large mode area photonic crystal fibre. *Electronics Letters*, 34(13):1347–1348, Jun 1998.

[56] K. Tankala, D. Guertin, J. Abramczyk, and N. Jacobson. Reliability of low-index polymer coated double-clad fibers used in fiber lasers and amplifiers. *Optical Engineering*, 50(11):111607–111615, 2011.

[57] Nufern [online]. URL: `http://www.nufern.com/pam/optical_fibers/` [cited 4-12-2015].

[58] J. P. Koplow, D. A. V. Kliner, and L. Goldberg. Single-mode operation of a coiled multimode fiber amplifier. *Opt. Lett.*, 25(7):442–444, Apr 2000.

[59] R. T. Schermer. Mode scalability in bent optical fibers. *Opt. Express*, 15(24):15674–15701, Nov 2007.

[60] J. Limpert, N. Deguil-Robin, I. Manek-Honninger, F. Salin, F. Roser, A. Liem, T. Schreiber, S. Nolte, H. Zellmer, A. Tunnermann, J. Broeng, A. Petersson, and C. Jakobsen. High-power rod-type photonic crystal fiber laser. *Opt. Express*, 13(4):1055–1058, Feb 2005.

[61] F. Jansen, F. Stutzki, C. Jauregui, J. Limpert, and A. Tunnermann. Avoided crossings in photonic crystal fibers. *Opt. Express*, 19(14):13578–13589, Jul 2011.

[62] T. Eidam, J. Rothhardt, F. Stutzki, F. Jansen, S. Hadrich, H. Carstens, C. Jauregui, J. Limpert, and A. Tunnermann. Fiber chirped-pulse amplification system emitting 3.8 gw peak power. *Opt. Express*, 19(1):255–260, Jan 2011.

[63] T. T. Alkeskjold, M. Laurila, L. Scolari, and J. Broeng. Single-mode ytterbium-doped large-mode-area photonic bandgap rod fiber amplifier. *Opt. Express*, 19(8):7398–7409, Apr 2011.

[64] M. M. Jorgensen, S. R. Petersen, M. Laurila, J. Lagsgaard, and T. T. Alkeskjold. Optimizing single mode robustness of the distributed modal filtering rod fiber amplifier. *Opt. Express*, 20(7):7263–7273, Mar 2012.

[65] L. Dong, T. W. Wu, H. A. Mckay, L. Fu, J. Li, and H. G. Winful. All-glass large-core leakage channel fibers. *Selected Topics in Quantum Electronics, IEEE Journal of*, 15(1):47–53, Jan 2009.

[66] L. Dong, H. A. McKay, L. Fu, M. Ohta, A. Marcinkevicius, S. Suzuki, and M. E. Fermann. Ytterbium-doped all glass leakage channel fibers with highly fluorine-doped silica pump cladding. *Opt. Express*, 17(11):8962–8969, May 2009.

[67] D. Jain, C. Baskiotis, and J. K. Sahu. Mode area scaling with multi-trench rod-type fibers. *Opt. Express*, 21(2):1448–1455, Jan 2013.

[68] D. Jain, Y. Jung, J. Kim, and J. K. Sahu. Robust single-mode all-solid multi-trench fiber with large effective mode area. *Opt. Lett.*, 39(17):5200–5203, Sep 2014.

[69] D. Jain, C. Baskiotis, T.C. May-Smith, J. Kim, and J. K. Sahu. Large mode area multi-trench fiber with delocalization of higher order modes. *Selected Topics in Quantum Electronics, IEEE Journal of*, 20(5):242–250, Sept 2014.

[70] X. Ma, C. Zhu, I. N. Hu, A. Kaplan, and A. Galvanauskas. Single-mode chirally-coupled-core fibers with larger than 50μm diameter cores. *Opt. Express*, 22(8):9206–9219, Apr 2014.

[71] G. M. Hale and M. R. Querry. Optical constants of water in the 200-nm to 200 μm wavelength region. *Appl. Opt.*, 12(3):555–563, Mar 1973.

[72] N. M. Fried and K. E. Murray. High-power thulium fiber laser ablation of urinary tissues at 1.94 μm. *Journal of Endourology*, 19(1):25–31, Jan 2005.

[73] N. M. Fried. Thulium fiber laser lithotripsy: An in vitro analysis of stone fragmentation using a modulated 110-watt thulium fiber laser at 1.94 Âţm. *Lasers in Surgery and Medicine*, 37(1):53–58, 2005.

[74] S. J. Xia, J. Zhuo, X. W. Sun, B. M. Han, Y. Shao, and Y. N. Zhang. Thulium laser versus standard transurethral resection of the prostate: A randomized prospective trial. *European Urology*, 53(2):382 – 390, 2008.

[75] B. Chen, S. L. Thomsen, R. J. Thomas, J. Oliver, and A. J. Welch. Histological and modeling study of skin thermal injury to 2.0 μm laser irradiation. *Lasers in Surgery and Medicine*, 40(5):358–370, 2008.

[76] S. M. Zeitels, J. A. Burns, L. M. Akst, R. E. Hillman, M. S. Broadhurst, and R. R. Anderson. Office-based and microlaryngeal applications of a fiber-based thulium laser. *Ann. Otol. Rhinol. Laryngol.*, 115(12):891–896, 2006.

[77] M. H. Bui, A. Breda, D. Gui, J. Said, and P. Schulam. Less smoke and minimal tissue carbonization using a thulium laser for laparoscopic partial nephrectomy without hilar clamping in a porcine model. *Journal of Endourology*, 21(9):1107–1112, 2007.

[78] J. W. Hazey, V. K. Narula, D. B. Renton, K. M. Reavis, C. M. Paul, K. E. Hinshaw, P. Muscarella, E. C. Ellison, and W. S. Melvin. Natural-orifice transgastric endoscopic peritoneoscopy in humans: Initial clinical trial. *Surgical Endoscopy*, 22(1):16–20, 2008.

[79] J. P. Cariou, B. Augere, and M. Valla. Laser source requirements for coherent lidars based on fiber technology. *Comptes Rendus Physique*, 7(2):213–223, 2006.

[80] P. Sprangle, A. Ting, J. Penano, R. Fischer, and B. Hafizi. Incoherent combining and atmospheric propagation of high-power fiber lasers for directed-energy applications. *Quantum Electronics, IEEE Journal of*, 45(2):138–148, Feb 2009.

[81] C. R. Phillips, J. Jiang, C. Langrock, M. M. Fejer, and M. E. Fermann. Self-referenced frequency comb from a tm-fiber amplifier via ppln waveguide supercontinuum generation. In *Lasers and Electro-Optics (CLEO), 2011 Conference on*, pages 1–2, May 2011.

[82] O. P. Kulkarni, V. V. Alexander, M. Kumar, M. J. Freeman, M. N. Islam, F. L. Terry, M. Neelakandan, and A. Chan. Supercontinuum generation from 1.9 to 4.5âĂL'μmin zblan fiber with high average power generation beyond 3.8âĂL'μm using a thulium-doped fiber amplifier. *J. Opt. Soc. Am. B*, 28(10):2486–2498, Oct 2011.

[83] Z. Li, A. M. Heidt, J. M. O. Daniel, Y. Jung, S. U. Alam, and D. J. Richardson. Thulium-doped fiber amplifier for optical communications at 2 μm. *Opt. Express*, 21(8):9289–9297, Apr 2013.

[84] S. D. Jackson and T. A. King. Theoretical modeling of tm-doped silica fiber lasers. *Lightwave Technology, Journal of*, 17(5):948–956, May 1999.

[85] P. Peterka, B. Faure, W. Blanc, M. KarÃąsek, and B. Dussardier. Theoretical modelling of s-band thulium-doped silica fibre amplifiers. *Optical and Quantum Electronics*, 36(1-3):201–212, 2004.

[86] D. C. Brown and H. J. Hoffman. Thermal, stress, and thermo-optic effects in high average power double-clad silica fiber lasers. *Quantum Electronics, IEEE Journal of*, 37(2):207–217, Feb 2001.

[87] B. Zintzen, T. Langer, J. Geiger, D. Hoffmann, and P. Loosen. Heat transport in solid and air-clad fibers for high-power fiber lasers. *Opt. Express*, 15(25):16787–16793, Dec 2007.

[88] M. Sabaeian. The effects of air-holes on temperature and temperature gradient of solid-core photonic crystal fiber lasers. *Optik - International Journal for Light and Electron Optics*, 124(22):5787 – 5791, 2013.

[89] C. Gaida, P. Kadwani, L. Leick, J. Broeng, L. Shah, and M. Richardson. Cw-lasing and amplification in tm3+-doped photonic crystal fiber rod. *Opt. Lett.*, 37(21):4513–4515, Nov 2012.

[90] N. Modsching, P. Kadwani, R. A. Sims, L. Leick, J. Broeng, L. Shah, and M. Richardson. Lasing in thulium-doped polarizing photonic crystal fiber. *Opt. Lett.*, 36(19):3873–3875, Oct 2011.

[91] F. Jansen, F. Stutzki, C. Jauregui, J. Limpert, and A. Tunnermann. High-power very large mode-area thulium-doped fiber laser. *Opt. Lett.*, 37(21):4546–4548, Nov 2012.

[92] M. M. Johansen, K. R. Hansen, M. Laurila, T. T. Alkeskjold, and J. Lagsgaard. Estimating modal instability threshold for photonic crystal rod fiber amplifiers. *Opt. Express*, 21(13):15409–15417, Jul 2013.

[93] Z. Zhu and T. G. Brown. Stress-induced birefringence in microstructured optical fibers. *Opt. Lett.*, 28(23):2306–2308, Dec 2003.

[94] T. Schreiber, H. Schultz, O. Schmidt, F. Roser, J. Limpert, and A. Tunnermann. Stress-induced birefringence in large-mode-area micro-structured optical fibers. *Opt. Express*, 13(10):3637–3646, May 2005.

[95] S. Selleri and J. Petracek. Modal analysis of rib waveguide through finite element and mode matching methods. *Optical and Quantum Electronics*, 33(4-5):373–386, 2001.

[96] F. Poli, A. Cucinotta, and S. Selleri. *Photonic Crystal Fibers - Properties and Applications*. Springer Series in Materials Science. Springer Netherlands, 2007.

[97] M. Steel. Reflection symmetry and mode transversality in microstructured fibers. *Opt. Express*, 12(8):1497–1509, Apr 2004.

[98] F. Stutzki, F. Jansen, C. Jauregui, J. Limpert, and A. Tunnermann. Non-hexagonal large-pitch fibers for enhanced mode discrimination. *Opt. Express*, 19(13):12081–12086, Jun 2011.

[99] E. Coscelli, F. Poli, T. T. Alkeskjold, M. M. Jorgensen, L. Leick, J. Broeng, A. Cucinotta, and S. Selleri. Thermal effects on the single-mode regime of distributed modal filtering rod fiber. *Lightwave Technology, Journal of*, 30(22):3494–3499, Nov 2012.

[100] P. F. Moulton, G. A. Rines, E. V. Slobodtchikov, K. F. Wall, G. Frith, B. Samson, and A. L. G. Carter. Tm-doped fiber lasers: Fundamentals and power scaling. *Selected Topics in Quantum Electronics, IEEE Journal of*, 15(1):85–92, Jan 2009.

[101] Aa. Tunnermann, T. Schreiber, and J. Limpert. Fiber lasers and amplifiers: an ultrafast performance evolution. *Appl. Opt.*, 49(25):F71–F78, Sep 2010.

[102] S. D. Jackson. Cross relaxation and energy transfer upconversion processes relevant to the functioning of 2 μm tm^{3+}-doped silica fibre lasers. *Optics Communications*, 230(13):197 – 203, 2004.

[103] R. Dauliat, D. Gaponov, A. Benoit, F. Salin, K. Schuster, R. Jamier, and P. Roy. Inner cladding microstructuration based on symmetry reduction for improvement of singlemode robustness in vlma fiber. *Opt. Express*, 21(16):18927–18936, Aug 2013.

[104] E. Coscelli, F. Poli, T. T. Alkeskjold, D. Passaro, A. Cucinotta, L. Leick, J. Broeng, and S. Selleri. Single-mode analysis of yb-doped double-cladding distributed spectral filtering photonic crystal fibers. *Opt. Express*, 18(26):27197–27204, Dec 2010.

[105] E. Coscelli, F. Poli, M. M. Jorgensen, T. T. Alkeskjold, L. Leick, J. Broeng, M. Sozzi, A. Candiani, A. Cucinotta, and S. Selleri. Thermal effect-resilient design of large mode area double-cladding yb-doped photonic crystal fibers. In *Proc. SPIE*, volume 8601, pages 86012O–86012O–7, 2013.

[106] R. Guobin, W. Zhi, L. Shuqin, and J. Shuisheng. Mode classification and degeneracy in photonic crystal fibers. *Opt. Express*, 11(11):1310–1321, Jun 2003.

[107] J. Limpert, F. Stutzki, H. J. Otto F. Jansen, Tino T. Eidam, and C. Jauregui A. Tunnermann. Yb-doped large-pitch fibres: effective single-mode operation based on higher-order mode delocalisation. *Light Sci Appl*, 1:e8, Apr 2012.

[108] S. Selleri and M. Zoboli. Performance comparison of finite-element approaches for electromagnetic waveguides. *J. Opt. Soc. Am. A*, 14(7):1460–1466, Jul 1997.

[109] F. Poli, E. Coscelli, T. T. Alkeskjold, D. Passaro, A. Cucinotta, L. Leick, J. Broeng, and S. Selleri. Cut-off analysis of 19-cell yb-doped double-cladding rod-type photonic crystal fibers. *Opt. Express*, 19(10):9896–9907, May 2011.

[110] Y. Fan, B. He, J. Zhou, J. Zheng, H. Liu, Y. Wei, J. Dong, and Q. Lou. Thermal effects in kilowatt all-fiber mopa. *Opt. Express*, 19(16):15162–15172, Aug 2011.

[111] E. Coscelli, F. Poli, T. T. Alkeskjold, F. Salin, L. Leick, J. Broeng, A. Cucinotta, and S. Selleri. Single-mode design guidelines for 19-cell double-cladding photonic crystal fibers. *Lightwave Technology, Journal of*, 30(12):1909–1914, June 2012.

[112] S. Liao, M. Gong, and H. Zhang. Theoretical calculation of beam quality factor of large-mode-area fiber amplifiers. *Laser Physics*, 19(3):437–444, 2009.

[113] H. K. Liang, B. Meng, G. Liang, J. Tao, Y. Chong, Q. J. Wang, and Y. Zhang. Electrically pumped mid-infrared random lasers. *Advanced Materials*, 25(47):6859–6863, 2013.

[114] D. S. Wiersma. The physics and applications of random lasers. *Nat Phys*, 4(5):359–367, May 2008.

[115] B. Redding, S. F. Liew, R. Sarma, and H. Cao. Compact spectrometer based on a disordered photonic chip. *Nat Photon*, 7(9):746–751, Sep 2013.

[116] F. Pratesi, M. Burresi, F. Riboli, K. Vynck, and D. S. Wiersma. Disordered photonic structures for light harvesting in solar cells. *Opt. Express*, 21(S3):A460–A468, May 2013.

[117] B. Redding, M. A. Choma, and H. Cao. Speckle-free laser imaging using random laser illumination. *Nat Photon*, 6(6):355–359, Jun 2012.

[118] D. S. Wiersma, P. Bartolini, A. Lagendijk, and R. Righini. Localization of light in a disordered medium. *Nature*, 390(6661):671–673, Dec 1997.

[119] K. Vyncki, M. Burresi, F. Riboli, and D. S. Wiersma. Photon management in two-dimensional disordered media. *Nat Mater*, 11(12):1017–1022, Dec 2012.

[120] M. Segev, Y. Silberberg, and D. N. Christodoulides. Anderson localization of light. *Nat Photon*, 7(3):197–204, Mar 2012.

[121] A. L. Burin, M. A. Ratner, H. Cao, and S. H. Chang. Random laser in one dimension. *Phys. Rev. Lett.*, 88:093904, Feb 2002.

[122] V. S. Letokhov. Light generation by a scattering medium with a negative resonant absorption. *Sov. Phys. JETP*, 16:835–840, 1968.

[123] N. M. Lawandy, R. M. Balachandran, A. S. L. Gomes, and E. Sauvain. Laser action in strongly scattering media. *Nature*, 368(6470):436–438, Mar 1994.

[124] D. S. Wiersma and A. Lagendijk. Light diffusion with gain and random lasers. *Phys. Rev. E*, 54:4256–4265, Oct 1996.

[125] K. L. van der Molen, R. W. Tjerkstra, A. P. Mosk, and A. Lagendijk. Spatial extent of random laser modes. *Phys. Rev. Lett.*, 98:143901, Apr 2007.

[126] P. Sebbah and C. Vanneste. Random laser in the localized regime. *Phys. Rev. B*, 66:144202, Oct 2002.

[127] J. Andreasen, A. A. Asatryan, L. C. Botten, M. A. Byrne, H. Cao, L. Ge, L. Labonté, P. Sebbah, A. D. Stone, H. E. Tureci, and C. Vanneste. Modes of random lasers. *Adv. Opt. Photon.*, 3(1):88–127, Mar 2011.

[128] H. Cao, X. Jiang, Y. Ling, J. Y. Xu, and C. M. Soukoulis. Mode repulsion and mode coupling in random lasers. *Phys. Rev. B*, 67:161101, Apr 2003.

[129] J. Fallert, R. J. B. Dietz, J. Sartor, D. Schneider, C. Klingshirn, and H. Kalt. Co-existence of strongly and weakly localized random laser modes. *Nat Photon*, 3(5):279–282, May 2009.

[130] C. Vanneste and P. Sebbah. Complexity of two-dimensional quasimodes at the transition from weak scattering to anderson localization. *Phys. Rev. A*, 79:041802, Apr 2009.

[131] J. Faist, F. Capasso, D. L. Sivco, C. Sirtori, A. L. Hutchinson, and A. Y. Cho. Quantum cascade laser. *Science*, 264(5158):553–556, 1994.

[132] T. Schwartz, G. Bartal, S. Fishman, and M. Segev. Transport and anderson localization in disordered two-dimensional photonic lattices. *Nature*, 446(7131):52–55, Mar 2007.

[133] F. Riboli, N. Caselli, S. Vignolini, F. Intonti, K. Vynck, P. Barthelemy, A. Gerardino, L. Balet, L. H. Li, A. Fiore, M. Gurioli, and D. S. Wiersma. Engineering of light confinement in strongly scattering disordered media. *Nat Mater*, 13(7):720–725, Jul 2014.

[134] X. Jiang and C. M. Soukoulis. Transmission and reflection studies of periodic and random systems with gain. *Phys. Rev. B*, 59:6159–6166, Mar 1999.

[135] X. Jiang and C. M. Soukoulis. Time dependent theory for random lasers. *Phys. Rev. Lett.*, 85:70–73, Jul 2000.

[136] S. Mujumdar, M. Ricci, R. Torre, and D. S. Wiersma. Amplified extended modes in random lasers. *Phys. Rev. Lett.*, 93:053903, Jul 2004.

[137] S. Mujumdar, R. Torre, H. Ramachandran, and D. S. Wiersma. Monte carlo calculations of spectral features in random lasing. *Journal of Nanophotonics*, 4(1):041550–041550–13, 2010.

[138] L. G. Henyey and J. L. Greenstein. Diffuse radiation in the galaxy. *Astrophysical Journal*, 93:70–83, 1941.

[139] R. Uppu and S. Mujumdar. Dependence of the gaussian-levy transition on the disorder strength in random lasers. *Phys. Rev. A*, 87:013822, Jan 2013.

[140] E. Zielinski, H. Schweizer, K. Streubel, H. Eisele, and G. Weimann. Excitonic transitions and exciton damping processes in ingaas/inp. *Journal of Applied Physics*, 59(6):2196–2204, 1986.

[141] H. C. Liu, F. Capasso, E. R. Weber, and R. K. Willardson. *Intersubband Transitions in Quantum Wells: Physics and Device Applications.* Academic Press, 1999.

[142] S. Karbasi, T. Hawkins, J. Ballato, K. W. Koch, and A. Mafi. Transverse anderson localization in a disordered glass optical fiber. *Opt. Mater. Express*, 2(11):1496–1503, Nov 2012.

[143] S. K. Turitsyn, S. A. Babin, A. E. El-Taher, P. Harper, D. V. Churkin, S. I. Kablukov, J. D. Ania-Castanon, V. Karalekas, and E. V. Podivilov. Random distributed feedback fibre laser. *Nat Photon*, 4(4):231–235, Apr 2010.

[144] D. V. Churkin, I. V. Kolokolov, E. V. Podivilov, I. D. Vatnik, M. A. Nikulin, S. S. Vergeles, I. S. Terekhov, V. V. Lebedev, G. Falkovich, S. A.Babin, and S. K. Turitsyn. Wave kinetics of random fibre lasers. *Nat Commun*, 2, Feb 2015.

[145] Y. Tang and J. Xu. A random q-switched fiber laser. *Nat Commun*, 5, Mar 2015.

Acknowledgement

Now it is mandatory to write some simple words to be grateful to all the people who helped me during these past years.

A heartfelt thanks shall be addressed to my family, in particular my father who supported me nevertheless the difficult time my family experienced in the last years. After that, a great thanks to my wife Asma who has been constantly near me.

Then, I would like to thank my supervisor Prof. Stefano Selleri and Prof. Annamaria Cucinotta who gave me the opportunity to improve my knowledge and supported my work during all this period. A great thanks also to my colleagues and friends at the University of Parma: Federica, Enrico, Alessandro, Michele, Lorenzo and Masruri for the friendship they demonstrated to me and for the constant help I received from them.

A special thanks is addressed to my supervisor in SIMTech Dr. Yu Xia and to the big boss Dr. Zhang Ying, who were able to motivate me during my stay in Singapore. Their useful suggestions is priceless. I would like to thank also the other members (current and former) of optic team: Boon Ping, Li Hao, Hon Leun, Houkun, Chris, Jiayun, Patrice and Liang Jie. A particular thanks to the guys and girls involved in Dr. Yu Xia group: Yanyan, Jiaqi, Elizabeth, Zhiyu, Derrick and Sun Biao, not only for the excellent scientific discussions that we have done together but also for the friendship they offered me, with their help I felt like to be at home. Then, I can not forget other smart friends I met in SIMTech, in particular: Jonathon, Bing Quing, Min Hao and Adrian.

Finally, I would like to remember all my Italian friends who spent time to help

me, to suggest me or simple to be patient to hear my boring stories. In this group, I have to explicitly mention: Alberto, Simone, Riccardo and Stefano.

An official acknowledgment shall be recognized to Singapore and the Agency for Science Technology and Research (A*STAR), which supported my work with the scholarship offered by A*STAR Research Attachment Programme (ARAP).